9-12-2011 12:00 AM

Vortex shedding from elongated bluff bodies

Zachary J. Taylor, *University of Western Ontario*

Supervisor: Dr. Gregory Kopp, *The University of Western Ontario*
Joint Supervisor: Dr. Roi Gurka, *The University of Western Ontario*
A thesis submitted in partial fulfillment of the requirements for the Doctor of Philosophy degree in Civil and Environmental Engineering

VORTEX SHEDDING FROM ELONGATED BLUFF BODIES

(Thesis format: Integrated Article)

by

Zachary John Taylor

Graduate Program in Civil and Environmental Engineering

A thesis submitted in partial fulfillment
of the requirements for the degree of
Doctor of Philosophy

The School of Graduate and Postdoctoral Studies
The University of Western Ontario
London, Ontario, Canada

THE UNIVERSITY OF WESTERN ONTARIO
School of Graduate and Postdoctoral Studies

CERTIFICATE OF EXAMINATION

Supervisors	Examiners
Dr. Gregory Kopp	Dr. Craig Miller
Dr. Roi Gurka	Dr. J. Maciej Floryan
	Dr. Wayne Hocking
	Dr. Pierre Sullivan

The thesis by

Zachary John Taylor

entitled:

Vortex shedding from elongated bluff bodies

is accepted in partial fulfillment of the
requirements for the degree of
Doctor of Philosophy

Date	Chair of the Thesis Examination Board

Abstract

As the spans of suspension bridges increase, the structures become inherently flexible. The flexibility of these structures, combined with the wind and particular aerodynamics, can lead to significant motions. From the collapse due to flutter of the Tacoma Narrows Bridge to the case of vortex-induced vibrations (VIV) of the Storebælt Bridge, it is evident that a better understanding of the aerodynamics of these geometries is necessary. The work herein is motivated by these two problems and is presented in two parts.

In the first part, the focus is on the physical mechanisms of vortex shedding. It is shown that the wake formation for elongated bluff bodies is distinct from shorter bluff bodies due to the leading edge separating-reattaching flow. Pressure data are then used to propose a mechanism of competition between the flow at the leading and trailing edges rather than synchronization which occurs at low Reynolds numbers. Within the context of this framework, the wakes are orthogonally decomposed and it was discovered that new modes appear not previously observed for shorter bluff bodies. In Part II, a time-resolved Particle Image Velocimetry (PIV) system is developed. This system is used to capture both the high and low frequency dynamics of flutter due its uniquely long recording length. It is shown that, contrary to conventional understanding, the vortex shedding does not significantly change during flutter. Thus, the fact that these bodies shed vortices is only a secondary effect in relation to the flutter instability.

There is a distinct contrast between flutter and VIV: the latter is known to be governed by the vortex shedding wake and it has been shown herein that the former is not. Regarding the problem of VIV, it is shown that the wakes of these bodies are formed due to interaction with the leading edge separating-reattaching flow. As the leading edge separation angle grows, it is shown to disturb the trailing edge vortex shedding altering many of the key parameters including fluctuating lift force and shedding frequency.

Keywords

Vortex shedding, elongated bluff bodies, bluff body aerodynamics, long-span suspension bridges, particle image velocimetry, flutter

Co-Authorship Statement

The articles used in this integrated article thesis are each co-authored. The contributions of each author are discussed in this section. There are three articles (Chapter 3, Chapter 4 and Chapter 7) which are authored by my two co-supervisors and myself with me being the first author on all of them. For these articles, I performed the experiments, the analysis and the preparation of the manuscripts. However, the advice and comments of my co-supervisors were invaluable in the preparation of these articles.

The article entitled "Long-duration time-resolved PIV to study unsteady aerodynamics" (Chapter 2) was co-authored with my two co-supervisors and Dr. Alex Liberzon of the Tel Aviv University. In this paper, I performed and analyzed the results of the experiments as well as being primarily responsible for the integration of the time-resolved PIV system. I was also primarily responsible for the preparation of the manuscript. In this article, we also presented our work on an open source Particle Image Velocimetry (PIV) analysis package. This software package was originally written by one of my co-supervisors (Dr. Roi Gurka) and his colleague Dr. Alex Liberzon. Thus, the extension of this package which I performed could not have been successful without their input.

The article entitled "Features of the turbulent flow around symmetric elongated bluff bodies" (Chapter 2) is co-authored by my two co-supervisors and Ms. Emanuela Palombi. Ms. Palombi is a former M.E.Sc. student of my co-supervisors. She and I performed the initial PIV experiments on the symmetric bluff bodies featured in this article. Ms. Palombi performed the pressure measurements that were used for these bodies. It is noted, however, that I repeated and extended the PIV measurements that were originally made to improve the quality and resolution of the data. Thus, for the article contained in , I performed the majority of the measurements, all of the analysis and I prepared the manuscript in its entirety.

Dedication

This work is dedicated to the two most important women in my life: my mother, Beverly, who passed away during the completion of this work, and to my wife and best friend, Lisa.

Acknowledgements

First of all, I want to thank my co-supervisors Drs. Greg Kopp and Roi Gurka. I first worked with Greg as an undergraduate student in the summer of 2005. After that summer I knew that I had found an exceptional supervisor and decided to do my Ph.D. under his supervision. Over the years, I have enjoyed our discussions of various topics and have learnt considerably from his careful articulation of arguments. More than his skills as a scientist and engineer, however, Greg truly cares about his students' work and more importantly the students themselves and is always approachable for discussion regardless of how busy he is with other work. Soon after my first year of graduate studies, Dr. Roi Gurka became a co-supervisor on the project. Practically, Roi's guidance on performing PIV experiments and his insight into the nature of the turbulence in our flows were invaluable. However, he brought much more than these to the project – and to me personally. His scientific exuberance and curiosity are contagious and have consistently helped motivate me when it was most needed.

Both of my supervisors have been very kind in allowing me to travel to several different places to present our work at a range of international conferences. These have been educational from the standpoint of the work presented, but more so in the eye opening experiences offered exclusively through travel. For these experiences, I am most grateful. However, I am most thankful to them for allowing me to be with my mother, and the rest of my family, in Winnipeg as she lost her battle to cancer in 2007.

The year 2011 marks the completion of my Ph.D. degree; however, much more importantly it marks the year I married the love of my life. I am exceedingly thankful that Lisa has stood by me as I worked through the completion of my thesis and I look forward to standing by her for the rest of our lives.

I have been fortunate to experience the ups and downs of graduate studies with fellow students. In particular I want to thank Dave, Partha and Tom who have been enjoyable sounding boards over many forms of drink. I also want to thank the technicians and students at the wind tunnel for assisting me during my various experimental programs.

Table of Contents

List of Tables

List of Figures

List of Appendices

List of Nomenclature and Abbreviations

BLWTL	Boundary Layer Wind Tunnel Laboratory
PIV	Particle Image Velocimetry
POD	Proper orthogonal decomposition
t	Model thickness
c	Model chord
c/t	Elongation ratio (also used as chord-to-thickness ratio)
U_∞	Free stream velocity
f	Frequency
St	Strouhal number, $St = f\,t/\,U_\infty$
Γ	Circulation
ω_z	Spanwise vorticity
ΔA	Discrete area defined by PIV grid
$x_{r,LE}$	Flow reattachment at the leading edge
$x_{r,W}$	Flow reattachment in the wake
$\mathrm{Re} = Ut/v$	Reynolds number
v	Kinematic viscosity
ρ	Density
L_p	Distance between the pressure minimum and $x_{r,W}$
$u'v'$	Reynolds shear stress
$u'u'$	Reynolds streamwise normal stress
C_p	Pressure coefficient
C_{pb}	Base pressure coefficient
$S(f)$	Estimate of the power spectral density
C_D	Sectional drag coefficient
C_L	Sectional lift coefficient
γ	Leading edge separation angle
τ	Time
R	Correlation coefficient
T	Time lag (cross-correlation)
Δx	Spatial lag (cross-correlation)

β	Flow angle
a	Coefficient in the POD
ϕ	Mode (eigenfunction) from POD
λ_j	Eigenvalue of POD mode
Λ	Wavelength of vortex shedding
α	Phase of vortex shedding cycle
f_t	Torsional frequency
fps	Frames per second
U_r	Reduced wind speed, $U_r = U_\infty / f_t t$
Δt	Time delay between two PIV images
θ	Wake momentum thickness
λ_{ci}	Swirling strength
Θ	Angular displacement of model during flutter

Preface

The motivation behind the work presented herein is the susceptibility of long span suspension bridges to wind. These architecturally impressive structures are inherently flexible and have necessary constraints on the geometry of their bridge decks. The combination of the aerodynamics of the bridge deck cross-section and the wind has been known to produce significant oscillations. Although there are several examples of wind-induced motion of suspension bridges, the most famous is the collapse of the Tacoma Narrows Bridge in 1940. After the bridge had collapsed, the best aerodynamicists from around the world examined the bridge in wind tunnels to try and understand why this structure had failed so dramatically. Early reports attributed the failure to resonance between a Kármán vortex street and the fundamental frequency of the structure (refer to Billah and Scanlan, 1991 for a thorough historical account). It was eventually discovered that the actual failure mechanism was similar to an instability found a few years earlier in airplane wings called flutter. Since the collapse of the Tacoma Narrows Bridge, wind tunnels have been used to ensure that new bridges do not suffer from the flutter instability.

Another part of the testing regimen for new long span suspension bridges seeks to ensure that the vortex-induced vibrations (VIV) – incorrectly thought to be the original cause of the failure of the Tacoma Narrows Bridge – are also minimal or non-existent. These types of vibrations occurred as recently as 1998, when prior to the opening of the Storebælt Bridge, oscillations of significant amplitude were observed (Larsen et al., 2000). Although these vibrations were predicted using wind tunnel testing, the ability to properly anticipate and simulate the structural damping present in the completed structure allows for undesired discretion when interpreting the results of wind tunnel tests. Vortex-induced vibrations are not limited solely to long span suspension bridges, however, and have been observed in many flexible bodies that shed periodic vortices such as chimneys and offshore oil platforms (Bearman, 2009). These shapes are generally of circular cross-section and much of the research has focused on this particular geometry.

Although there is a significant body of knowledge on VIV of circular cylinders, it is unclear how much can be applied to bodies typical of bridge deck cross-sections. These bodies have leading edge flow separation, followed by the reattachment of the flow along the deck and subsequent trailing edge separation. Even for the relatively simple case of circular cylinders, there is a significant parameter space including damping, mass, stiffness, wind speed, etc. The interested reader is referred to the recent study of Morse and Williamson (2009) for an examination of different parameters which affect VIV of circular cylinders. Although the parameter space for VIV of circular cylinders is large, the size of the parameter space grows considerably for elongated bluff bodies. The almost infinite possibility of shapes and aspect ratios of suspension bridge decks reveal the increased complexity of these shapes. In the study of VIV, there are two main values which are of considerable importance: the shedding frequency and the resultant amplitude of vibration. Both of these are desired quantities for bridge designers; however, currently, only case specific wind tunnel testing is capable of revealing this information.

The work presented in the following presents the existing knowledge of the aerodynamics of these elongated bluff bodies. However, as will be discussed, there is little known about the vortex shedding mechanisms of these bodies at higher Reynolds numbers. In Part I, the flow and pressure data from several different experiments on elongated bluff bodies are presented and discussed in light of the physical mechanisms of vortex shedding. This study represents a necessary step towards the understanding of the wakes of these bodies once they become dynamically mounted. In Part II, a state-of-the-art Particle Image Velocimetry system is developed to study the flutter instability. With the data obtained using this system, information about the vortices is used to clarify some recent misconceptions about how leading edge vortices contribute to the flutter instability. The field of long span bridge aerodynamics is complex due to the nature of the geometries involved and it is the hope that future studies can benefit from the work of a fundamental nature provided herein.

Part I The mechanisms of vortex shedding from elongated bluff bodies

Introduction to Part I

Kármán vortex shedding is a resilient phenomenon. From low to high Reynolds numbers, the phenomenon persists even though the nature of the process changes significantly (Roshko, 1993). The focus of much of the research in this area has been on relatively "short" bluff bodies, where the term short is used to indicate the streamwise length of the body compared to its cross-stream dimension. The circular cylinder, as an example of short bluff bodies, has received considerable attention due to its simple geometry and the many applications in engineering design. For comprehensive reviews of the flow around circular cylinders, the reader is referred to Williamson (1996) and Zdravkovich (1997). However, vortex shedding occurs for bodies with significantly different geometries as well, one example being long-span bridges. The research presented in this part is inspired by the Storebælt Bridge. When it opened in 1998, the $3 billion (USD) Storebælt Bridge in Denmark was the longest suspension bridge in the world. Prior to opening, the bridge experienced low frequency, high amplitude oscillations which required the addition of turning vanes to alter the vortex shedding characteristics to mitigate the instability (Larsen et al., 2000). Not all bridges exhibit these dangerous oscillations because specific cross-section geometries create characteristically different oscillating wakes; however, these issues have been common enough (e.g., Battista and Pfeil 2000; Larsen et al., 2000; Fujino and Yoshida, 2002) that the problem merits greater consideration. One of the challenges is that these "elongated" bluff bodies have leading edge flow separation, followed by reattachment along the body and subsequent separation at the trailing edge. The reasons why one shape sheds vortices in a different manner to another are not well understood.

For shorter bluff bodies, Gerrard (1966) has described the mechanism by which vortex streets are formed. His conception of the Kármán shedding phenomenon (which was later verified experimentally by Green and Gerrard, 1993) is that the vortices are formed alternatively by the interaction of the two separated shear layers via entrainment into the growing vortex. This entrainment of vorticity eventually cuts off the growing vortex at the point that it is shed from the body. Thus, it is expected that altering the separated shear layers will lead to significantly different vortex street characteristics. This notion

has been exploited in the field of flow control over bluff bodies. Choi et al. (2008) review several studies where the goal is to alter the vortex street wake such that the drag and/or the fluctuating lift force is decreased. The issue of flow control is closely linked with the persistence of Kármán shedding. In their study on the control of the wake behind a body with a significant three-dimensional geometric disturbance along the trailing edge, Tombazis and Bearman (1997) found periodic vortex shedding at Reynolds numbers above $2x10^4$. They found that even though the spanwise coherence had dropped significantly, the wake was able to organize into alternating vortices – albeit in four possible modes. At lower Reynolds numbers, Strykowski and Sreenivasan (1990) as well as Dipankar et al. (2007), show that a control cylinder placed in one of the separated shear layers is not always enough to suppress the phenomenon. It has also been observed that with Reynolds numbers on the order of 10^7, vortex shedding from a circular cylinder persists (Roshko, 1961). At these Reynolds numbers, the boundary layer on the circular cylinder transitions to turbulence before separation and the flow is highly three-dimensional, yet there is a distinct periodicity in the wake. Elongated bluff bodies are typified by leading edge flow separation. This flow separation represents a departure from the case of an aerodynamic leading edge and can thus be thought of as type of flow control. The manipulation of the leading edge geometry is a form of passive flow control whose parameter space is large. The many parameters which might affect the wake of elongated bluff bodies include: Reynolds number, elongation (chord-to-thickness) ratio, leading edge geometry, trailing edge geometry, asymmetries, etc. Within this vast parameter space, the rectangular cylinder has received the greatest interest.

At present, there is a relatively thorough understanding of the flow around rectangular cylinders at low Reynolds numbers ($Re < 2000$). Nakamura and Nakashima (1986) found that there was an instability at low Reynolds numbers which controlled the shedding of vortices from the leading edge. They called this instability the Impinging Shear Layer Instability since similar instabilities had been found for cavity flows (e.g., Rockwell and Naudascher, 1979). Later researchers found that it did not have to be an impingement of the separated shear layer with the trailing edge, but that the passage of leading edge vortices past the trailing edge was enough to complete the feedback loop and therefore renamed the instability the Impinging Leading Edge Vortex (ILEV)

instability (Naudascher and Wang, 1993). This instability represented the general understanding of elongated bluff body flows until Hourigan et al. (2001) showed the importance of trailing edge vortex shedding (TEVS) to the overall process. Mills et al. (2003) found that, for a perturbation applied far from the natural shedding frequency, the leading edge vortices shed at the perturbation frequency; however, in this case, trailing edge vortex shedding was suppressed due to the out-of-phase interactions with the leading edge vortices. At higher Reynolds numbers, it is well known that the ILEV instability is suppressed (e.g., Nakamura et al., 1991); however, there remains little information on possible mechanisms of wake formation at these elevated Reynolds numbers.

Elongated bluff bodies at higher Reynolds numbers represent numerous engineering applications from heat exchanger fins to the decks of long-span suspension bridges. Several case studies exist for individual design purposes (e.g. Diana et al., 2010); however, few studies exist of a more fundamental nature. The work of Parker and Welsh (1983) remains a benchmark study in which they found a wide range of elongation (or chord-to-thickness) ratios, c/t, where there was no detectable vortex shedding, $7.6 < c/t < 16$. The experiments of Parker and Welsh (1983) were all performed for rectangular cylinders with Reynolds numbers $O(10^4)$. The more fundamental work at these Reynolds numbers is found largely in two separate categories since there are two separate phenomena which make up this class of flows: leading edge separating-reattaching flows and trailing edge vortex shedding. Separately, each of these phenomena has received considerable attention. Discussion on each contextualizes the current study with the trailing edge vortex shedding process already having been described above.

The case of separating-reattaching flow was studied by Roshko and Lau (1965) who found that for almost all leading edge separation angles, the pressure data can be collapsed within the separation bubble following suitable normalization of the pressure and scaling of the data by the mean reattachment length, x_r. This result was subsequently shown by Ram and Arakeri (1990) and Djilali and Gartshore (1991), the former of which showed that, while the fluctuating pressures generally cannot be scaled in this way, the peaks of fluctuating pressure all occur at the same position relative to the mean

reattachment length as well. More information on the temporal variation of leading edge separation bubbles was found by Cherry et al. (1984) using an "infinite" blunt nosed plate at a Reynolds number $O(10^4)$. They found that vortices where shed from the separation bubble at the leading edge. However, there was no periodicity to these shed vortices. Castro and Epik (1998) show significant departures in the turbulent stresses for a boundary layer after separation-reattachment compared to a turbulent boundary layer having the same boundary layer thickness which has not separated. Some of the turbulent stresses were shown to be comparable in magnitude after 6.5 times the reattachment length; however, the profiles of the higher-order moments were always observed to be influenced by the leading edge separating-reattaching flow. As previously discussed, the leading edge separating-reattaching flow is only one part of the flow around elongated bluff bodies. The geometry of elongated bluff bodies cannot be considered "infinite" in length due to the trailing edge vortex shedding. In light of the results of Castro and Epik (1998), the trailing edge vortex shedding is expected to be significantly impacted by the leading edge separating-reattaching flow since they show that the leading edge flow approaching the trailing edge cannot simply be considered as conventional turbulent boundary layers.

The state of the trailing edge boundary layers was recognized as important early on as Fage and Johansen (1928) and Roshko (1954a) examined the effects of geometry on the vortex street wake parameters in light of the state of the separated shear layers. Roshko (1954a) observed that as a body becomes bluffer (i.e., for a larger separation angle) the recirculation region becomes larger and the shedding frequency decreases. These results were explained on the basis of the free streamline-based, notched hodograph theory (Roshko, 1954b). However, Roshko noted that these trends may not be applicable for bodies with significant boundary layer thickness or, in other words, when the separated shear layers can no longer be thought of as infinitesimally thin vortex sheets. Thus, for elongated bluff body flows, where the flow has separated and reattached prior to the trailing edge, there is expected to be a significant influence of the trailing edge boundary layers on the vortex street wake.

It is now well known that the geometry of the body has a significant effect on the wake

which develops for short bluff bodies (e.g., Wygnanski et al., 1986; Ferré and Giralt, 1989; Kopp et al., 1995; Kopp and Keffer, 1996a,b). However, the information available on the effects of geometry for elongated bluff bodies is much scarcer. Nguyen and Naudascher (1991) made single point velocity measurements behind elongated bodies with different leading and trailing edge shapes. Of interest here are four of their models, with constant elongation ratio (c/t = 10), which are the four possible permutations of square and semi-circular-edges at the leading and trailing edges. They remark that the leading edge has a more significant effect than the trailing edge on the vortex shedding wake. There is also work in the study of duct resonance (Welsh et al., 1984 and Stokes and Welsh, 1986), which uses similar shapes and finds that changing from a square leading edge to a semi-circular leading edge alters shedding more significantly than when the trailing edges are altered. From the published literature it is clear that for rectangular cross-sections, the leading edge vortices are essential to the formation of the wake; however, for streamlined leading edges, where there are no leading edge vortices, shedding must be governed by the trailing edge. The importance of the flow and boundary conditions between these two limiting cases is unknown. It is the objective of the following studies herein to describe both qualitatively and quantitatively the physical mechanisms of the transition between bodies which are leading edge dominated and trailing edge dominated.

The balance between the leading edge separating-reattaching flow and the trailing edge vortex shedding must control the resultant wake dynamics. However, as alluded to above, the balance between bodies which are leading edge dominated and those that are trailing edge dominated is relatively unexplored. This balance is addressed through three separate studies. In Chapter 1, the experimental details of all the studies carried out are presented. Chapter 2 explores the recirculation region in the near wake of three symmetric elongated bluff bodies. This is the region where the trailing edge vortex development occurs (Gerrard, 1966) which implies that an understanding of the dynamics of this region is imperative going forward. In Chapter 3, several different leading edge geometries are evaluated to understand the effect of geometry on the overall development of the flow. This study explores the magnitude and frequency content of the aerodynamic forcing as well as the three-dimensionality of the flow as the leading edge

geometry changes. The third study, Chapter 4, uses proper orthogonal decomposition on the wakes of three elongated bluff bodies to quantify features common to these wakes. Through these studies, a more thorough understanding of the vortex shedding wakes of these bodies is developed. Emphasis is placed on the understanding of the physical mechanisms related to wake development. The knowledge of the physical mechanisms is then related to the practical application of long span suspension bridges. For bridge designers mindful of vortex-induced vibrations, the aerodynamic loading is important; however, understanding of the shedding frequency variation is of paramount interest. Currently, there is no understanding of why different bridge deck cross-sections shed vortices at one frequency or another due to the limited understanding of the wake formation mechanisms of elongated bluff bodies at higher Reynolds numbers.

Chapter 1

Details of experiments

The work presented herein is based on the results of an extensive experimental program. Many different datasets are discussed and presented in the following sections. In this section, the various experimental set-ups used to obtain these datasets are presented.

1.1 Symmetric models

1.1.1 *Model details*

The experiments were carried out in a 0.46 m x 0.46 m cross section by 1.5 m long test section of an open return wind tunnel at the Boundary Layer Wind Tunnel Laboratory (BLWTL) at the University of Western Ontario. The turbulence intensity in the wind tunnel is approximately 0.8% and the flow is uniform across the test section to within 1% of the free stream. Three smooth, elongated bluff bodies with distinct leading and trailing edge geometries were tested. Each model had a chord-to-thickness, or elongation ratio, of 7. The three models were symmetric about the streamwise direction as well as symmetric about the vertical axis. The models had leading and trailing edges of square, triangular and semi-circular shape, as shown in Figure 1.1. This selection of body geometry was made to ensure that one model had significant leading edge vortices (the square-edged model); one model would be governed by strong trailing edge shedding (the circular-edged model) and another model that would reflect an intermediate case between the other two. The effects of the geometry of the leading and trailing edges were not isolated from each other because of the choice to make the models symmetric, since the ultimate use of this information pertains to bridge aerodynamics.

As previously stated, the models used are nominally smooth due to the choice of construction material. Song and Eaton (2002) show that surface roughness can have a pronounced effect on a boundary layer; however, they note that even significant roughness on the surface had a negligible effect on the separated flow in their experiments. Therefore, roughness effects are expected to be negligible in the current work due to the choice of materials and the significant separation at the leading edge.

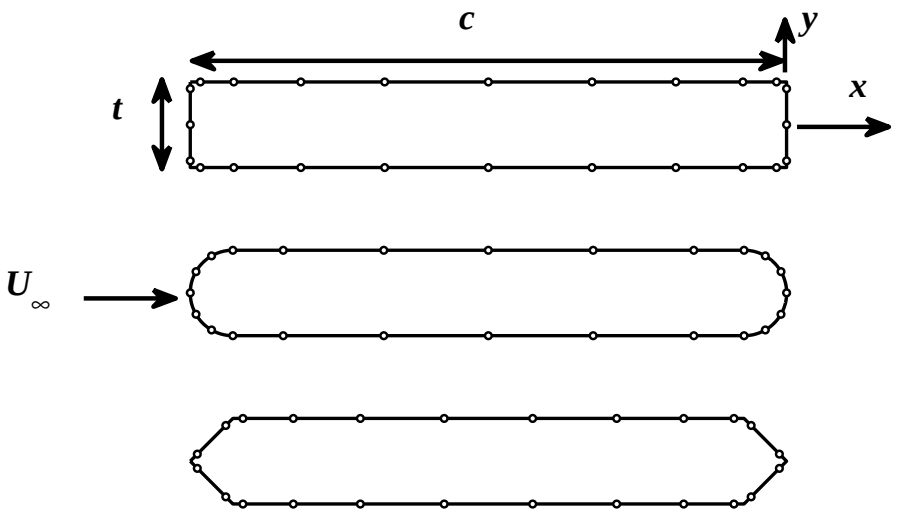

Figure 1.1. Sketches of the three model cross-sectional geometries with flow field co-ordinate system. Markers indicate location of pressure taps. From top to bottom: square-, circular- and triangular-edged cylinders.

Each model was mounted horizontally in the mid-plane of the working section, approximately 0.3 m downstream of the inlet. Spanning the full width of the working section and securely fastened to the glass windows of the tunnel walls on each side, the span-to-thickness ratio of all three models was 18. The thickness of each model was t = 25 mm so that the blockage ratio was 5.4%. This level of blockage is similar to other studies (e.g., Cherry et al., 1984) and the results are not corrected for blockage effects. The origin of the coordinate system coincides with the mid-height and the trailing edge of each cylinder as shown in Figure 1.1. Except as otherwise noted, this co-ordinate system is maintained throughout the studies using these geometries. The tunnel speed was set to 17.8 m/s yielding a Reynolds number of $3\text{x}10^4$, based on t, for the majority of the experiments. However, to gauge the effect of Reynolds number variations pressure measurements performed across a range of Reynolds numbers ($\text{Re} = 1\text{x}10^4 – 3\text{x}10^4$).

1.1.2 *Surface pressure measurements*

The models were each instrumented with 24 pressure taps positioned around the body surfaces at mid-span. The tap locations on each model are shown in Figure 1.1, each of which was connected to a pressure scanner via a tubing system. The tubing system had a frequency response which was flat to beyond 200 Hz. The frequency response is

determined by providing a known random pressure signal to the tap and measuring the amplification of the signal over the spectrum of frequencies. During the experiments, the pressure scanners ensure that all of the taps are measured nearly simultaneously and, in this case, were sampled for 150 seconds at 400 Hz while being low pass filtered at 200 Hz. Using a pressure scanner system, the measurements were taken within the sampling cycle with a maximum time lag of 15/16 of the sampling rate. In this case, the maximum time lag is approximately 2.3 msec. Surface pressures were integrated around the surface of the body at each point in time to obtain estimates of the sectional lift and drag time series (neglecting viscous drag), after the time lag was corrected by linear interpolation of the data within the same sample cycle. This method is known to yield accurate force integrations when compared with load cell measurements (Ho et al., 1999), and hot-wire spectra in the wake validated that the measured frequencies were unaffected by pressure scanner time lags.

1.1.3 *Particle Image Velocimetry measurements*

The PIV system used in this study consists of a 120 mJ/pulse double head Nd:YAG laser operating at 15 Hz. To capture the images, a 1016 x 1000 pixel CCD double exposure camera with an 8-bit dynamic range was used. A Laskin nozzle atomizing olive oil was used to seed the flow. The mean diameter of the seeding particles was approximately 1 μm (Echols and Young, 1963).

The images were correlated using the FFT cross-correlation method with 32 x 32 pixel interrogation windows and 50% overlap. Using a global standard deviation filter followed by local mean and median filters, erroneous vectors were identified and rejected. Typically this filtering process resulted in less than 5% of the vectors being removed. The data were then interpolated to fill the locations where velocity data were rejected. Due to the limit of the hard disk speed on the acquisition computer the sampling frequency was reduced; thus, each of the 5000 total vector maps acquired for each model, at each location, was treated as an independent sample.

The details of the PIV measurements made in this study vary considerably due to resolution requirements in the different regions of the flows. For the leading edge

measurements, a different resolution was used for each model to capture as many details as possible of the separation bubble from separation to reattachment. The field of view for the trailing edge measurements was large enough to ensure approximately 30 data points in the vertical direction along the trailing edge of each model as well as to characterize the trailing edge boundary layers. In the wake, a field of view of one chord length was desired, which meant a relatively lower resolution. The time separation between image pairs in the PIV experiments was adjusted to yield typical particle image displacements of 5-6 pixels.

A significant challenge of the PIV experiments is measuring close to the body. As is discussed later (see §2.2.2), the recirculation region at the leading edge of the circular-edged body could not be measured in the current set-up. For the other two models, higher resolution (as small as 93 μm/pixel for the leading edge of the triangular-edged model) was obtained to ensure sufficient data could be taken within the separation bubble. It was observed that the combination of seeding, illumination and camera sensitivity were all sufficient to achieve sufficiently high signal-to-noise ratios (average of approximately 2.5) in this region. The first row of data above the body were always disregarded since it was observed that the signal-to-noise ratio was low (i.e., close to 1). Another problem close to body surfaces is reflection; however, this was mitigated by positioning the centre of the camera to coincide with the surface of the body which eliminated a significant portion of the reflected light from the body surface. The data were measured on only one side of the body at a time since the laser created a shadow thus, the positioning of the camera in this way meant half of the pixel array was not used; however, the limiting of reflected light was necessary to ensure data of sufficient quality.

1.2 Models with varying leading edge geometry

1.2.1 *Model details*

The model used in the current study has been designed to accommodate different nosing geometries. A nosing is defined as having a constant cross-section which is fitted to either the leading or trailing edge surfaces. In this study, 5 different leading edge noses were used in addition to the base model; these noses are shown in Figure 1.2.

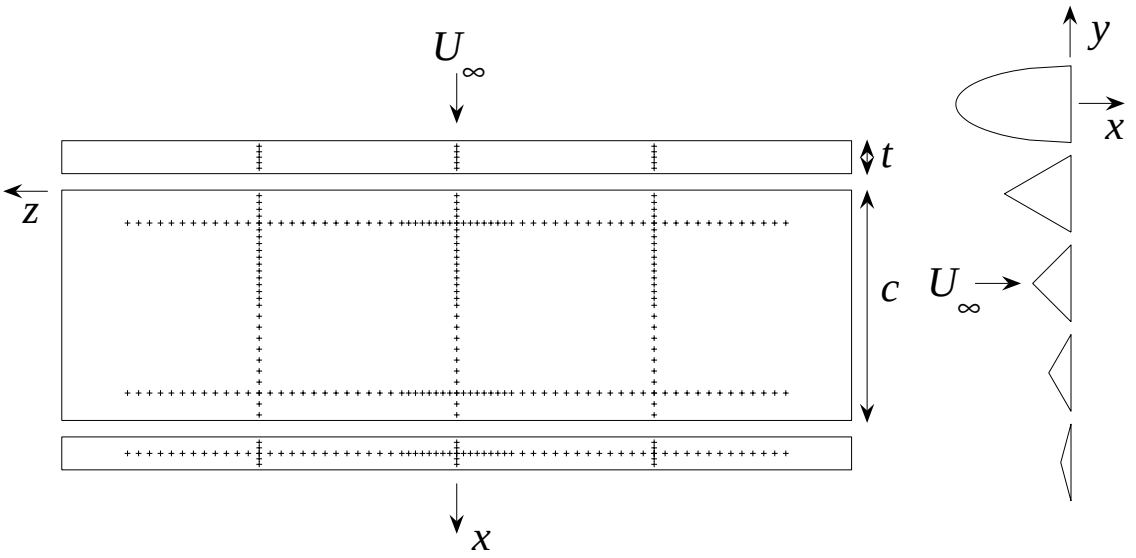

Figure 1.2. Schematic of the model showing the pressure tap layout (+ symbols) and the different noses used in the experiments. The leading and trailing edges have been folded out to demonstrate the full tap layout.

The base model is of rectangular cross-section measuring 76.2 mm in thickness, t, with a chord-to-thickness ratio of $c/t = 7$. This elongation ratio is kept constant across all tests; however, the length of the nose is not considered in the measurement of the chord. The noses used in the current study include an elliptical nose, with a 3:1 axis ratio, and noses of triangular cross-section with interior angles ranging from 60°-180° at 30° increments.

The co-ordinate system used throughout the current study is shown in Figure 1.2. The y-axis is centred along the span of the model, the z-axis is centred vertically on the model and in the streamwise direction, the x-axis begins after the nose. This streamwise location corresponds with the fixed separation points for all of the noses except for the one of elliptical cross-section (which has no leading edge separation).

The model is fitted with 512 pressure taps. The basic layout of the taps is shown in Figure 1.2. As is shown in Figure 1.2, the leading edge has 3 rows of 5 taps each. The tap spacing used for the base case is shown therein and the same vertical spacing is projected onto each nosing. The spacing of the leading edge taps is preserved on the trailing edge surface in addition to a row of taps along the span. Each spanwise row of

taps consists of 67 taps spaced 25.4 mm apart towards the edge of the model and spaced at 15.9 mm closer to the centre. To obtain sectional loading data, three streamwise loops are used comprising the taps on the leading and trailing edge surfaces as well as 27 taps on the top and bottom surfaces. These taps are spaced at 15.9 mm within approximately 3.5*t* of the leading edge and 25.4 mm from this location until the trailing edge. The density of taps was chosen so that the data were better spatially resolved within as much of the leading edge separation bubble as possible. Although not shown in Figure 1.2, the pressure tap layout on the bottom mirrors that on the top.

In the literature on circular cylinders, and short bluff bodies in general, there is considerable discussion about the inherent three-dimensionalities of bluff body experiments. Roshko (1993) noted that certain extrinsic characteristics can alter the three-dimensionality of a given experiment. The two main extrinsic characteristics which are focused on in this regard are aspect ratio and end plates. There is some overlap between these two issues in the design of such an experiment. In the present experiments end plates are used which extend 0.57 m into the wake ensuring that they protrude into the wake for at least one complete vortex shedding cycle. The aspect ratio is relatively high for comparable studies with a span-to-thickness ratio of 24. However, unlike the plethora of data regarding circular cylinders and aspect ratio, there remains little on its effect for elongated bluff bodies. The significant leading edge separation for these bodies and its interaction with the wall boundary layers is an additional complication to the case of shorter bluff bodies and is shown to be sensitive to many parameters (Castro and Epik, 1998). In the present study, the model is instrumented sufficiently to describe the three-dimensional nature of the flow thus this topic will be returned to when the data are presented (§3.1.3).

1.2.2 *Wind tunnel tests*

The tests were performed in Tunnel II at the Boundary Layer Wind Tunnel Laboratory. This tunnel is of closed-circuit design and includes a test section measuring 1.83 m high by 3.35 m wide. The length of test section is 39 m; however, the testing was all performed approximately 2 m from the inlet. At this location, the turbulence intensity is measured less than 1% and the velocity is uniform to within 1% away from the walls.

The model was fitted with end plates, as discussed above and was mounted in the middle of the tunnel both vertically and horizontally. The free stream speed was adjusted to yield 8 different Reynolds numbers ranging between $4x10^4 – 7.5x10^4$ (based on thickness) in increments of $0.5x10^4$.

The pressure taps were connected to multiplexing pressure scanners. A total of 12 taps were connected to each scanner and each tap was sampled at 500 Hz. The tubing system used to connect each tap to the scanners has been tested to have a frequency response which is flat to approximately 200 Hz. Thus, the data herein have been low-pass filtered at 180 Hz. For each of the nose configurations (6 in total) and each Reynolds number, the pressure data are sampled for 120 sec. The pressure data are interpolated in time at each time step, which is necessary due to the multiplexed nature of the measurement system. Phase lag tests have been performed on this system to ensure that effects from this procedure are negligible. The reader is referred to Ho et al. (1999) for more details on the pressure scanning system.

Chapter 2

Features of the turbulent flow around symmetric elongated bluff bodies*

In this chapter, the flow around three symmetric elongated bluff bodies is quantified with particular focus on the recirculation region. In his work on a circular cylinder in free stream turbulence, Gerrard (1966) presents two length scales related to the recirculation region which are important in determining the vortex shedding characteristics. The first is the often referenced formation length (i.e., the length of the recirculation region) and the second is a more ambiguous scale referred to as the diffusion length. The notion of the diffusion length, according to Gerrard (1966), is that the more "diffuse" a shear layer, the more difficult it will be for the two separated shear layers to interact. He extended this notion, proposing that the more difficult it is for the two shear layers to interact, the longer the time required for this interaction to occur and, as a result, the shedding frequency should decrease. The recirculation region, where all of this interaction takes place, is then of paramount interest to understand the phenomenon.

For elongated bluff bodies there is an additional region that is important since there is leading edge separation and reattachment. For example, it is well known that the wake of rectangular cylinders is governed by the presence of leading edge vortex shedding (e.g., Nakamura et al., 1991). However, it remains unclear what happens as the relative balance between leading and trailing edge shedding is altered. As Gerrard (1966) points out, there must be at least two length scales that govern; however, it is unknown how many length and time scales are required to understand the wakes of elongated bodies.

A force balance is used in this chapter to quantify the different dynamics in the recirculation region of the three tested bodies. For shorter bluff bodies, Balachandar et al. (1997) show markedly different characteristics between several geometries in their

* A version of this chapter has been published in the Journal of Fluids of Structures. The full reference is cited herein as Taylor et al., 2011. Copyright release is provided in Appendix A.

force balance analysis of the recirculation region. Since these balances were performed on short bluff bodies the shear layers were consequently thin. It is anticipated that the thick boundary layers and leading edge vortices shed from elongated bluff bodies will be reflected in all characteristics of the vortex street wakes as well as the force balance of the recirculation region.

The flows studied herein, where there are thick shear layers as well as leading edge vortices present at the trailing edge, is the type of flow experienced by the decks of long-span suspended bridges. It is the objective of the current study to develop a quantitative understanding of the leading edge separated flow, the relatively thick trailing edge boundary layers and the subsequent vortex street wakes of elongated bluff bodies. To this end, the flows around three elongated bluff bodies are examined comparing three separate cases: one in which leading edge vortex shedding governs, one in which trailing edge vortex shedding governs and one where both types of vortex shedding are significant. The results in this chapter are based on the PIV and pressure measurements of the three symmetric bluff bodies. For a detailed explanation of the experimental setup the reader is referred to §1.1.

2.1 Vortex shedding

In later sections, the flow around the body and the flow in the near wake are examined separately; however, it is useful to first quantify the distinctions observed between the models in a broader context. The intermediate wake, in effect, reveals an ensemble of the flow around the body and that in the near wake. Removed from the complexities within the near wake, it is possible to observe distinctions between vortex characteristics in this region. These characteristics are examined in this section; however, a fundamental parameter for bluff body wakes is the shedding frequency which is determined first in the following.

2.1.1 *Shedding frequency*

The pressure data for each cylinder were integrated to find the sectional lift fluctuations. The shedding frequencies, f, were identified from peaks in the power spectra of the lift coefficients for each model (shown in Figure 2.1c) and used to calculate the individual

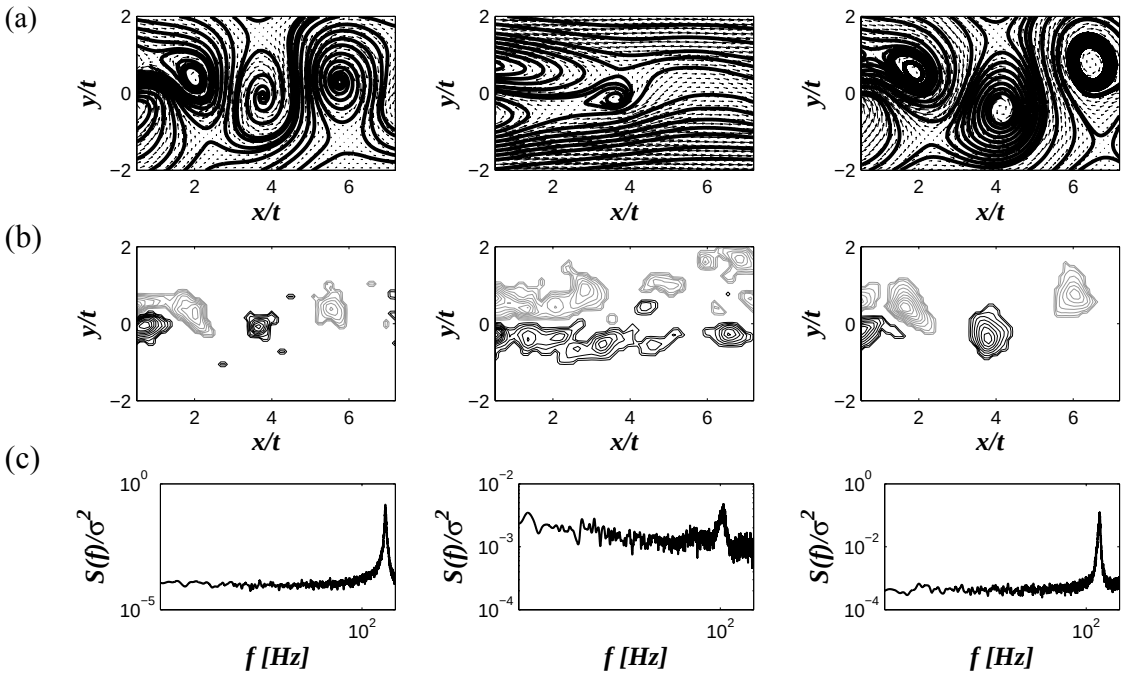

Figure 2.1. (a) Ensemble averaged wake of (left to right): circular-, square- and triangular-edged cylinders. Convection speed of $0.88U_\infty$ is subtracted from triangular- and circular-edged wakes and $0.55U_\infty$ is subtracted from square-edged wake. (b) Instantaneous vorticity maps in the wake (order matches top row). Black lines are contours of positive vorticity with gray lines contouring negative vorticity. (c) Power spectra densities of the lift coefficient for each model (order matches top row).

Strouhal numbers. Using the uniform free stream, U_∞, and fixed model thickness, t, the Strouhal number is defined as, $St = ft/U_\infty$. The resulting Strouhal numbers are listed in Table 2.1. The Strouhal numbers are distinct for each model, ranging from 0.15 for the square-edged model to 0.24 for the circular-edged model. These results correspond well to others presented in the literature. Nguyen and Naudascher (1991) report a value of 0.26 for a circular-edged model with an elongation ratio of 7 and free stream turbulence intensity of 4.5%. Nakamura et al. (1991) indicate that for low Reynolds numbers ($Re < 1000$) a rectangular cylinder with $c/t = 7$ has a Strouhal number based on chord of 1.1 – this translates to a Strouhal number based on thickness of 0.16.

The spectral peaks for the circular- and triangular-edged bodies are significant and narrow-banded. However, the square-edged body has a small amplitude, broad-banded peak in the lift spectrum (Figure 2.1c). Furthermore, there is no discernable peak in the spectrum of the drag coefficient for the square-edged cylinder (not shown). These results agree with those shown by Parker and Welsh (1983) where the measured spectral peak in

Table 2.1. Measured flow parameters for vortices ensemble averaged at $x = 2t$.

Edge Shape	St	U_c/U_∞	A/t^2	$\lvert\Gamma\rvert/U_\infty t$
Circular	0.24	0.8	0.95	1.2
Square	0.15	0.5	0.52	0.85
Triangular	0.19	0.7	0.78	1.7

the wake for an elongation ratio of 7.6 is subtle. Thus, although periodic vortex shedding does occur for rectangular cylinders of this elongation ratio and Reynolds number, it is intermittent and spans a relatively broad range of frequencies.

2.1.2 *Effect of Reynolds number on shedding frequency*

Roshko (1954a) showed the dependence of the Strouhal number on the Reynolds number for three different short bluff bodies. For the bodies with fixed separation points, the Strouhal number varies minimally as the Reynolds number approaches $1x10^4$ compared to the significant variations at lower Reynolds numbers. The circular cylinder does not have fixed separation points and as such is more dependent on the Reynolds number; however, Roshko (1961) shows that the Strouhal number varies little between $1x10^4$ and $2.5x10^5$. For more elongated bodies, Okajima (1982) measured the effect of Reynolds number on shedding frequency past rectangular shapes with elongation ratios between $1 < c/t < 4$. Okajima (1982) showed a strong dependence on Reynolds numbers when $Re < 5000$ with two different modes observed in this range for the rectangular cylinder with an elongation ratio of 3. However, at higher Reynolds numbers he found similar trends as Roshko (1954a) in that, as the Reynolds number approaches $1x10^4$, the variation in the Strouhal number decreases. In their study on a wide range of elongation ratios, Nakamura et al. (1991) found that for $Re > 2000$ no discernible peak could be found for elongation ratios greater than 12. In the forced and unforced experiments of Parker and Welsh (1983) they examined unforced flow in the Reynolds number range $1.48x10^4 < Re < 3.11\ x10^4$. As has been alluded to previously, they did not find any regular shedding like that present for lower Reynolds numbers (Nakamura et al., 1991) in their Reynolds number range for bodies of elongation ratios between $7.6 < c/t < 16$. They also note that they did not observe any noticeable differences in the hot-wire data across their Reynolds number range for a given elongation ratio. In the present experiments, pressure

measurements were made at several different Reynolds numbers to determine the variability of the Strouhal number. These results are shown in Figure 2.2 where it is clear that there is minimal variability of the Strouhal number with Reynolds number from $1x10^4 – 3x10^4$.

2.1.3 *Ensemble averaged wake*

With the range of Strouhal numbers observed for the three models it is expected that their wakes will also have significant distinctions. To quantify the features of these vortex shedding wakes, the PIV velocity data were ensemble averaged based on the vortices identified at $x = 2t$, downstream of the trailing edge. The vortices were identified based on the eigenvalues of the velocity gradient tensor, as proposed by Chong et al. (1990) and used on two-component, two-dimensional PIV data by Adrian et al. (2000). A square window centred at $(x, y) = (2t, 0)$ with dimensions t^2 was used as the location about which to perform the ensemble average. Each PIV frame with a vortex of adequate and like-signed circulation within this window was included in the ensemble average. The frames which were included in the ensemble were then all shifted such that the centre of the vortex identified in each window would lie on the average vortex centre position of all frames. The reason for shifting the frames was to reduce the effect of smearing typical of ensemble averages. The size of the window and the shedding frequency of each model

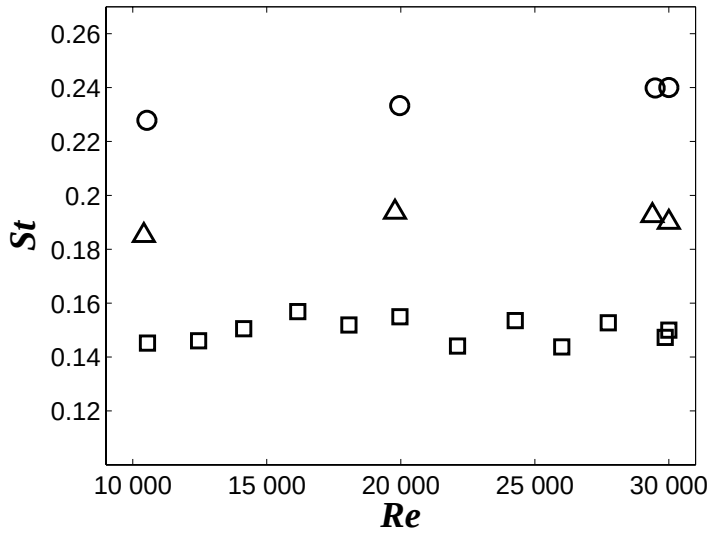

Figure 2.2. Variation of Strouhal number with Reynolds number. □ – square-, ○ – circular- and Δ – triangular-edged models.

ensured that the subset created contained between 15-20% of the entire data set meaning between 750-1000 PIV data frames. This number of frames was observed to be sufficient for convergence of the ensemble averaged statistics.

Instantaneous vorticity contours are shown in Figure 2.1b, while the vectors and streamlines of the ensemble averaged vortex wakes are presented in Figure 2.1a from the point of view of an observer travelling at $0.88U_\infty$ for the circular- and triangular-edged models and $0.55U_\infty$ for the square-edged model. Perry et al. (1982) emphasize the importance of the speed of the observer when studying streamline patterns. Thus, these frames of reference have been selected since they are the approximate convection speeds of the ensemble averaged vortices shown. Several locations were attempted in the ensemble average of the square-edged cylinder; however, a strong vortex street was not observed for any location, consistent with the instantaneous contours shown in Figure 2.1b. Instead, the pattern was of a solitary vortex about which the ensemble average was performed, such as at $x = 4t$, shown in Figure 2.1a. The pattern which emerges in the wake of the square-edged model confirms the observation from the pressure measurements that periodic vortex shedding does not occur continuously and is weak, at best.

2.1.4 *Vortex characteristics*

In this section the convection speed, area and circulation of the ensemble averaged vortices located at $x = 2t$ are presented and are listed in Table 2.1. The convection speed of the vortex is defined as the streamwise velocity at the centre of the vortex following Zhou and Antonia (1994). The circulation is estimated in the same manner as Cantwell and Coles (1983) via,

$$\Gamma = \int_S \boldsymbol{\omega} \cdot \mathbf{n}\, dS \approx \sum_{i,j} \left\langle \omega_z \right\rangle_{i,j} \Delta A_{i,j} \tag{2.1}$$

where ω_z is the spanwise vorticity at a given location and S is the area of the vortex. In this work, $\Delta A_{i,j}$ is the area created by the spacing of the PIV data grid points. The circulation of the vortex is computed by first identifying the location of maximum vorticity in the vortex. The radius is then defined by the location where the vorticity drops below 1% of its maximum. All points lying within this radius are included in the

sum of Eq. (2.1). Any approximation of circulation inherently has significant uncertainty due to the difficulty in accurately determining the boundary of a vortex and a lack of resolution of the vorticity field. Thus, emphasis is placed on the relative magnitudes for the three models.

The strength of the vortices in the wake reveals fundamental differences between the circular- and triangular-edged bodies. The triangular-edged body sheds the strongest vortices even though they are physically smaller than the circular-edged vortices. Gerrard's (1966) physical description of the mechanism of vortex shedding relies heavily on the notion of interaction between the two separated shear layers. In his work on vortex shedding in smooth and turbulent streams he found a significantly lower shedding frequency when the turbulence in the free stream was increased. Gerrard (1966) hypothesized that it was the increased free stream turbulence that led to a disruption of the interaction process. He also anticipated that if interaction between the shear layers is disrupted then there is less vorticity cancellation as well as less entrainment in the growing vortex. These have the consequences of increasing circulation and decreasing size respectively when the interaction process is disturbed. Returning to the present measurements, the triangular-edged model has stronger yet smaller vortices than the circular-edged cylinder. Although other factors are influential as well, these results could be indications of the level of interaction between the separated shear layers. This point is further addressed in later sections.

The convection speeds of the triangular- and circular-edged models are different than each other; however, they are similar to what would be expected in conventional vortex streets at this location. Their differences reflect the differences in vortex shedding frequency. However, it is observed that the convection speed of the average vortex at this location for the square-edged cylinder is quite low with a value of $0.45U_\infty$. The results of Bearman (1967) predict a minimum convection speed of $0.5U_\infty$ for vortex street wakes based on an analytic formulation using point vortices. Although there are certain failings of the point vortex method (Saffman and Schatzman, 1982) it is an interesting result since the square-edged cylinder does not form a regular vortex street in its wake. The theoretical prediction corresponds to the limit of the spacing ratio going to infinity

(Bearman, 1967) which implies that the vortices in one row are much closer together than the distance between rows. One can conceptualize that this represents a case of poor interaction between the shear layers.

2.2 Flow around the body

Elongated bluff bodies are distinguished by the separation at the leading edge and reattachment of the flow before separating again at the trailing edge. The flow separating at the trailing edge is then a significant departure from the relatively thin layers typical of the separated shear layers of shorter bluff bodies. The flow around the body must have a significant effect on the formation of the wake; however, the literature shows the strong effect of feedback for these types of shapes where the leading edge flow can be forced by the trailing edge shedding, thus completing a feedback loop between all portions of the flow (Hourigan et al., 2001). Thus, it is not straightforward to separate cause and effect of the observed flow either around the body or in the wake. While it is clear from the literature that feedback organizes temporal features of the leading edge separation bubble, it is equally apparent (e.g., Djilali and Gartshore, 1991) that the leading separation angle must play an important role in determining the scale of the leading edge separation bubble.

2.2.1 *Leading edge separation angle and reattachment length*

The leading edge separation angle is a parameter often used to gauge the "bluffness" of a given geometry (Roshko, 1954a). The separation angle is defined here as the angle that the leading edge separating streamline makes with the streamwise direction at separation. For the two bodies with fixed separation points these values are taken to be the angle between the tangent to the body at separation and the streamwise direction. For the circular-edged model, the separation angle is estimated based on the PIV measurements. These values are reported in Table 2.2.

The reattachment point is defined as the point at which the shear stress at the wall is zero, following a region of reversed flow near the wall (Tritton, 1988). The reattachment length is denoted as $x_{r,LE}$ with the additional subscript *LE* used to distinguish the leading edge reattachment from the reattachment of the flow in the wake recirculation region.

Accurate measurements of reattachment are challenging and the uncertainties are specified in Table 2.2 based on the resolution of the PIV measurements. The reattachment length is estimated using velocity profiles along the streamwise direction from the PIV data and is located at the point where the mean flow near the wall changes from reversed flow to forward flow. Thus, for the square- and triangular-edged models adequate resolution was obtained to estimate the reattachment point within one streamwise PIV grid point on either side of the values listed in Table 2.2. For the circular-edged model it proved more difficult because of its small size, therefore, it is estimated that the listed value is accurate to within two grid points.

The square-edged model has a mean reattachment length of 4.2t, the longest of the three models. Cherry et al. (1984) report that for a tunnel blockage of 5% the mean reattachment length for an infinite plate is 4.4t which compares well with the value of 4.3t found by Roshko and Lau (1965) for a similar blockage. The reattachment length is known to be quite sensitive to many parameters. For example, Castro and Epik (1998) measure a reattachment length of 7.7t on an infinite blunt nosed flat plate, and state that their aspect ratio (span/thickness ratio of 64), significantly lower blockage (1.2%), the use of end plates and a possible Reynolds number (Re = 6500) dependence are the reason for the longer separation bubble. For an infinite plate with a triangular leading edge, Djilali and Gartshore (1991) report a reattachment length of 2.4t compared with the present measured value of 2.1t. The reattachment length reported for the square-edged case by Djilali and Gartshore (1991) is also noticeably higher than that found currently and, as previously mentioned, by Roshko and Lau (1965). The reattachment length for the circular-edged body is small being 0.94t, which is similar to the reattachment length of 0.95t found by Hazarika and Hirsch (1994) in their experiments on an infinite plate with a circular leading edge. Their experiments were performed at a Reynolds number,

Table 2.2. Mean reattachment lengths, $x_{r,LE}$, and separation angles, α for the three models

Edge Shape	α [degrees]	$x_{r,LE}/t$
Circular	30	0.94 ± 0.04
Square	90	4.2 ± 0.09
Triangular	45	2.1 ± 0.06

based on thickness, of 2.4×10^4 in smooth flow with a blockage ratio of 2.3%. Therefore, the current experiments are in good agreement compared with published values in the literature.

2.2.2 *Details of the separation bubble*

In the previous section, the relative sizes of the leading edge separation bubble were determined. Ultimately, it is the shedding of this "bubble" as distinct patches of vorticity (Simpson, 1989) from the leading edge, which have significant influence as they approach the wake. This region is examined in closer detail in this section. As mentioned above, measuring the separation bubble of the circular-edged model proved difficult with the current scale of the experiment. The region of interest is too small to obtain a resolution with sufficient data points to generate profiles along the separation streamline. Thus, the comparison of the leading edge separated shear layers and separation bubbles is limited to the triangular- and square-edged models.

It has been shown in the literature that profiles of the mean surface pressure under separation bubbles can be made markedly similar with a suitable normalization of the pressure coefficients. The normalized pressure data beneath the separation bubble all collapse for thin separated shear layers if the streamwise co-ordinate is normalized by the reattachment length (Roshko and Lau, 1965). Thus, in the current comparison of velocity profiles, the reattachment length is used to scale both the streamwise and cross-stream directions.

The mean velocity profiles along the separation bubble are plotted in Figure 2.3 with the Reynolds shear stresses plotted in Figure 2.4. The velocity profiles scale well with the chosen normalization along the separation bubble, which agrees with the noted scaling of pressure underneath the bubble since these are both time-averaged quantities. However, Figure 2.4 shows that the shear stresses cannot be scaled in this way. The magnitude of these shear stresses is likely the result of both an incoherent component – due to the level of unsteadiness and flapping typical of these separated shear layers – and a coherent component due to the size and circulation of the separation bubble.

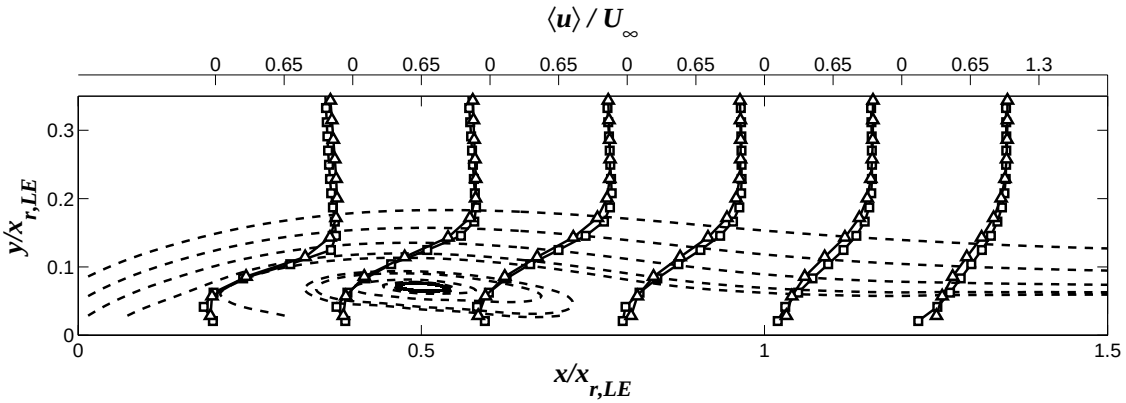

Figure 2.3. Leading edge velocity profiles: □ – square- and Δ – triangular-edged models. Vertical and horizontal dimensions are normalized by the leading edge reattachment length $x_{r,LE}$. Location of $x = 0$, in this case, is the point of separation. Streamlines (dashed) are from the separation bubble of the triangular-edged cylinder (square-edged are similar).

2.2.3 *Evidence of feedback*

For low Reynolds number cases of flow over rectangular cylinders, Mills et al. (2003) show that there is a significant narrow-band feedback resulting in the ILEV instability. As previously discussed, the current data, as well as that taken by Parker and Welsh (1983), suggest that this feedback is suppressed at higher Reynolds numbers for rectangular shapes. The spectra from the surface pressure data (not shown) support this notion. Shortly after reattachment along the body of the square-edged cylinder, there is no significant peak in the pressure spectra. However, narrow-band frequencies are observed in the pressure taps along the entire length of the body for the circular- and

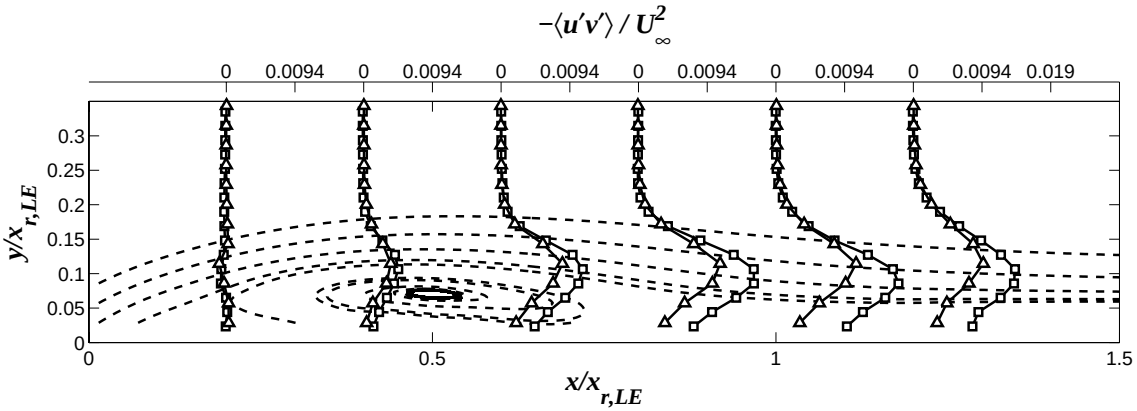

Figure 2.4. Leading edge Reynolds shear stress profiles: □ – square- and Δ – triangular-edged models. Vertical and horizontal dimensions are normalized by the leading edge reattachment length $x_{r,LE}$. Location of $x = 0$, in this case, is the point of separation. Streamlines (dashed) are from the separation bubble of the triangular-edged cylinder (square-edged are similar).

triangular-edged cylinders suggesting feedback from the trailing edge still plays a role for these shapes. However, neither the pressure data nor the PIV data are resolved well enough in time to study feedback further in the present work.

2.2.4 *Flow at the trailing edge*

In this section, the state of the flow is examined just before the boundary layer separates into the wake at the trailing edge. The trailing edge velocity profiles are shown in Figure 2.5 where it is evident that the mean boundary layer of the square-edged cylinder is significantly thicker than those of the other two models, with the development length downstream of reattachment being rather limited. The boundary layers measured by Castro and Epik (1998) on a blunt leading edge plate took $6.5x_{r,LE}$ for some of the Reynolds stresses to recover, and significantly longer for higher order moments. Thus, all of the boundary layers at the trailing edge – and the subsequent free shear layers – in the current study are affected by the initial leading edge separation. This connection is seen in the profiles of the Reynolds shear stress shown in Figure 2.6. As was expected from the work of Castro and Epik (1998), the leading edge vortex shedding and the unsteadiness of the leading edge shear layer have substantially increased the shear stresses at the trailing edge for the square-edged model. However, the triangular-edged model also shows higher levels of Reynolds shear stress than the circular-edged model.

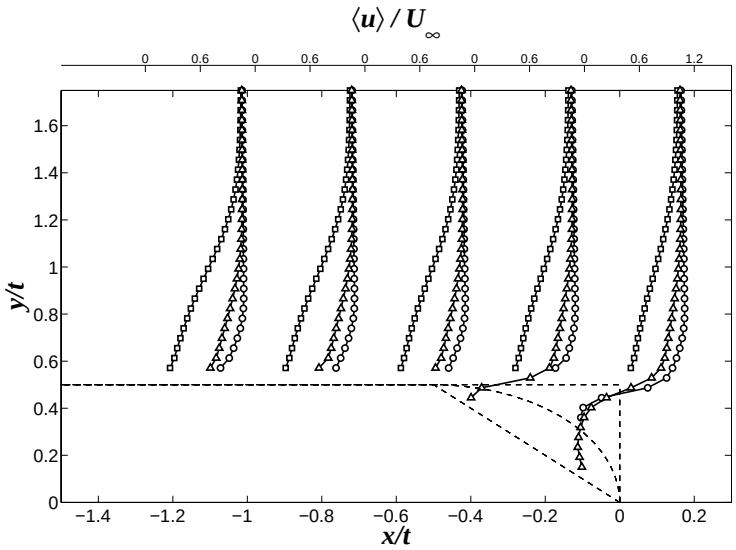

Figure 2.5. Trailing edge velocity profiles: □ – square-, ○ – circular- and Δ – triangular-edged models. Body shapes indicated with dashed lines.

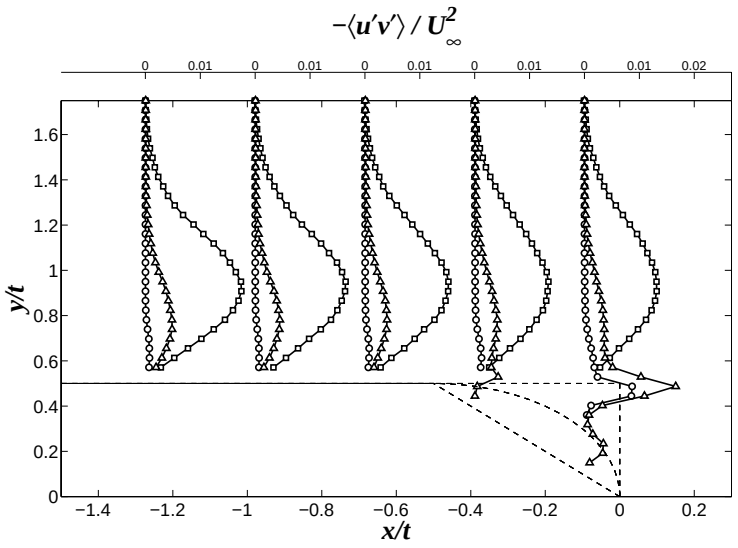

Figure 2.6. Trailing edge Reynolds shear stress profiles: □ – square-, ○ – circular- and Δ – triangular-edged models. Body shapes indicated with dashed lines.

These elevated levels of stress appear to be associated with a larger leading edge separation bubble.

2.3 Wake recirculation region

The wake recirculation region is the critical area of the flow field for determining the resultant vortex shedding parameters. The complexity of the flow approaching the recirculation region means that the separated shear layers at the trailing edge are significantly different from both those observed for shorter bluff bodies, as well as between the geometries examined herein. Due to the lack of time resolution in the PIV system, emphasis is placed on the mean and fluctuating values in the recirculation region. As has been alluded to previously, the interaction of the shear layers in the recirculation region is paramount to the wake which evolves. It will be shown in this section that the different boundary layer states play a significant role in altering the balances of the recirculation region, suggesting that the levels of shear layer interaction are markedly different for each model. A force balance applied to the wake recirculation provides a framework to examine quantitatively how the near wake varies for the three cases studied herein.

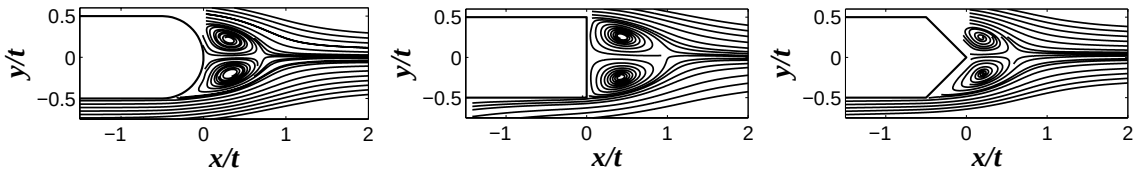

Figure 2.7. Mean streamlines along the trailing edge and in the recirculation region of each body.

2.3.1 *Force balance*

The wake recirculation region is defined by the pair of streamlines ($\psi = 0$) separating from the body at the trailing edge which join at a saddle point in the wake. The streamwise distance between the separation point and the saddle point in the wake is denoted as $x_{r,W}$. This distance is commonly referred to as a reattachment length; the additional subscript, W, is used to distinguish the wake reattachment from the reattachment of the leading edge flow onto the body. Figure 2.7 depicts the mean streamlines near the trailing edge and in the recirculation region of each model, while the lengths of the recirculation region determined from the PIV data are shown in Table 2.3. It is observed that $x_{r,W}$ is approximately the same for all three bodies in spite of the large differences in shedding frequencies. This observation deviates from the trend for shorter bluff bodies where the recirculation region gets larger for bodies with lower shedding frequency (Roshko, 1954a).

If a surface is defined by the closed, separating streamlines, $\psi = 0$, and the body, then there is, by the definition of a streamline, no mean flow entering or leaving the control surface. Following the work of Roshko (1993) and Balachandar et al. (1997), a force balance is constructed, neglecting the viscous terms which scale with Re^{-1}, as follows,

$$\frac{1}{{U_\infty}^2}\int_\psi \left(\frac{\langle p \rangle}{\rho} + \langle u'u' \rangle \right) dy + \frac{1}{{U_\infty}^2}\int_\psi \langle u'v' \rangle dx + \frac{1}{{U_\infty}^2}\int_b \frac{\langle p_b \rangle}{\rho} dy = 0 \tag{2.2}$$

where the prime denotes a fluctuation from the mean and the angle brackets denote a time average . The contour b represents integration along the base of each model and ψ refers to integration along the separation streamlines. Using notation similar to Balachandar et al. (1997), coefficients for each term are defined as follows, where U_s is the maximum

velocity in the separated shear layer (Roshko, 1993),

$$C_p = \frac{\langle p \rangle}{\frac{1}{2}\rho U_s{}^2}, \quad C_{p_b} = \frac{\langle p_b \rangle}{\frac{1}{2}\rho U_s{}^2}, \quad C_n = \frac{\langle u'u' \rangle}{\frac{1}{2}U_s{}^2}, \quad C_\tau = -\frac{\langle u'v' \rangle}{\frac{1}{2}U_s{}^2} \tag{2.3}$$

The contributions of the Reynolds normal and shear stresses to the momentum balance are shown in Figure 2.8. In the figure, the overall forces calculated for each term are equal to the area under each curve, which are denoted as F_n and F_τ for the forces corresponding to the streamwise normal and shear stresses, respectively, in Table 2.3. Note that C_n is plotted against y and C_τ is plotted against x in the figure. The pressure along the base of each model has been measured in the current experiments; however, the pressure within the flow has not. Assuming negligible contribution from the viscous terms, the sum of F_n and F_p (the force due to pressure) must equal F_τ to balance the forces, where F_p is estimated as the difference between F_τ and F_n. These contributions are listed in Table 2.3.

Table 2.3. Recirculation region parameters

Edge Shape	$x_{r,W}/t$	F_n	F_τ	$F_p \approx F_\tau - F_n$	L_p/t	$-C_{p_b}$	U_c/U_∞
Circular	1.05	0.121	0.075	-0.046	0.09	0.49	~1
Square	1.09	0.054	0.056	0.002	0.56	0.30	0.7
Triangular	1.08	0.089	0.085	-0.004	0.22	0.50	0.8

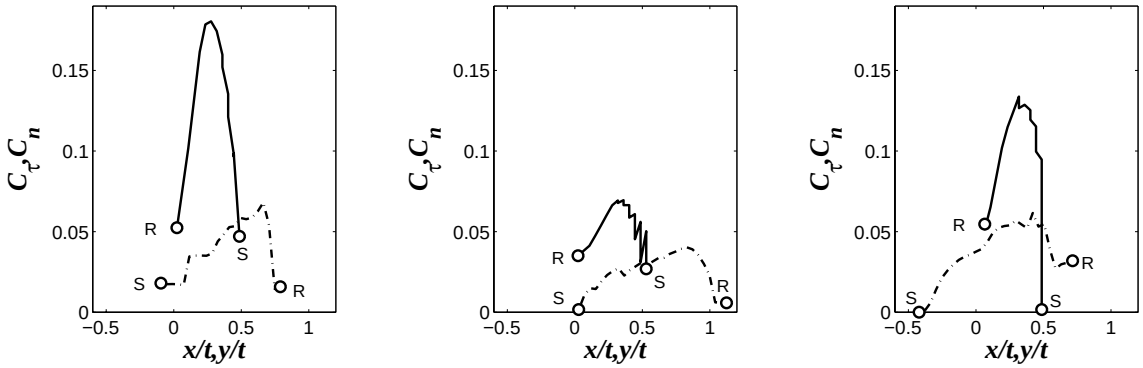

Figure 2.8. Momentum balance where the contribution to the normal stress, C_n, is the solid line and the contribution to the shear stress, C_τ, is the dashed line. Label 'S' refers to separation and 'R' to wake reattachment. C_n is plotted against y/t and C_τ is plotted against x/t such that the area under each curve (between S and R) is equal to each component's contribution to the overall momentum balance. (a) Circular-, (b) square- and (c) triangular-edged cylinders.

Examining Table 2.3 and Figure 2.8, it is apparent that the variation in F_n between the three cases is larger than the variation in F_τ, with the largest value of F_n (circular-edged) being about 2.2 times larger than the smallest (square-edged). In contrast, the value of F_τ for the largest value (triangular-edged) is 1.5 times larger than that for the smallest (square-edged). Thus, considering the differences in vortex strengths and frequencies indicated in Table 2.1, as well as the differences in the Reynolds shear stresses at the trailing edge shown in Figure 2.6, the overall balance is based on the complex interaction of the initial shear layer with the details of vortex formation. The force due to the normal stresses has been shown to be always in the streamwise direction for shorter bodies (Balachandar et al., 1997). However, the force due to the pressure varies significantly between the models. For the circular-edged body it is strongly against the direction of flow acting to close the recirculation region. While acting against the stream for the triangular-edged model as well, it is found that this force is relatively small for both it and the square-edged model.

The measured base pressure coefficients are presented in Table 2.3 where an unexpected result is observed. According to Roshko (1954a) a decrease in base suction should accompany a decrease in shedding frequency; however, there is a significant difference in the shedding frequencies of the circular- and triangular-edged models which does not appear in the base pressure coefficients. The base pressure for all models tested is negative, thus, the resultant pressure force indicates that the pressure near the end of the recirculation region of the square- and triangular-edged models is positive and weakly negative, respectively, while there remains strong suction near the end of the recirculation region for the circular-edged model. The near zero pressure forces for the square- and triangular-edged models reveal that it is the augmented shear stresses which act to close the mean wake as opposed to the pressure force which is often conceptualized to close this region (Roshko, 1954b). The pressure variation is examined in further detail below.

2.3.2 *Pressure and Reynolds shear stress distributions*

Contours of the Reynolds shear stresses, as well as the bounding streamlines of the recirculation region, are shown in Figure 2.9. The patterns observed herein are similar to those observed in other studies (e.g., Balachandar et al., 1997). The distribution of Reynolds shear stresses in the recirculation region shows that there is a particular region centred on $y = 0$ of zero shear stress, upstream of the wake reattachment point, surrounded by regions of alternating positive and negative stresses. It should be noted that it is this area – and not a point – that is being considered since the shear stress is zero everywhere along the wake centreline. This pattern is largely the result of vortex shedding activity over a cycle (Balachandar et al., 1997), although there are some significant variations due to the precise details of each flow, particularly the significant values of $\langle u'v' \rangle$ at the trailing edge for the square- and triangular-edged models.

The pressure minimum is known to occur along $y = 0$; at some distance from the base of the body, in the recirculation region (Roshko, 1954a). Along $y = 0$, the mean velocity and the streamwise normal stress, shown in Figure 2.10, are observed to change slowly. Figure 2.10 shows that these slow changes begin at a location upstream of the point where $\langle u'v' \rangle = 0$, through to the reattachment point; prior to this location the values change more rapidly. Thus, the streamwise gradients are negligibly small in the vicinity of the region where $\langle u'v' \rangle = 0$. Using the symmetry of the mean velocity and pressure fields across $y = 0$, the mean cross-stream velocity and the cross stream pressure gradient

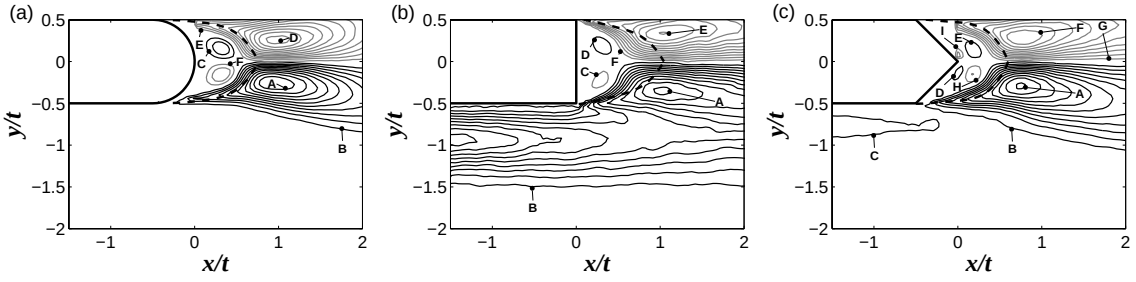

Figure 2.9. Normalized Reynolds shear stress $\langle u'v' \rangle / U_\infty$ with the bounding streamlines of the recirculation region drawn. Contour values are as follows. (a) Circular edged - Level step: 0.005, A: 0.05, B: 0.005, C: 0.005, D : -0.005, E: -0.005, F: -0.005 . (b) Square edged: Level step - 0.002, A: 0.02, B: 0.002, C: -0.002, D: 0.002, E: 0.022, F: -0.002. (c) Triangular edged - Level step: 0.004, A: 0.04, B: 0.004, C: 0.004, D: 0.004, E: 0.004, F: -0.04, G: -0.004, H: -0.004, I: -0.004.

are zero. This infers that the pressure changes only in the streamwise direction along $y = 0$. Thus, the time-averaged Navier-Stokes equation in the streamwise direction reduces to two terms along the centreline near the location of zero shear stress, such that,

$$0 = \frac{1}{\rho}\frac{d\langle p\rangle}{dx} + \frac{\partial\langle u'v'\rangle}{\partial y} \tag{2.4}$$

(Near the body, the normal stresses increase from zero to the value obtained in the recirculation region and it is observed from the PIV data that the gradient near the body is not negligible, and Eq. (2.4) does not hold).

Figure 2.11 presents the Reynolds shear stress from PIV data located on either side of $y = 0$ as well as the pressure gradient. The pressure gradient is computed from the streamwise, two-dimensional, Reynolds averaged Navier-Stokes equation of which it is the only unknown. It is shown in the figure that where the shear stresses cross zero coincides approximately with where the pressure gradient is zero which agrees with Eq. (2.4). This also implies that this region of zero shear stress coincides with the pressure minimum. Note that this is consistent with Balachandar et al.'s (1997) computational data, where one can observe that the pressure minimum occurs near the location where $\langle u'v'\rangle = 0$.

The three recirculation regions differ significantly as is shown by the distance from this point of pressure minimum to the wake reattachment point. This distance is defined as L_p and is shown in Table 2.3. In particular, L_p is substantially different for the circular-

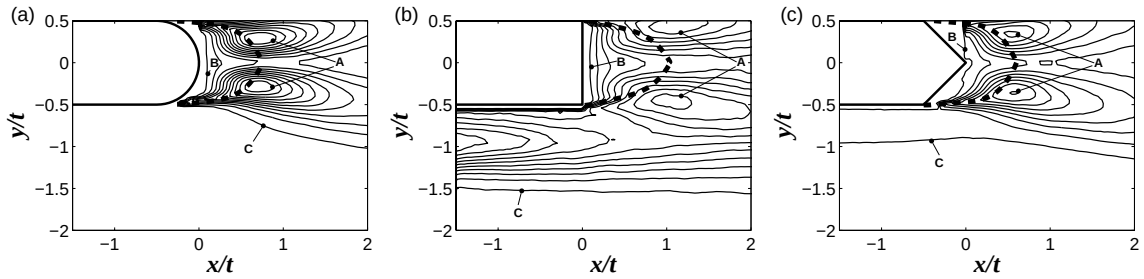

Figure 2.10. Normalized Reynolds streamwise normal stress $\langle u'u'\rangle/U_\infty$ with the bounding streamlines of the recirculation region drawn. Contour values are as follows. (a) Circular edged: Level step: 0.008, A: 0.088, B: 0.008, C: 0.008. (b) Square edged - Level step: 0.004, A: 0.04, B: 0.004, C: 0.004. (c) Triangular edged - Level step: 0.008, A: 0.072, B: 0.008, C: 0.008.

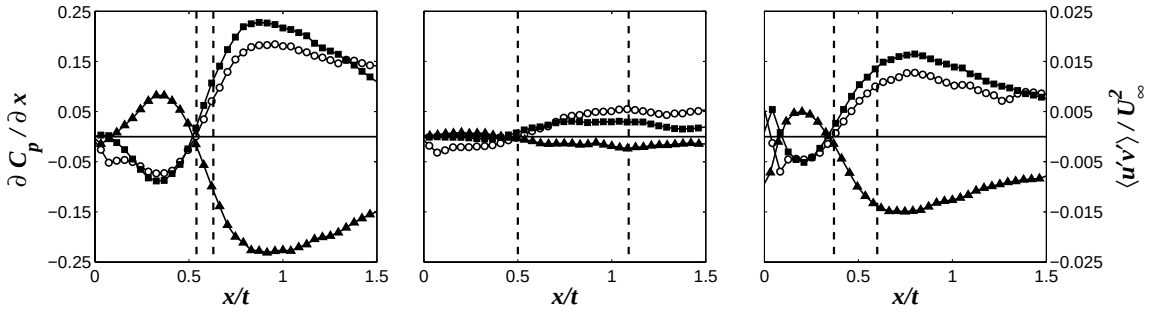

Figure 2.11. Gradient of the pressure coefficient along the wake centreline ($y = 0$) and the Reynolds shear stress close to the centreline on either side. From left to right: circular-, square- and triangular-edge models. Left axes: pressure gradient, right axes: shear stress. All corresponding axes have the same intervals as the two that are marked. Location of pressure minimum and the end of the wake recirculation region are shown as vertical lines. Symbols: o - $\partial C_p/\partial x$; ■ - $\langle u'v' \rangle / U_\infty$ above y=0, ▲ - $\langle u'v' \rangle / U_\infty$ below y=0.

edged model ($L_p = 0.09t$) compared to the square-edged model ($L_p = 0.56t$). When the recirculation region closes near the pressure minimum, the resultant pressure force is negative since the minimum pressure is negative. This result is observed for the circular- and triangular-edged models. In contrast, when the recirculation region closes farther from the pressure minimum, the pressure is increased and can become positive near the end of the recirculation region. When assessing L_p in light of the measured base pressure coefficients the role of this length is made clearer. The triangular-edged model has the same base pressure as the circular-edged cylinder; however, the role of pressure in closing the wake is much smaller than the circular-edged cylinder as is exhibited in the difference of the forces due to pressure. This difference in forces must be strongly influenced by not only the base pressures – which are similar – but the different distances, L_p.

It is also noted that this length scale exhibits similar behaviour in Balachandar et al.'s (1997) data for shorter bluff bodies (which have no reattachment on the body) where the normal flat plate, with disrupted shedding caused by lower frequency flapping of the separated shear layers, has a larger L_p than the other geometries presented in the figures of their paper, which have more regular shedding. It may be that this length, L_p, is more relevant to the vortex shedding behaviour than the wake reattachment length, $x_{r,W}$, since the latter does not vary with the shape of the bodies used in the current study. However, this length L_p still does not collapse the data to a universal scaling of the shedding

frequency indicating that the parameter space of the phenomenon is too large to be scaled by a small number of either geometric or measured values.

2.3.3 *Vortex paths and convection speed*

The measurements of the leading edge indicate the presence of leading edge vortices ranging from large, for the square-edged cylinder, to small, for the circular-edged cylinder. The trailing edge measurements suggest that the larger vortices have modified the trailing edge boundary layers, which were shown to alter the dynamics of the recirculation region in the previous section. The resultant stress distributions and pressure field of the recirculation region are also strongly influenced by the motion of the growing trailing edge vortices (Balachandar et al., 1997). Thus, it is useful to analyze the path and convection speed of these vortices.

Since an isolated vortex creates no convection speed of its own, the convection speed of a vortex is due to the surrounding velocity field. Illustrating this concept is the case of a mixing layer where vortices travel at the average convection speed of the two free stream speeds (Bernal and Roshko, 1986). Thus, the details of the boundary layer and the vortices convecting past the trailing edge into the wake recirculation region will play a critical role in determining the speed, and timing, of the vortices forming and emerging in the wake.

While it is not possible to reconstruct a shedding cycle of instantaneous vector maps from the current experimental data, the characteristics of the vortices as a function of location can be obtained using the vortex identification approach discussed in §2.1.3. Bins defined by every two PIV streamwise locations are used to sort through the sample set of vortices identified in each of the vector maps. Each bin (i.e., x location) then contains the actual distribution of both vertical location of the vortex centre and the vortex convection velocity. Figure 2.12 depicts the mean location of the vortex centres, while Figure 2.13 presents the mean vortex convection speeds. In both figures, the standard deviation in each bin is typically smaller than the marker used to represent the data.

It is not possible to separate leading edge vortices from trailing edge vortices in the

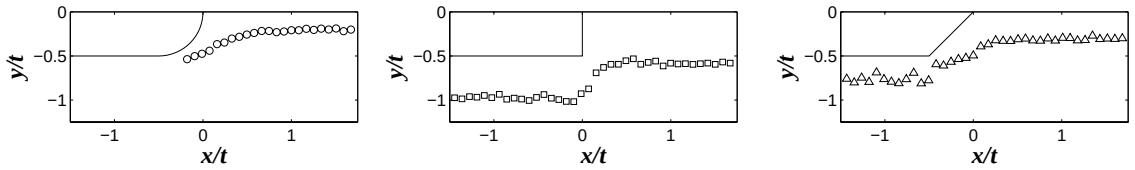

Figure 2.12. Mean y location of the vortices in each x-direction bin. (a) Circular-, (b) square- and (c) triangular-edged cylinders.

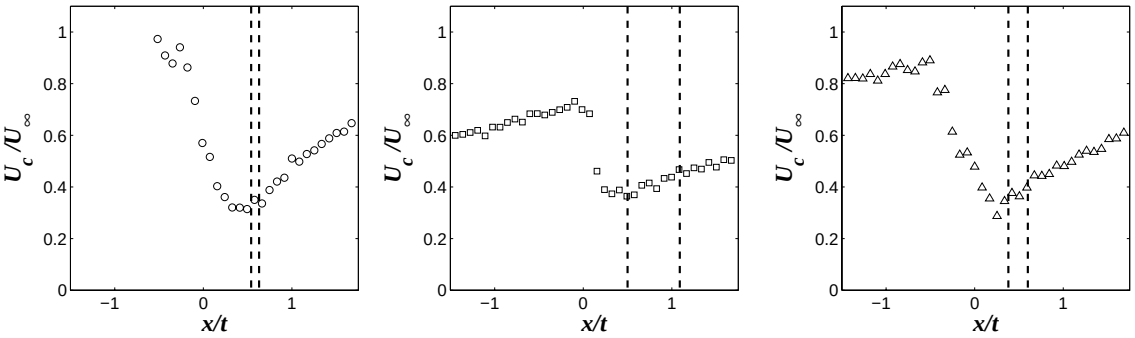

Figure 2.13. Mean streamwise convection velocity normalized by the free stream velocity of the vortices in each x-direction bin. First vertical line marks the distance L_p upstream of the second vertical line at $x_{r,W}$. (a) Circular-, (b) square- and (c) triangular-edged cylinder.

current experiments (other than the fact that it is unlikely that the trailing edge vortices travel far upstream if at all). From Figure 2.13 it appears that the leading edge vortices (i.e., those observed before the trailing edge) entering the wake have unique convection speeds which depend on the leading edge separation angle. The square-edged model has vortices entering the wake region at approximately $0.7U_\infty$ while those entering the wake of the triangular-edged cylinder are faster at approximately $0.8U_\infty$. These values are also presented in Table 2.3. The work of Cherry et al. (1984) and others has shown that vortices shed from blunt leading edges typically travel at convection speeds of approximately $0.6U_\infty$, which is also observed herein for the square-edged cylinder (until they speed up as they approach the trailing edge). For the triangular-edged model, the vortices travel along the body at about $0.8U_\infty$, and then speed up as they approach the trailing edge. It should be noted that for Tan et al.'s (2004) low Reynolds number simulations of rectangular cylinders, similar speed-up behaviour is observed.

The importance of the pressure minimum is also observed in the convection speeds of the vortices as they reach their minimum convection speed just prior to this point (which has been marked on Figure 2.13 as a dashed line). The vortices then accelerate away from

the point of the pressure minimum at markedly different rates with vortices from the circular-edged models gaining more speed in less space than the triangular-, followed by the square-edged, models. This part of the shedding cycle has been termed Phase II by Balachandar et al. (1997). By the time the vortices reach $x/t = 2$, the speeds are significantly different between the three cases, as indicated by the data in Table 2.1.

2.4 Conclusions

Although different sizes of the rectangular cylinder have been studied in the literature, there is minimal information about changing the leading and trailing edges for a given elongation ratio as has been done herein. From the experiments performed herein several conclusions can be made.

At the leading edge it was discovered that, as with pressures, mean velocities collapse well in the separation bubble when the reattachment length is used to scale the data. However, the Reynolds shear stresses are higher for larger separation angles when the same scaling is used. These differences in shear stress are manifest at the trailing edge where there are distinctions in both the shear stress and velocity profiles. The differences between the trailing edge flows of each model lead to distinct recirculation regions.

The recirculation region of each model is unique as was shown by a force balance of the mean recirculation bubble. The location of the pressure minimum was found to coincide with a region of zero Reynolds shear stress on the wake centreline and a length was defined from this location to the end of the recirculation region. This length, L_p, varied between all three models. Vortices entering the recirculation region were shown to take distinct paths and to accelerate and decelerate at different rates across all models. The pressure minimum was observed to occur where the convection speed of vortices in the recirculation region was a minimum.

All of these observations begin to explain the widely varying wakes observed across the models. The shedding frequency trends from shorter bluff bodies regarding base pressure and length of recirculation region are shown not to hold for the bodies tested herein. Also, at the same point in the wake, the characteristics of an ensemble averaged vortex

are markedly different. The triangular-edged model had much stronger vortices than the circular-edged model even though the vortices were smaller in size. The square-edged model had vortices convecting much slower than the other two models and the shedding was shown to be intermittent and weak compared to the other two models.

Chapter 3

Effects of leading edge geometry on vortex shedding of elongated bluff bodies

In the previous chapter, the flow around three elongated bluff bodies was examined. The leading edge separation bubble was quantified as was the trailing edge boundary layer for each body. The vortices shed in the wake were also characterized based on an ensemble average; however, emphasis was placed on the dynamics of the recirculation region. It was found that due to the significant leading edge separating-reattaching flow that the pressure created by the growing trailing edge vortex became increasingly less important in closing the recirculation region.

The current study seeks to examine the interaction of these two types of flows: the leading edge separation and reattachment and the trailing edge vortex shedding, which occur simultaneously for elongated bluff bodies. Specifically it is of interest how the leading edge geometry affects this interaction. As was discussed in the Introduction to Part I, the leading edge geometry is suggested to play a more significant role than the geometry of the trailing edge. Pressure data are measured herein at a significant scale such that the leading edge separating-reattaching flow and the trailing edge vortex shedding can both be well quantified. These two flow scenarios are then examined in light of their magnitude, timing, and three-dimensionality. Through these data, a mechanism is suggested regarding how the leading edge separating-reattaching flow interacts with the trailing edge vortex shedding and how this interaction affects various parameters including aerodynamic loading and shedding frequency at Reynolds numbers of order $O(10^4)$. In this chapter, the pressure data are taken on the body with 6 different leading edge configurations. The details of the experimental setup can be found in §1.2.

3.1 Results

3.1.1 *Aerodynamic loading and Reynolds number dependence*

In this section, the conventional parameters related to vortex shedding bodies are presented. The effect of Reynolds numbers is also examined in this section. The

Reynolds number dependence will be shown by plotting the aerodynamic loading characteristics at all 8 Reynolds numbers for which data were taken. A short discussion on its effect will summarize the results at the end of this subsection.

The pressure data in each streamwise ring are integrated along the surface to obtain sectional load coefficients. The time-averaged sectional drag coefficient, C_D, is shown in Figure 3.1a for the centre streamwise ring. The data of the other streamwise rings match that of the centre ring in the time-averaged sense and are thus not shown. The sectional drag force is shown to increase monotonically with increasing leading edge separation angle, γ, as one would expect since the bodies are becoming increasingly bluff. The separation angle is 0° for the model with an elliptical leading edge and assumed to be tangent to half of the interior angle of each triangular nosing. All of the models are symmetric so the mean lift is negligible; however, the lift fluctuations are not and are shown in Figure 3.1b. The lift fluctuations are computed as the standard deviation of the integrated sectional lift force. There is a noticeable peak in the variation of the lift fluctuations at a separation angle of 30°. Along with the drag and fluctuating lift, the base pressure is often reported as a means of quantifying the strength of the vortex shedding (e.g., Roshko, 1954a). The time-averaged pressure coefficient located at the centre of the trailing edge in both the vertical and spanwise directions is plotted in Figure 3.2. Also plotted in Figure 3.2 are the standard deviations about the base pressure plotted

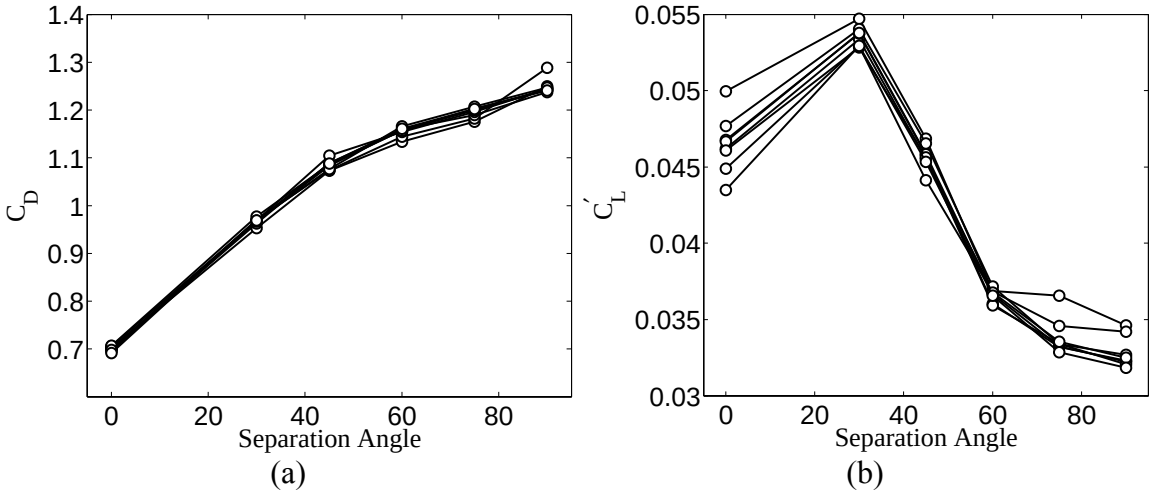

Figure 3.1. (a) Sectional drag coefficient and (b) sectional lift coefficient fluctuation variation with separation angle at all Reynolds numbers tested. Lines are for ease of visualization only.

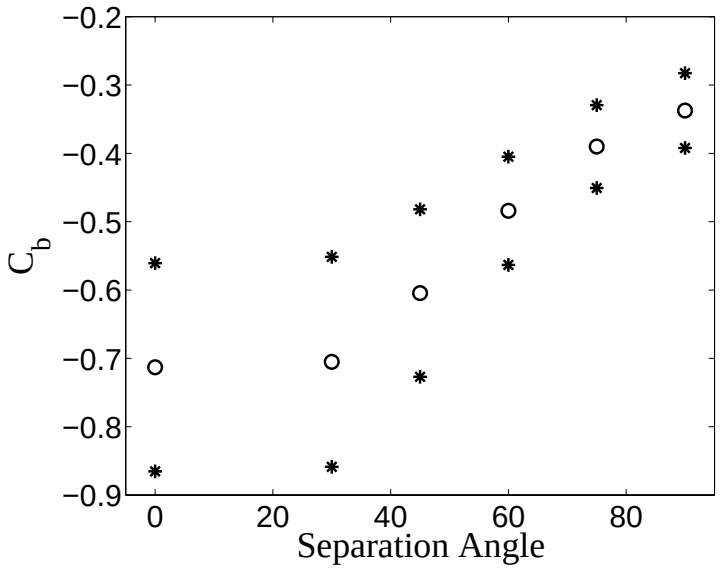

Figure 3.2. Base pressure variation with increasing separation angle. ○ – mean base pressure, * – standard deviation of the base pressure (measured off of the corresponding mean value).

with asterisks by their corresponding magnitudes off of the mean. It is observed that even though the lift fluctuations were higher for the case with a separation angle of 30°, the base pressure does not show a pronounced peak at this separation angle.

The preceding characterizes the magnitude of the loading on the body; however, the shedding frequency has classically been of greater interest and its variation is reported here in Figure 3.3 for all Reynolds number experiments. The shedding frequency is estimated by computing the spectra of the integrated lift coefficient for each model and normalizing it as the Strouhal number, $St=ft/U_\infty$. It is observed that the decrease of the Strouhal number is nearly linear. Although no direct evidence for this trend is found, a discussion on the possible mechanism behind this linearity is presented in §3.2.3.

From the presented results in this section, the Reynolds number is shown to play a relatively minor role especially in the drag coefficient. The Strouhal number was also observed to be relatively unchanged over the Reynolds numbers tested, $Re = 4x10^4 – 7.5x10^4$. Underscoring this point, across the various noses the change in Strouhal number ranges between 3-6%. The most significant changes are observed in the lift fluctuations (Figure 3.1b) where the greatest variation occurs for the model with an elliptical leading edge which is expected to be more dependent on Reynolds numbers, as opposed to the

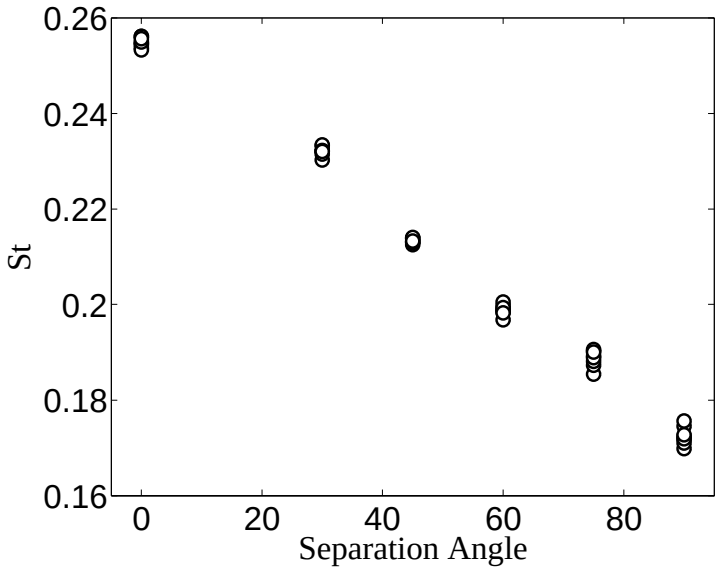

Figure 3.3. Strouhal number, $St = ft/U_\infty$ variation with the separation angle at all Reynolds numbers tested.

bodies with fixed separation points. The results in the present work will focus on the case when Re = $5x10^4$ from this point onwards. It is for this Reynolds number that the base pressure has already been reported.

3.1.2 *Leading edge separation bubble*

The leading edge separation and reattachment is one of the defining features of elongated bluff body flows. In the current study, the elliptical nose is used as a comparison with bodies without leading edge separation and reattachment. The determination of flow reattachment can be performed many different ways. For example, reversed flow intermittency (e.g. Kiya and Sasaki, 1983; Djilali and Gartshore, 1991), flow visualization (Ram and Arakeri, 1990), mean flow velocity profiles (Chapter 2) and surface oil visualization (e.g., Cherry et al., 1984). From the results presented in Cherry et al. (1984), it is observed that flow reattachment occurs just downstream of the location where the pressure fluctuations are a maximum. Herein, it is assumed that the reattachment point is related to the location of maximum pressure fluctuation by $x_r = x|_{max(Cp')}/0.95$. It is well known that the time-averaged pressure field within a separation bubble collapses well when scaled by the reattachment length (e.g., Roshko and Lau, 1965; Djilali and Gartshore, 1991; Ram and Arakeri, 1990). However, Ram and Arakeri

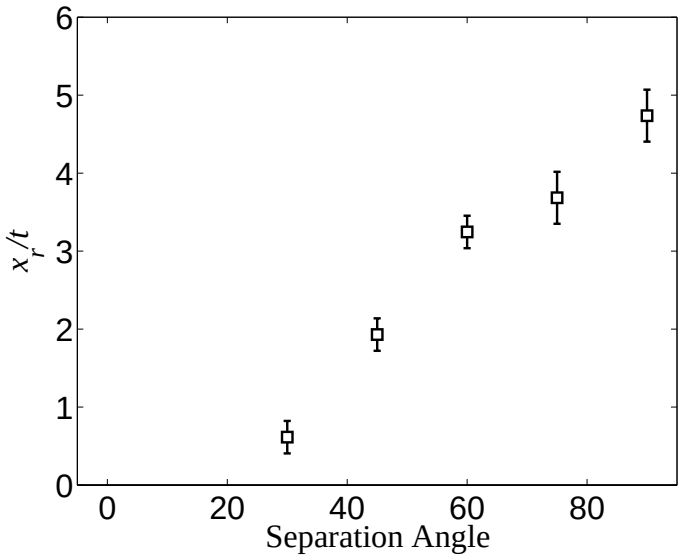

Figure 3.4. Variation of the reattachment length with separation angle. Error bars mark the uncertainty in the estimate of the reattachment length.

(1990) show that the pressure fluctuations can be partially scaled by the reattachment length. The scaling is only partial because the magnitudes of the fluctuations do not collapse on each other; however, the locations of the peak fluctuations are all observed at the same location when scaled by the reattachment length – a feature that is exploited currently to estimate the reattachment length. The reattachment lengths estimated in this way are shown in Figure 3.4. Error bars are shown in Figure 3.4 to mark the uncertainty caused by the resolution of the pressure taps. Many researchers (Cherry et al., 1984; Castro and Epik, 1998) have shown that wind tunnel blockage has a significant effect on the reattachment length. The current blockage is 4.1%, for which no corrections have been made, and the reattachment lengths reported herein are in good agreement with existing literature at comparable blockage ratios (e.g., Djilali and Gartshore, 1991; Cherry et al., 1984).

As previously discussed, Roshko and Lau (1965) showed that following a suitable normalization of the pressure coefficient that the time-averaged pressure within a separation bubble can be collapsed when scaled by the reattachment length. This collapse has been validated by several researchers using various leading edge geometries (Yeung and Parkinson, 2004 have compiled some of these studies). The pressure data are normalized along the surface in the same way here using,

$$C_p^* = \frac{C_p - \min(C_p)}{1 - \min(C_p)} \tag{3.1}$$

It is observed from Figure 3.5 that when the reduction of Eq. (3.1) is plotted against the streamwise distance (normalized by the reattachment length) that the data collapses well in the present case until close to the mean reattachment length. It should be noted that the vast majority of the previously published data are from bodies which can be considered effectively infinite in streamwise extent. Thus, it was not a foregone conclusion that the data in the present case should follow the same scaling because of the potential influence of the wake flow.

Even though the data scales relatively well by the Roshko and Lau (1965) scaling, there are other aspects of the leading edge separation bubble which clearly distinguish one model from the next. One method of describing separating-reattaching flows is to explore the vorticity generation mechanisms, such as those suggested by Reynolds and Carr (1985). They showed that by making assumptions similar to the classical boundary layer assumptions that the generation of circulation is related to the pressure field at the surface. The first assumption is that the change in the streamwise direction of velocity

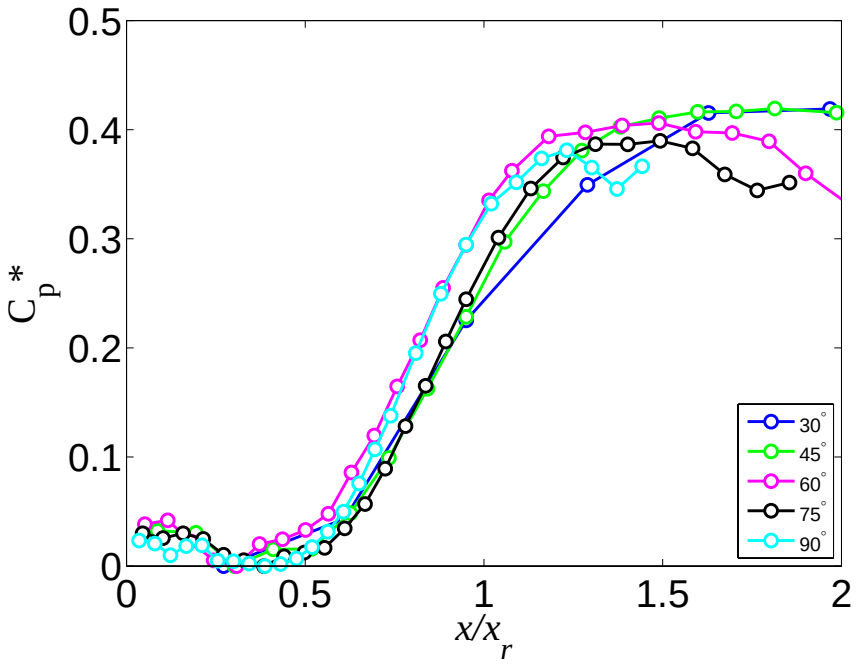

Figure 3.5. Scaled pressure coefficients along the surface of each model with leading edge separation. Values in the legend refer to the separation angles of each model.

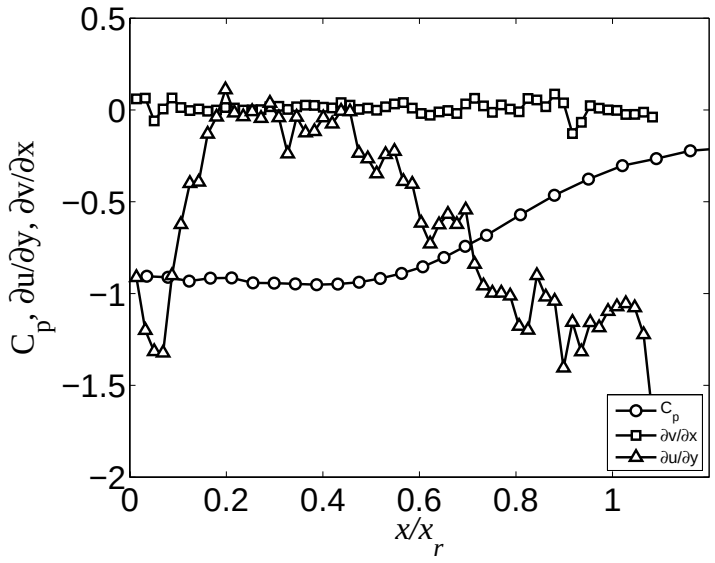

Figure 3.6. Variation of the vorticity gradients and the pressure coefficient until reattachment for the rectangular cylinder (separation angle = 90°). Velocity gradients are taken approximately 0.2*t* above the surface.

near the wall is slow such that vorticity can largely be described by, $\omega_z \approx -\partial u/\partial y$. The validity of this assumption is shown by the negligible contribution of $\partial v/\partial x$ from the PIV measurements taken at 0.2*t* underneath the model surface, within the separation bubble, plotted in Figure 3.6. This assumption allows for the following form of the two-dimensional momentum equation at the wall (e.g., Lighthill, 1963),

$$\frac{1}{\rho}\frac{dp}{dx} = -\nu\frac{\partial \omega_z}{\partial y} \tag{3.2}$$

The time rate of change of circulation (where time is denoted by τ to avoid confusion with the thickness *t*) within the control surface can be written as the volume integral of the viscous diffusion of vorticity or, equivalently, the surface integral of the vorticity flux (e.g., Andreopoulus and Agui, 1996),

$$\frac{d\Gamma}{d\tau} = \iiint \nu\nabla^2\vec{\omega}dV = -\iint \nu\left(\vec{n}\cdot\nabla\vec{\omega}\right)dS \tag{3.3}$$

A control surface is drawn herein which extends from the surface to the free stream between two arbitrary streamwise locations. The spanwise extent of the control surface is limited herein (i.e., $dz = 1$) such that the circulation can be thought of as analogous to a sectional force coefficient. It should be noted that the flow across the span of the model

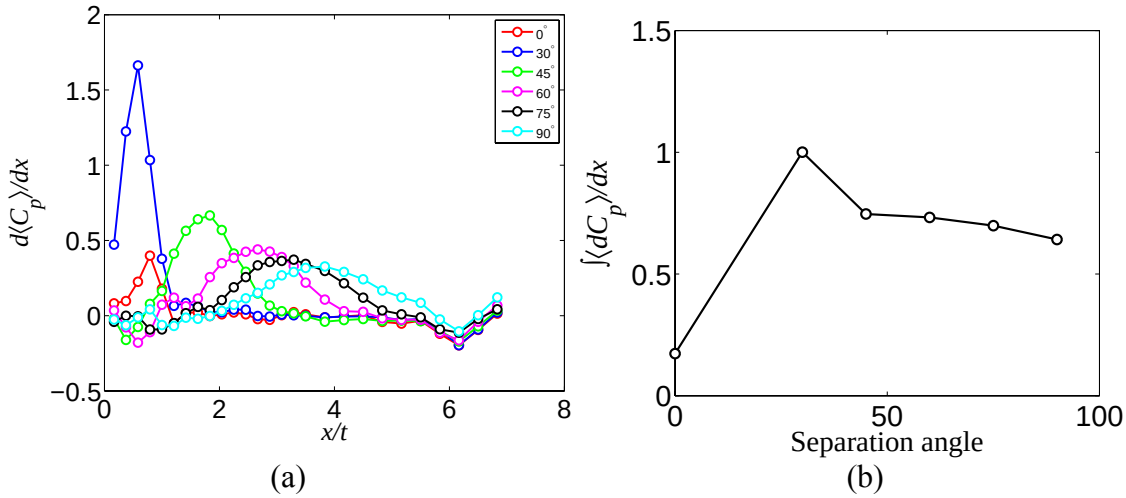

Figure 3.7. (a) Streamwise gradient of the pressure coefficient measured at each tap. Legend refers to the leading edge separation angle. (b) Integrated pressure gradient along the leading edge separation bubble. Lines are for visualization purposes only and angle brackets denote a time average.

becomes uniform in the time average implying that the time-averaged sectional circulation (and force coefficients) apply over the span of the model. It is also assumed that the vorticity vector is aligned primarily with the spanwise direction. The control surface has four main segments. Of these four segments, it is convenient to discuss the two separate mechanisms which generate vorticity: that generated by the surface and that generated by vorticity flux at the streamwise boundaries. The potential flow in the free stream contributes nothing to the surface integral in Eq. (3.3) as the vorticity flux across the boundary at this location is, by definition, zero. If the control surface extends from the separation point at the leading edge until shortly after reattachment, the vorticity generation is largely that due to the surface. The time rate of change of circulation can then be approximated by,

$$\frac{d\Gamma}{d\tau}(\tau) \approx \int_{x_1}^{x_2} \frac{dC_p(x,\tau)}{dx} dx \tag{3.4}$$

by substituting Eq. (3.2) into Eq. (3.3). The time-averaged pressure gradient is computed for each body and is plotted in Figure 3.7a with the integrated pressure gradient for each body in Figure 3.7b. It is observed that the time-averaged rate of circulation is greatest for a separation angle of 30°, which agrees with the observed peak in the lift fluctuations shown in Figure 3.1b. Changes to the circulation rate are discussed further in §3.2.3.

Aside from the magnitude and size (as approximated by the reattachment length) of the leading edge structures, the convection speed of shed structures is also of interest. Cherry et al. (1984) reported a convection speed of approximately $0.6U_\infty$ for vortices shed from the leading edge separation bubble of an infinite plate. Speeds of the same approximate value have been validated by many subsequent studies of similar type. Herein, the change in leading edge geometry warrants further investigation into the convection speed of leading edge vortices. The cross-correlation coefficient with time lag, T, and spacing Δx,

$$R(\Delta x, \mathrm{T}) = \frac{\langle p'_1(x_0, \tau) p'_2(x_0 + \Delta x, \tau + \mathrm{T}) \rangle}{\sigma_{p_1} \sigma_{p_2}} \tag{3.5}$$

where the prime denotes a fluctuation from the mean and the angle brackets represent a time average, is shown for each body in Figure 3.8 where x_0 is located just prior to mean reattachment for each body. An observable ridge of high correlation is observed for each body in Figure 3.8. The approximately linear shape of the ridge allows for the estimation

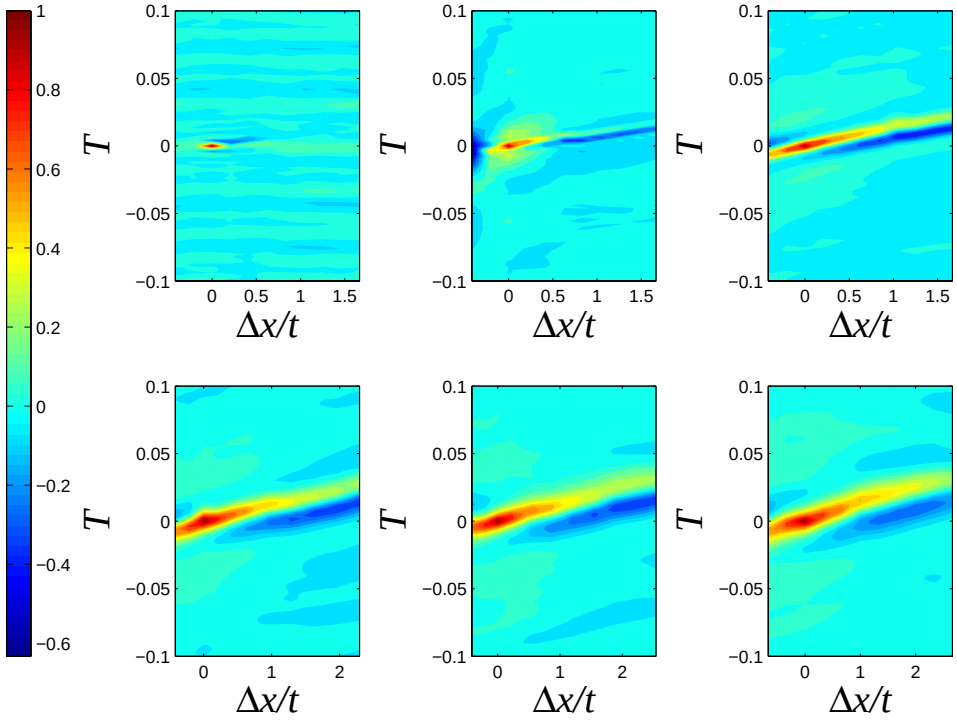

Figure 3.8. Contours are the normalized cross-correlation coefficient at different time lags, T, between pressure taps with different spacing, Δx, originating just upstream of the mean reattachment point. From top left to bottom right: 0°, 30°, 45°, 60°, 75°, 90°. Colour map applies to all figures.

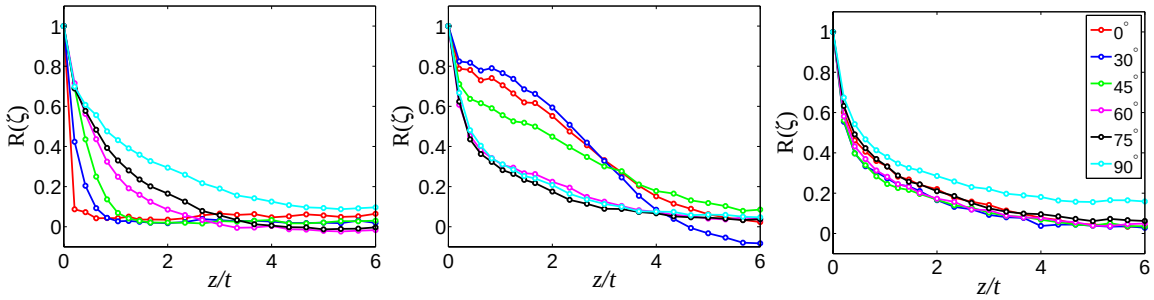

(a) (b) (c)

Figure 3.9. Spanwise correlation across top surface at (a) $x = t$, (b) $x = 6.17t$ and (c) in the base region at $y = 0$. Symbols for all three figures are shown by the legend in (c).

of a convection speed by taking its slope which herein is found to be approximately $0.65U_\infty$ for all bodies with leading edge separation bubbles. Thus, the geometry does not seem to affect the initial convection speed of the vortices leaving the leading edge separation bubble. The breadth of the ridge in Figure 3.8 reveals the scaling of the structures with the larger reattachment lengths observed to shed larger structures, as expected.

3.1.3 *Spanwise characteristics*

As shown in Figure 1.2, the models are equipped with 5 different locations of spanwise rows. Because these rows are at fixed locations, the spanwise characteristics measured at the leading edge (at $x = 1t$) are at different locations in relation to the mean reattachment length of each body. While this is also the case at the trailing edge, where the spanwise row is located at $x = 6.17t$, the spanwise characteristics at this location offer details about the flow approaching the recirculation region. A spanwise row is also located in the base region at $y = 0$.

A time-averaged evaluation of the spanwise characteristics is shown in Figure 3.9 for three spanwise row locations: leading, trailing and base, where the leading and trailing rows were taken on the top of the model. Due to the symmetry of the results, the data from the bottom are not shown. The correlation coefficient shown in Figure 3.9 is calculated, in relation to the central tap, as follows,

$$R(\zeta) = \frac{\langle p'_1(z_0) p'_2(z_0 + \zeta) \rangle}{\sigma_{p_1} \sigma_{p_2}} \tag{3.6}$$

where z_0 is the spanwise location of the central tap, ζ is the spatial lag and σ_p is the standard deviation. Close to the leading edge, it is observed that the flow is better correlated for bodies with larger separation angles. This situation is reversed near the trailing edge as the bodies with smaller separation angles have well correlated flow approaching the base region. Within the base region, the flow is poorly correlated for all models as the three-dimensionality of this stagnation region is high.

An examination of the three-dimensionality in both time and space is now performed. A time-lag autocorrelation is performed for each spanwise tap using the following, where T is the time lag,

$$R(z,\mathrm{T}) = \frac{\langle p'(z,\tau)p'(z,\tau+\mathrm{T})\rangle}{\sigma_p^{\,2}} \tag{3.7}$$

The value of the correlation coefficient is plotted as contours in the span-time plane in Figure 3.10 for the row close to the trailing edge ($x = 6.17t$). The flow is correlated poorly in time for all models both close to the leading edge and in the base region and are therefore not shown herein. However, from Figure 3.10 it is evident that there is strong periodic correlation of the flow near the trailing edge. Both the strength and the frequency of the wavelengths, observed in time, correspond to the strength and frequency

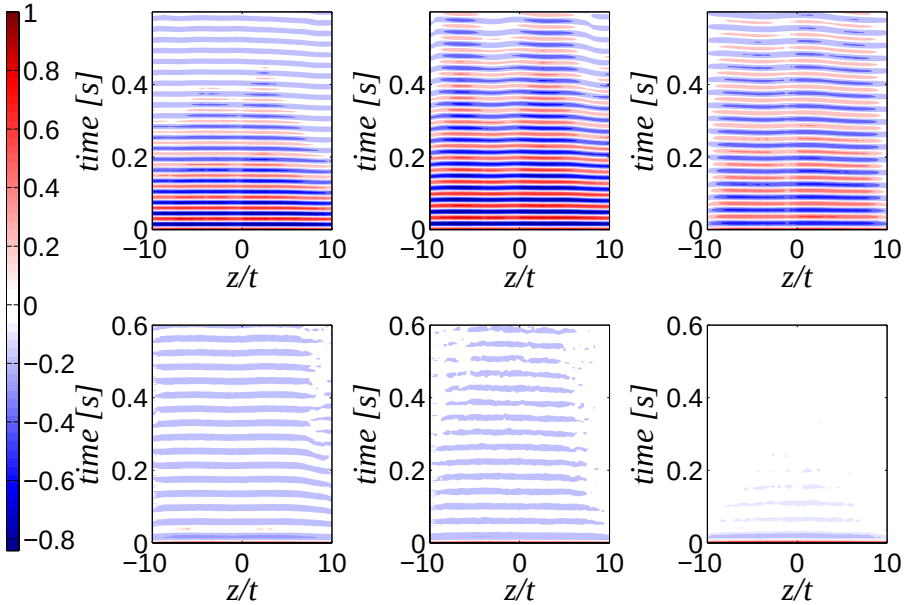

Figure 3.10.Contours of the autocorrelation coefficient computed at each tap in the spanwise row near the trailing edge, $x = 6.17t$. From top left to bottom right: 0°, 30°, 45°, 60°, 75°, 90°. Colour map applies to all figures.

of the vortex shedding. There is also an apparent spanwise pattern for the three smallest separation angles. This observation is returned to when the flow at this location is examined in greater detail in the following section.

3.1.4 *Base region*

Although the base pressure is previously reported in §3.1.1, a more thorough examination of the base region is given here. As previously discussed, there is a spanwise row of taps on the trailing edge of the model in this region and three vertical tap arrangements consisting of five taps each. The focus in this section is primarily on the vertical tap arrangement at the spanwise centre of the model. The distribution of the time averaged pressure, $\langle C_p \rangle$, along the trailing edge surface is shown in Figure 3.11a while the standard deviation of the pressure, C_p', is shown in Figure 3.11b. The base pressure reported earlier is the time averaged quantity at $y = 0$. The mean pressure distribution is observed to be relatively flat for all models; however, differences are observed in the fluctuating pressures. Just as was the case for the fluctuating lift force, the model with a separation angle of 30° is also observed to have higher pressure fluctuations in the base region. Another observation of the fluctuating pressure data is the difference in slopes away from the minimum at $y = 0$ – a point returned to in detail in §3.2.3. Many authors (e.g., Roshko, 1954a) have linked the pressure in the base region with the strength of vortex formation. Herein, it is suggested that the magnitude and the slope of the pressure fluctuation distribution in the base region is also indicative of the vortex formation process.

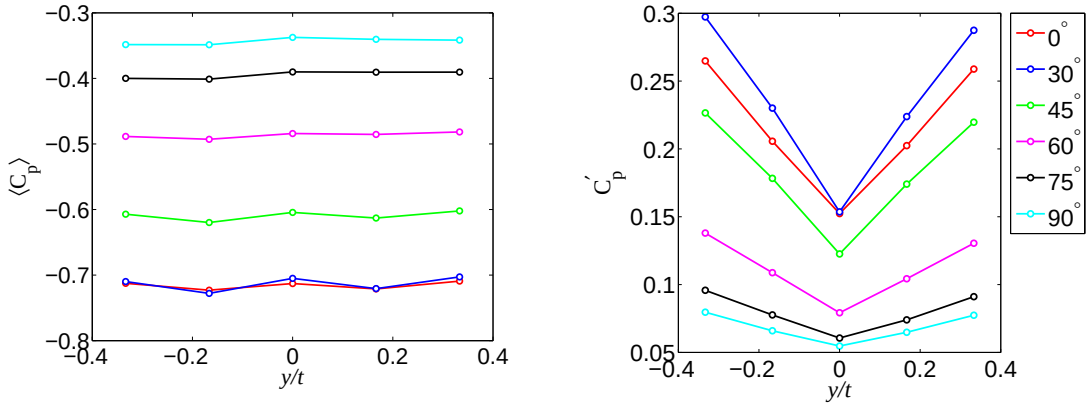

Figure 3.11. Data from the vertical tap arrangement in the base region at $z = 0$. (a) Time average and (b) standard deviation of the pressure coefficient for each model (refer to legend).

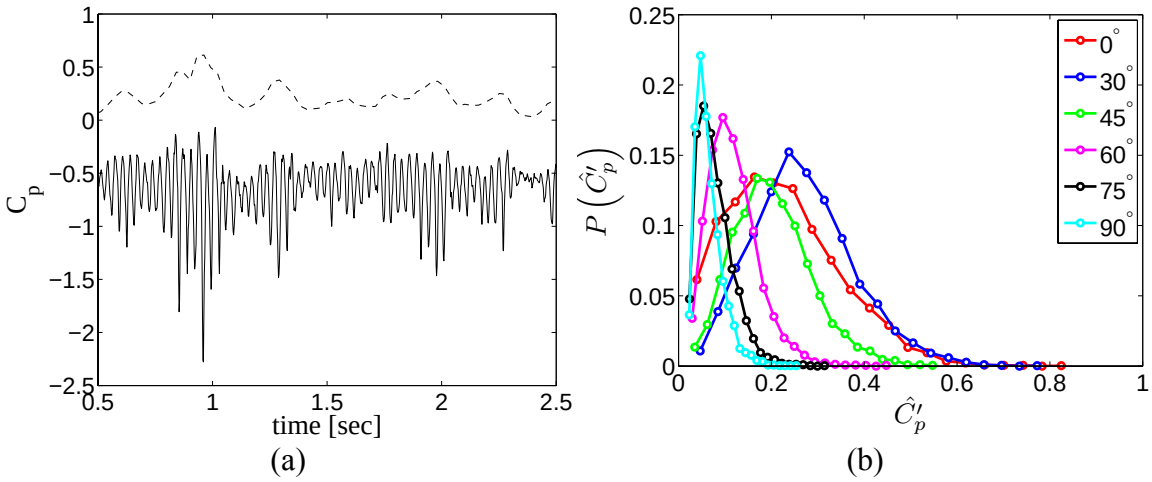

Figure 3.12. (a) Time trace of the pressure tap at $(x,y,z) = (7t, 0.33t, 0)$ for the body with a separation angle of 30°. Dashed line is a window averaged standard deviation of the time series. (b) Distribution of the window averaged standard deviation for all models (as marked in the legend).

The results presented thus far represent time averages of the entire 120 sec. record length. However, these data gloss over many of the temporal details of the shedding processes occurring for these bodies. In Figure 3.12a, a sample is plotted of the time series for the case where the leading edge separation angle is 30°. The pressure coefficient data are presented for the tap located at $y = 0.33t$ in the base region. Therein it is possible to observe events where the fluctuations of the pressure are quite strong and other times when the strength of the fluctuations is diminished. The dashed line in Figure 3.12a represents a window averaged standard deviation, $\hat{C}'_p$, with a window size of 30 points and a 50% overlap used to quantify the magnitude of the fluctuations with time. The distribution of $\hat{C}'_p$ is shown in Figure 3.12b. The area under each distribution returns the corresponding value of the total time averaged standard deviation. The analysis of the time series and the corresponding distributions reveals that there is an "intermittency" or "bursting" to the shedding events. The work of Wu et al. (2005) shows a similar phenomenon in the wake of a circular cylinder and the term "burst" will be used hereafter to describe events of strong fluctuating suctions which represent the tail of the distributions shown in Figure 3.12b. Quantitatively, the bursting events are defined as having a window averaged standard deviation greater than the mode plus 1.75 times the standard deviation of the distribution shown in Figure 3.12b. For each model, the longest

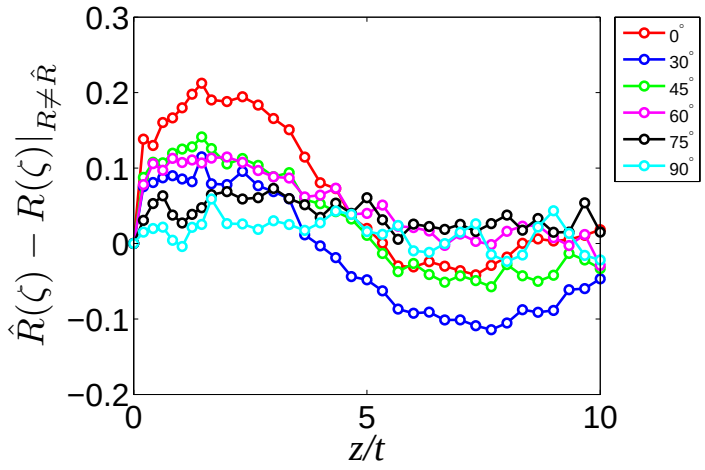

Figure 3.13. Difference in spanwise correlation between bursting events (marked with ˆ) and non-bursting events for all bodies marked according to the legend.

time sequence spent above this threshold is also identified and typically consisted of approximately 100 time steps. The range of the distribution (Figure 3.12b) of these burst events is shown to vary significantly from model to model. It is anticipated from the work of Wu et al. (2005) that the bursting behaviour of each body is linked to varying three-dimensional effects.

The data are now examined in light of changes to the surface pressure field during the bursting events. First, the characteristics across the span of the model are examined. The correlation along the span of the model, defined in Eq. (3.6), is computed for all bursting events as well as the data which fall below this threshold. The difference between the correlations at the trailing edge is shown in Figure 3.13. Among the trends observed in Figure 3.13, it should be noted that the positive correlations become more positive and negative correlations more negative during bursting events. Thus, it is observed that the spanwise correlation at the trailing edge is increased during bursting events for models with small leading edge separation angles with negligible increases as the leading edge separation angle is increased. The same calculation is performed for the spanwise rows at the leading edge and within the base region; however, no noteworthy changes were observed at these locations.

As previously discussed, a bursting sequence is identified for each model. In Figure 3.14, the pressure data are plotted to corresponding colour values along the span of the model

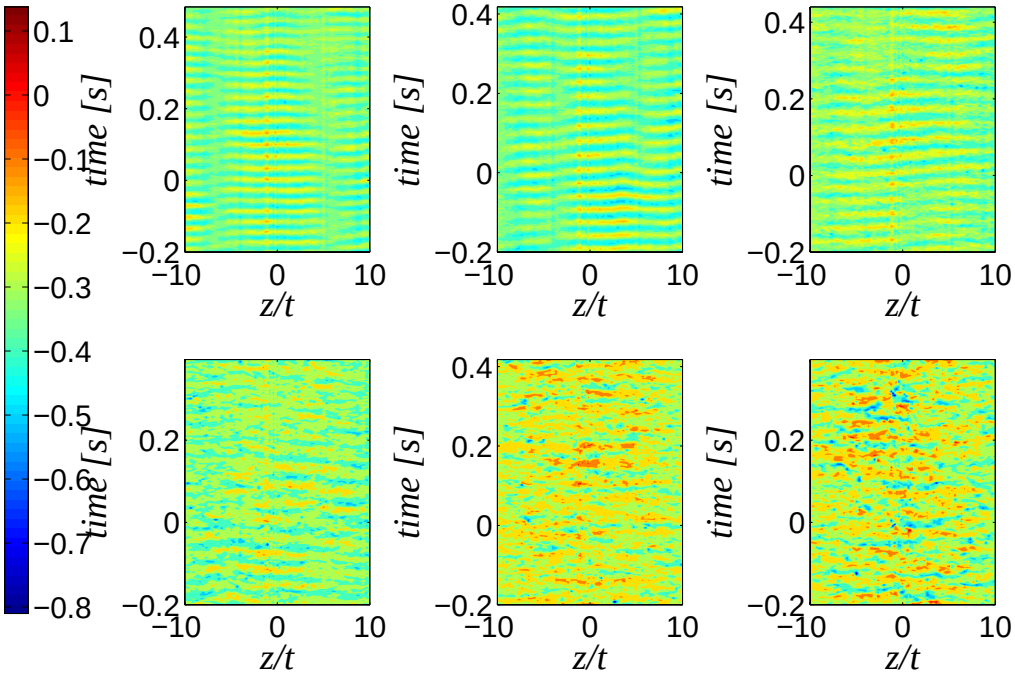

Figure 3.14. Contours of the instantaneous pressure coefficient along the span of each body in time. From top left to bottom right: 0°, 30°, 45°, 60°, 75°, 90°. Colour map applies to all figures.

near the trailing edge at each time step of the bursting sequence for each model. Context is also given to the bursting sequence by plotting the same number of time steps contained within the sequence both before and after the bursting sequence. In this way, it is possible to observe any precursors to the sequence as well as any indications regarding why the bursting sequence was terminated. In Figure 3.14, time $\tau = 0$ represents the start of the identified bursting sequence. A strong periodicity is observed for the models with smaller separation angles with essentially no periodicity observed for the models with separation angles of 75° and 90°. There are also strong indications of the three-dimensionality of the flow over this location, which agree with the spanwise correlations shown in Figure 3.10. These dislocations in the spanwise direction seem to have a recurring wavelength; however, without flow data it is not possible at this point to speculate as to their cause. These patterns of discontinuities in the spanwise contours are most prevalent for models with leading edge separation angles of 0°, 30° and 45°. In these cases, it is observed that data are both stronger in magnitude and better correlated before the bursting events ($\tau < 0$) than after the bursting events indicating that increased

correlation along the span may be a precursor to bursting events as well as being a trait observed during bursting events.

The time averaged rate of circulation generation for the leading edge separation bubble was shown in Figure 3.7b. During bursting events, neither the time averaged rate of circulation nor the fluctuations change appreciably. Thus, the strong bursting events at the trailing edge do not seem to impact the leading edge flow significantly.

3.1.5 *Leading edge separation and trailing edge vortex shedding interaction*

The first examination of the interaction between leading and trailing edge flows is an analysis of the synchronization between these two locations. An estimate of the magnitude-squared coherence spectrum is computed using a minimum variance distortionless response approach (Benesty et al., 2005). The coherence spectra are computed for each body and between two separate locations. Figure 3.15a shows the coherence spectra between the tap at $y = 0.33t$ in the base region and the first tap on the surface of the model in the streamwise direction, $x = 0.17t$. Figure 3.15b shows the coherence between the tap at $y = 0.33t$ in the base region and a tap just upstream of the mean reattachment point. It is observed that there are peaks at the shedding frequencies of each body for the tap located at $x = 0.17t$; however, by the time the separated shear

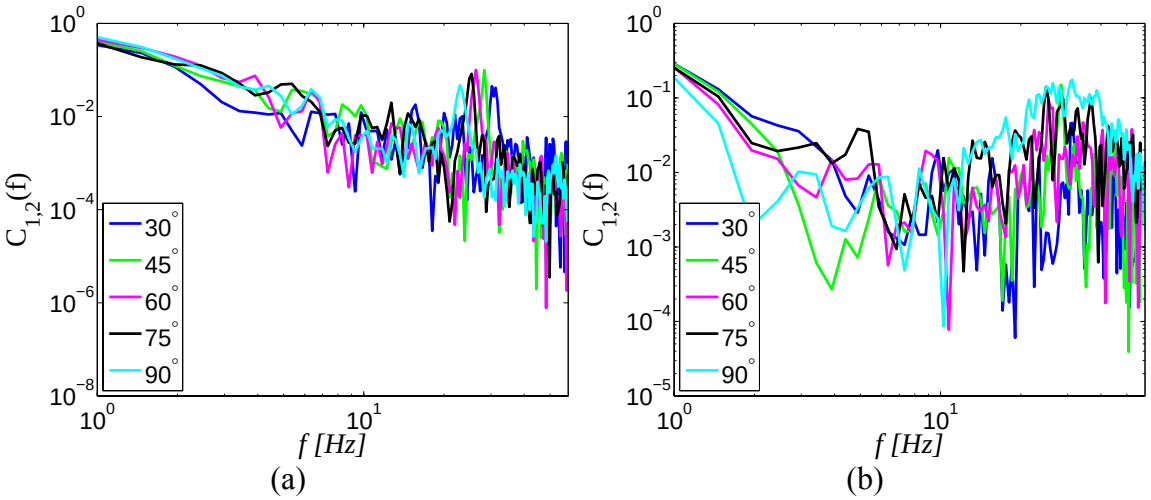

Figure 3.15. Magnitude squared coherence spectra for each body between the tap at $y = 0.33t$ in the base region and (a) $x = 0.17t$ on the top surface, (b) tap located just upstream of the mean reattachment point.

layer reattaches there is no longer a strong influence of the trailing edge shedding frequency. There remains a noticeable level of energy associated around the shedding frequency, but no defined peaks.

The results of Cherry et al. (1984) have shown that without the presence of a trailing edge, the separation bubble does not shed vortices regularly. The ILEV instability at lower Reynolds numbers completes a feedback between leading edge vortices passing the trailing edge with the shedding of vortices at the leading edge such that a strong periodicity emerges (Naudascher and Wang, 1993). The leading edge separation bubble is now examined in terms of its frequency content in Figure 3.16 where it is observed that there is a noticeable energy content at a low frequency near the reattachment point for each model with leading edge separation. This low frequency flapping of shear layers is a well known feature of separating-reattaching flows (e.g., Castro and Haque, 1987). Closer to the wake (not shown) the energy content begins to concentrate around the shedding frequency which is approximately two orders-of-magnitude more energetic than the peaks at the low frequency flapping of the shear layer. Thus, the leading edge

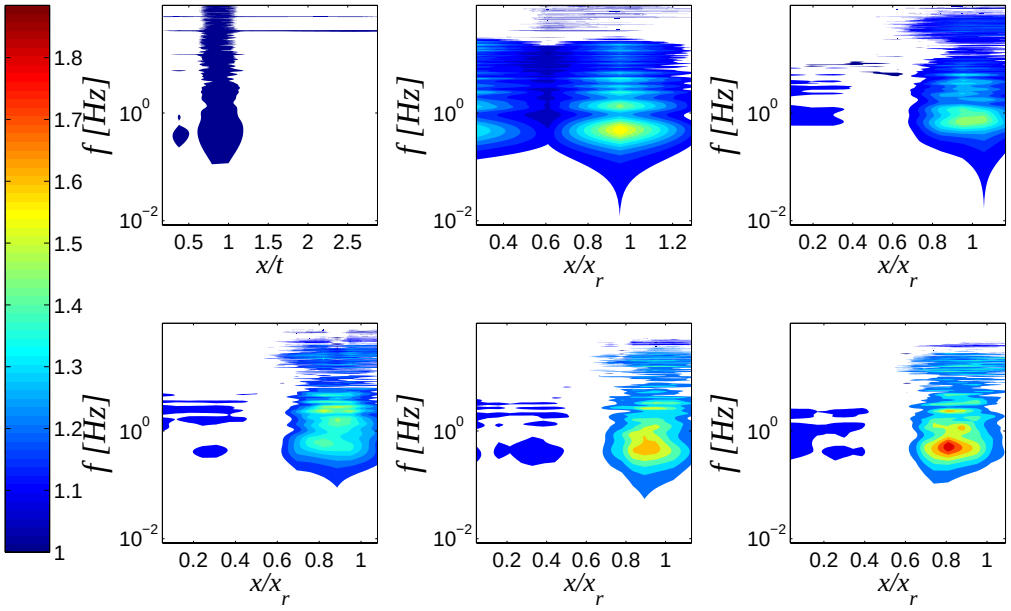

Figure 3.16. Contours of $10^{S(f)}$, where S(f) is the estimate of the power spectral density at each tap position, *x*. From top left to bottom right: 0°, 30°, 45°, 60°, 75°, 90°. Colour map applies to all figures.

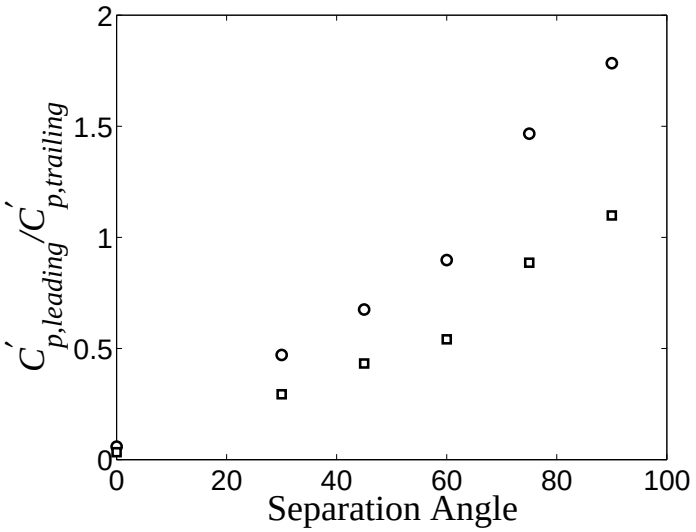

Figure 3.17. Ratio between the fluctuations of the pressure tap near mean reattachment and the fluctuations of the pressure tap at $y = 0.33t$ in the base region. ○ - time-averaged, □ - burst events

separation bubble does not appear to shed vortices regularly and the ILEV instability is indeed suppressed.

Thus far, the timing of the leading edge separation bubble and possible timing between leading and trailing edge flows has been examined. However, now the focus is shifted towards the comparative magnitudes of fluctuations at the leading and trailing edge. The ratio between fluctuating pressures near mean reattachment on the surface and the fluctuating pressure at $y = 0.33t$ in the base region is computed for each body and shown in Figure 3.17. Also shown in Figure 3.17 is the same ratio during bursting events. It is observed that the ratio is near zero for the elliptical leading edge and surpasses unity on its monotonic increase to its maximum for the body with a leading edge separation angle of 90°. Herein, a ratio of unity is used to discuss bodies which are leading edge dominated ($C'_{p,leading}/C'_{p,trailing} > 1$) and trailing edge dominated ($C'_{p,leading}/C'_{p,trailing} < 1$). The ratios are all observed to decrease during bursting events; however, it should be noted that the drop is solely due to the increase in trailing edge fluctuations during bursting events. A result which agrees with the assessment that circulation rate at the leading edge does not change during bursting events.

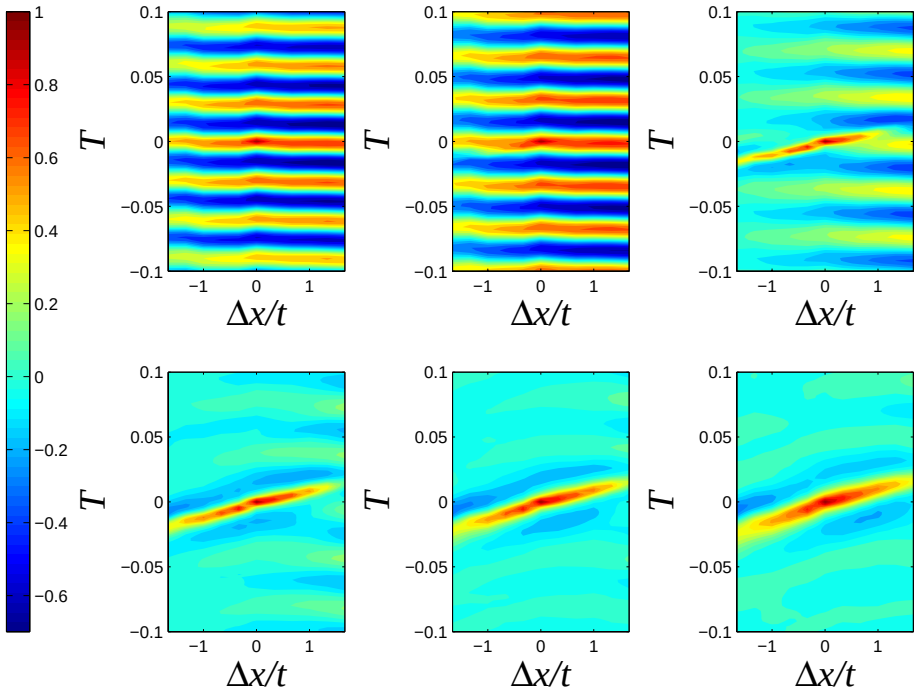

Figure 3.18. Contours are the normalized cross-correlation coefficient at different time lags, T, between pressure taps with different spacing, Δx, originating at $x_0 = 5.17t$. From top left to bottom right: 0°, 30°, 45°, 60°, 75°, 90°. Colour map applies to all figures.

The estimate of size and convection speed of leading edge vortices was performed in §3.1.2. The same analysis is performed near the trailing edge of the model to determine the persistence of the leading edge disturbance. Thus, using Eq. (3.6) with $x_0 = 5.17t$, the persistence of leading edge structures near the trailing edge is shown in Figure 3.18. For bodies that are leading edge dominated, as defined above, it is observed that the disturbance found at the leading edge (Figure 3.8) is still strong at the trailing edge. However, as the leading edge separation angle decreases, there is an increasing oscillatory correlation in time at each shown streamwise position, which is due to the strong trailing edge vortex shedding. These observations are discussed in the following section.

3.2 Discussion

3.2.1 *Elliptical leading edge*

The elliptical leading edge was used in this study as a benchmark since it has no leading

edge separation and only trailing edge vortex shedding. It is observed to have the highest shedding frequency and a similar base pressure to the model with a leading edge separation angle of 30°. These parameters are traditionally understood to represent the strength of vortex shedding (Roshko, 1954a) which implies that the elliptical leading edge has strong trailing edge vortex shedding. The lift fluctuations were also observed to be high; however, not as high as some other bodies which are discussed in the following section.

Vorticity is generated along any surface and the case of the elliptical leading edge is no exception. A small amount of circulation is generated in comparison with the models with leading edge separation. However, the poor spanwise correlation near the leading edge reveals the three-dimensional nature of the flow already at this location. Near the trailing edge ($x = 6.17t$), the flow is shown to be much better correlated along the span of the model.

The correlation at the trailing edge of the body shows the susceptibility of the flow along the surface to be influenced by the trailing edge vortex shedding. Many data presented herein show the periodic nature and the extent to which the flow is correlated across the span (e.g., Figure 3.10). However, the case of the elliptical leading edge urges caution in the interpretation of the pressure contours of Figure 3.12. The organized and periodic appearance of the pressure contours in this plot might be perceived as footprints of leading edge vortices passing this location. However, the lack of leading edge separation, lack of convecting structures (Figure 3.8) and the poor correlation at the leading edge of this body reveal that these contours do not represent vortices in this case and thus, do not necessarily represent vortices in the other cases – although it does not rule out this interpretation either. Rather, the pressure at this location oscillates with the period of vortex shedding in the recirculation region.

Bursting was found for all bodies tested and is discussed in greater detail in the following sections; however, it is a dominant feature in the base region of the body with an elliptical nose as well. This phenomenon has been observed by many authors (e.g., Wu et al., 2005 and references therein); however, its cause remains unknown. The existence

of bursting for the case of no leading edge separation herein is important, however, to contextualize the discussion on its importance to the flow around the bodies with leading edge separation.

3.2.2 *Balance between leading edge separation and trailing edge vortex shedding*

The dual phenomena occurring in the case of flow over elongated bluff bodies has largely been analyzed in the context of rectangular cylinders at low Reynolds numbers. At low Reynolds numbers, there is a relatively clear understanding of the mechanisms producing the vortex shedding wake. The ILEV instability, as has already been discussed, forms a feedback between leading edge vortex shedding and those vortices passing the trailing edge. Although the magnitude remains unclear of the pressure pulse emitted from a vortex passing the trailing edge, it has been readily shown (e.g., Nakamura et al., 1991) that the ILEV instability is suppressed for many elongation ratios once $Re > 2000$. However, it is also well known, as it has been shown herein, that vortices are still shed from the leading edge separation bubble at higher Reynolds numbers even though they are not emitted at any regular frequency. Thus, the resultant wake is the combination of these vortices shed at apparently random intervals from the leading edge with the much more periodic process of trailing edge vortex shedding. In this section, the balance between these phenomena is addressed.

The synchronization between the leading edge separation bubble (referred to as the leading edge hereafter) and the trailing edge vortex shedding was shown to be discernable near the start of the separation bubble. It should be noted, however, that the synchronization was shown to be strongest for the elliptical leading edge. Although shear layers are known to be highly sensitive to forcing, by the time the shear layer reattaches to the body, there was no discernable synchronization between these two locations – a result reinforced by the lack of periodic leading edge vortex shedding. Since the timing between these two locations is observed not to be relevant, the magnitude of the fluctuations must play an important role in the interaction. The magnitude of the fluctuations at two points does not give an integral sense of either location; however, the ratio plotted in Figure 3.17 between the two points of maximum fluctuation at the leading

edge and trailing edge seems to categorize the observed data well.

For bodies which were observed to be trailing edge dominated, it was observed that bursting events were stronger in magnitude and much more likely to occur. It was also evident that the spanwise correlation was much stronger in general and more susceptible to increases during bursting events. For the two bodies which were leading edge dominated, the spanwise correlation was generally poor and did not improve appreciably during apparent bursting events. However, the most telling feature of the leading edge dominated bodies was the persistence of leading edge structures at the trailing edge.

For the elliptical leading edge and for the body with a leading edge separation angle of 30°, there are no detectable leading edge structures in Figure 3.8. The footprint of the leading edge structures (Figure 3.18) is easily observed for the leading edge dominated bodies. However, there is a continual transition between the two extremes. It is this plot (Figure 3.18) which best epitomizes the interaction between leading edge and trailing edge flows. The forcing of the flow near the trailing edge by the vortex shedding in the base region is clearly evident (e.g., Figure 3.10) yet there remain strong disturbances from the leading edge. These disturbances were shown to significantly affect wake formation in the force balance analysis of Chapter 2.

The scale of the leading edge vortices can be estimated several ways: from the breadth of the contours around the ridge in Figure 3.8 (as well as Figure 3.18) and from the mean reattachment length (Figure 3.4). These vortices were all shown to convect at the same speed away from the leading edge separation bubble in no discernibly periodic fashion. Thus, it is assumed that it is primarily the size of the leading edge structures which is important at these Reynolds numbers. This assumption leads to the following proposed mechanism.

Once the leading edge vortices become sufficiently large, they overwhelm the forming trailing edge vortices and it becomes difficult for the trailing edge vortex shedding to establish itself, even though it persists. The balance between the leading edge and the trailing edge is observed to be less like a conventional instability, since there does not appear to be significant synchronization between the two, and more like a competition

between the strength, or magnitude, at the two locations. If the scale of the structures shed from the leading edge can compete with the strength of those at the trailing edge, they are shown to significantly alter the flow dynamics. On the other hand, when the scale of the leading edge separation is small, there is also a marked change due to the presence of the leading edge separation. This notion is discussed further in connection with shedding frequency and lift fluctuations in the following section.

3.2.3 *Effects of the competition between leading and trailing edge*

The previous section discussed the competition between leading and trailing edge flows. The impact that this competition has on the wake characteristics is now discussed in terms of this notion. The elliptical leading edge is taken as the base case and the trailing edge vortex shedding proceeds generally as that described by Gerrard (1966) although with relatively thicker boundary layers than those in the wake of circular cylinders. As leading edge separation is introduced, vortices are shed from the leading edge. From the results herein, these structures are detectable at the trailing edge for the cases when the leading edge separation angle is greater than 45°. These structures disturb the strong periodicity associated with the persistent trailing edge vortex shedding of the elliptical leading edge. With increasing leading edge separation angle, these disturbances are also increasingly three-dimensional with poor spanwise correlation. This type of disruption is hypothesized to lower the shedding frequency which is in agreement with suggestions made by Gerrard (1966). Gerrard (1966) hypothesized that the more difficult the interaction between opposing shear layers, the lower the shedding frequency. Coupling these disruptions with the observation that there is no significant jump between leading and trailing edge domination (e.g., Figure 3.17, Figure 3.18), an explanation for the linear variation of the Strouhal number is now suggested.

Simpson (1989) expects a roughly linear variation in the reattachment length with increasing separation angle as was also found herein. The mean reattachment length is a reasonable approximation to the size of the leading edge disturbances, thus the linear variation in the Strouhal number could simply be the result of a linearly increasing leading edge disturbance. If there was a strong dependence on the synchronization between these two locations, as there is at low Reynolds numbers, one would expect

shedding frequencies to be selected on the basis of one or more instabilities. For example, Liu (2009) showed that there are bounding options for frequency selection at low Reynolds numbers. The lower bound is the case of the ILEV instability for rectangular cylinders which has a stepwise variation in the chord based Strouhal number with elongation ratio and the upper bound is the elliptical leading edge which shows a linear variation with separation angle. They also show that for the case of a leading edge separation angle of 45°, the frequency locks to one mode before switching to another once the chord is slightly elongated. The results herein, with the lack of frequency communication between these locations show that this is not the mechanism which occurs at higher Reynolds numbers. Rather it is suggested that it is simply the scale of the leading edge disturbance which most affects shedding frequency and could explain the linear variation observed in Figure 3.3.

The leading edge separation angle is also observed to have a significant effect on the fluctuating lift; however, the existence of a peak lift fluctuation is in contrast with the linear decrease of shedding frequency. These results might have been anticipated by the hypotheses of Gerrard (1966) who suggested that even if the frequency is decreased due to a disturbance, this disruption can also lead to less vorticity cancelled out by reduced entrainment of oppositely signed vorticity which in turn increases circulation in the shed vortex and, ultimately, the fluctuating lift. This point was also addressed in Chapter 2 where higher wake vortex circulations and lift fluctuations were found for the case of a triangular-edged elongated bluff body compared to a body with a higher shedding frequency.

The present results show that the fluctuations in the base pressure can be higher in magnitude close to the boundary of the base region ($y \rightarrow 0.5t$) for the case of $\gamma = 30°$ compared with the elliptical nosed body even though they share the same mean and fluctuating base pressure (i.e., that measured at $y = 0$). This observation suggests formation of the vortices closer to the top of the base region than the middle. The formation of vortices closer to the top of the base region can either be attributed to the increased circulation (of the same sign) drawing the growing vortex towards the edge of the base region or a reduction in the entrainment of the opposing shear layer due to the

leading edge disturbance. Either one or both may be occurring and this type of interaction will produce higher lift fluctuations compared with the elliptical leading edge for much the same reasons as suggested by Gerrard (1966). As the separation angle is increased further (i.e. $\gamma > 60°$), the flow from the leading edge becomes highly three-dimensional, the strength of the TEVS is decreased and thus its ability to correlate the trailing edge flow is also decreased thus, once again, lowering the lift fluctuations.

Another factor limiting the lift fluctuations at higher separation angles is the observed suppression of bursting events. Bursting events are known to be associated with strong shedding and high lift fluctuations for circular cylinders (Szepessy and Bearman, 1992). The burst events identified herein are shown to produce the highest lift fluctuations for the bodies with small separation angles. Thus, the suppression of bursting events is expected to lower the time-averaged lift fluctuations. However, it remains unclear if it is the scale of the leading edge disturbance which suppresses bursting at the trailing edge or if it is the high three-dimensionality for large leading edge separation angles. Burst events were observed to be preceded by strong three-dimensional correlation near the trailing edge (also observed by Szepessy and Bearman, 1992 for circular cylinders); however, the poor correlation of structures shed from the leading edge at high leading edge separation angles does not allow this precursor to bursting events and correlation near the trailing edge remains poor. Thus, the dominance of the leading edge flow is suggested to be the reason for reduced burst events which are primarily a feature of trailing edge vortex shedding.

3.3 Conclusions

For rectangular cylinders at low Reynolds numbers, the frequency selection is largely based on the ILEV instability. However, the shedding frequency at the higher Reynolds numbers examined herein is suggested to be determined by the competition in magnitude between the separating-reattaching flow at the leading edge and the vortex shedding at the trailing edge. As the leading edge separation angle increased it was observed that the vortices shed from this location increased in scale as well. The only frequency about which any energy was detected at the leading edge separation bubble was that of a low frequency flapping, thus the leading edge vortices were not shed at periodic intervals.

The lack of synchronization between leading and trailing edge flows was observed to lead to a competition of respective magnitudes in the determination of the overall flow properties. Importantly, the transition between leading and trailing edge domination was observed to be essentially continuous with no jump between instabilities typical of lower Reynolds numbers. It should be noted that testing at other elongation ratios is required to prove conclusively that no jumps occur at higher Reynolds numbers in general.

Due to the continuous nature of this transition, the Strouhal number was observed to decrease approximately linearly. However, the fluctuating lift does not show the same linear trend. For the fluctuating lift, a peak was observed for a leading edge separation angle of 30°. The circulation generated at the leading edge is the most significant for this body; however, the scale of the leading edge disturbance remains small thus the increased circulation interacts with the dominant trailing edge vortex shedding to produce the highest fluctuating lift, yet without having the highest shedding frequency. Another contributor to the observed lift fluctuations was the existence and suppression of bursting phenomena like that observed in circular cylinder wakes. For bodies that were leading edge dominated herein, the bursting phenomenon was essentially suppressed due to the highly three-dimensional flow shed from the leading edge. It was shown that just prior to bursting events the flow becomes well correlated across the span and remained so during bursting events. Thus, the significant three dimensionality of the flow from high leading edge separation angles is suggested as the cause for the suppression of bursting events and resultant decrease of the lift fluctuations.

The case of elongated bluff body flows at higher Reynolds numbers was explored herein and the method of frequency selection in the wake encouragingly appears more straightforward, in some respects, than that of the same bodies at lower Reynolds numbers. Without external forcing, the shedding frequency appears to be dependent on the competition between the strength of the leading edge separation and the trailing edge vortex shedding. However, the strength of the trailing edge vortex shedding is also shown to be highly dependent on the scale of the leading edge separation. The reverse, however, is not true. There appears to be little-to-no dependence of the leading edge separation on the trailing edge vortex shedding. The three-dimensionality of these flows

was also shown herein and further studies are encouraged to better understand how the significant three-dimensionality of the leading edge structures interacts and decreases the frequency and strength of the trailing edge vortex shedding. Future studies are required incorporating more elongation ratios as well as higher Reynolds numbers to be able to better understand the variation of the shedding frequency. However, the results herein show a stark departure from what would be expected for lower Reynolds numbers with the overall flow being largely determined by a competition of energetic magnitudes at the leading and trailing edges as opposed to a synchronization (or lack thereof) between the two locations.

Chapter 4

Wake structure of elongated bluff bodies using proper orthogonal decomposition

As alluded to throughout the previous chapters, much is already known about the mechanisms of trailing edge vortex shedding from shorter bluff bodies. One relatively recent path used to better understand the wakes of circular cylinders is proper orthogonal decomposition (POD). Decomposing these wakes through POD allows for the understanding of the important spatial features necessary to describe the wake. Many studies have been performed on circular cylinders (Deane et al., 1991; Ma and Karniadakis , 2002; Noack et al., 2003) as well as on other shapes such as the square cylinder (van Oudheusden et al., 2005). These wakes are shown to be dominated, energetically, by the fundamental trailing edge vortex shedding. The dominance of this feature leads to the possibility of low-order modeling of the wake (Ma and Karniadakis, 2002). POD has also been applied to other classical flows such as turbulent boundary layers (Gurka et al., 2004) and mixing layers (Lardeau et al., 2010) to further the understanding of their spatial structures.

In the previous chapters, a mechanism regarding the competition between leading edge and trailing edge flows has been suggested. This competition seemed to be dominated by the magnitudes of the pressure fluctuations at each location rather than by the synchronization typical of lower Reynolds numbers. The pressure fluctuations represent the fluctuating energy in the flow, but not in an integral sense. In the current chapter, this competition is examined by performing POD on the wake. This decomposition reveals the most energetic features of the flow. Thus, it is expected that the balance of pressure fluctuations observed in Chapter 3 will manifest itself in terms of decomposed wake structures herein. The energy associated with the modes is then expected to reflect the balance between the leading edge separated flow and the trailing edge vortex shedding and better quantify the notion of competition presented in the previous chapters. The data analyzed in this chapter are taken by PIV in the wake of the three symmetric elongated bluff bodies (refer to §1.1 for details).

4.1 Results

4.1.1 *Pressure measurements*

The surface pressure measurements from each body are integrated to yield sectional lift and drag coefficients (see Table 4.1). Also presented in Table 4.1 is the Strouhal number, $St = ft/U_\infty$, which has been determined from the power spectra of the lift coefficients (for plots of the spectra, the reader is referred to Chapter 2). The shedding frequency for the square-edged body agrees well with that measured at lower Reynolds numbers by Nakamura et al. (1991) and the shedding frequency of the circular-edged body close to the value of 0.26 found experimentally by Nguyen and Naudascher (1991). It is observed that all the bodies have distinct shedding frequencies and bluffness, the latter being shown by the sectional drag coefficient. One of the immediate observations from this data is the strength of the sectional lift fluctuations, C'_L, of the triangular-edged body. From established trends of shorter bluff bodies it is expected that a lower shedding frequency corresponds to weaker vortex shedding (Roshko, 1954a). However, the stronger vortex shedding of the triangular-edged body seem to reflect the levels of interaction between the separated shear layers in the recirculation region. This observation is returned to in §4.2.

4.1.2 *Recirculation region*

The objective of this chapter is a better understanding of the wake structure for elongated bluff bodies. For shorter bluff bodies, it is the recirculation region, where most of the interaction occurs, that determines the features of the vortex street wake (Gerrard, 1966). Thus, in this section, distinctions are noted in the recirculation region which will be connected to the wake structure studied by POD in later sections.

Table 4.1. The Strouhal number (from Chapter 2) and sectional aerodynamic coefficients

Edge shape	C_D	C'_L	St
Circular	0.58	0.055	0.24
Triangular	0.81	0.059	0.19
Square	1.13	0.037	0.15

The results of Chapter 2 suggest that the recirculation region is the predominant region for the wake formation of elongated bluff bodies. However, while the interacting shear layers are relatively thin for shorter bluff bodies, for elongated bluff bodies these boundary layers can be of significant size with embedded leading edge vortices. The force balance of the recirculation region (Chapter 2) shows that the shear stresses along the edge of the recirculation region become increasingly influential as the leading edge separation angle increases. In light of this observation, a distribution of fluctuating flow angles is calculated at the edge of the recirculation region. This distribution is essentially a quadrant analysis and is computed at one-third the length of the recirculation region for each body, on the separation streamline, where the end of the recirculation region is defined as the saddle point in the time-averaged velocity field. The fluctuating flow angle, $\beta' = \tan^{-1}(v'/u')$-$\langle \beta \rangle$, is the angle between the fluctuating flow vector and the streamwise direction. It is this fluctuating angle for which the distribution in Figure 4.1 is computed. The data presented are for the top ($y > 0$) of the recirculation region, therefore, a positive v' value points out of the recirculation region. It is observed that the most probable fluctuating flow angle for the circular-edged body, as well as the triangular-edged body, are more horizontal than for the square-edged body. The square-edged body is observed to have a broad range of fluctuating velocity with significant upwards, vertical fluctuations. This result indicates that the momentum transfers at the edge of the

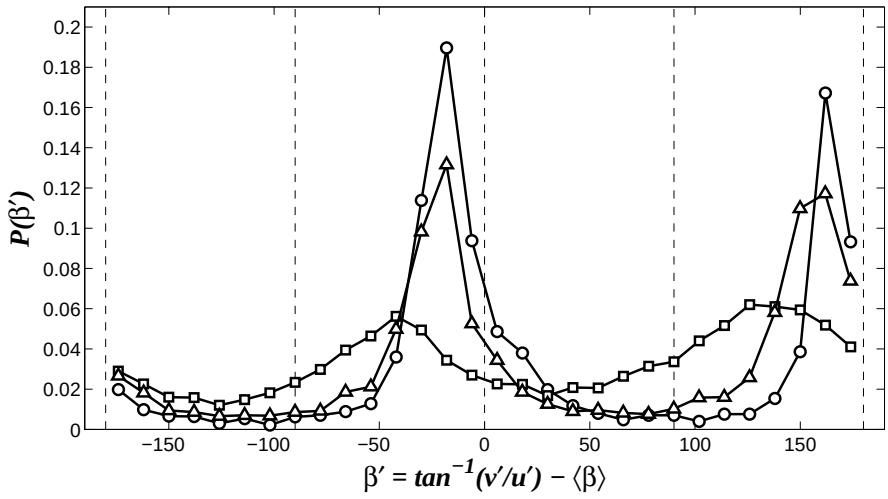

Figure 4.1. Distribution of the fluctuating velocity vector taken at one third of the length of the recirculation region of each body: ○- circular-, Δ - triangular- and □- square-edged bodies.

recirculation region for the square-edged body are a departure from the more conventional vortex shedding wake of the circular-edged body. The features of the flow which may be responsible for this departure are explored in the following sections.

4.1.3 *Proper orthogonal decomposition*

Lumley (1970) was the first to suggest the use of POD in the study of turbulent flows. In the utilization of POD to turbulent flows, the set of functions to be decomposed is typically comprised of either numerical (e.g., Diamessis et al., 2010) or experimental data (e.g., Gurka et al., 2006). The functions that are decomposed herein are the velocity and vorticity fields extracted from the PIV data taken in the wake of the three elongated bluff bodies. The result of the POD is empirical eigenfunctions which will hereafter be referred to as POD modes. These modes are sorted such that the lowest numbered mode represents the most energetic feature of the wake and each subsequent mode is less energetic than the preceding mode.

The details of the proper orthogonal decomposition algorithm employed herein are now outlined. The algorithm follows the implementation of the snapshots method proposed by Sirovich (1987) and as laid out in Diamessis et al. (2010). This method has been employed since the number of snapshots, ($M \sim 2000$), is significantly fewer than the number of data points in every snapshot ($N \sim 6400$), which is the criterion for improved performance. The eigenvalue problem is given by,

$$C \cdot \psi = \lambda \cdot \psi \tag{4.1}$$

$$C = \Omega^T \cdot \Omega, \quad \Omega = \begin{bmatrix} \omega'_z(x_1, y_1, \tau_1) & \omega'_z(x_1, y_1, \tau_2) & \cdots & \omega'_z(x_1, y_1, \tau_M) \\ \omega'_z(x_2, y_1, \tau_1) & \omega'_z(x_2, y_1, \tau_2) & & \omega'_z(x_2, y_1, \tau_M) \\ \vdots & \vdots & \ddots & \vdots \\ \omega'_z(x_q, y_p, \tau_1) & \omega'_z(x_q, y_p, \tau_2) & \cdots & \omega'_z(x_q, y_p, \tau_M) \end{bmatrix} \tag{4.2}$$

Matrix C is defined in Eq. (4.2) where each column of the matrix Ω represents the spanwise fluctuating vorticity (denoted by the prime) of a p x q PIV snapshot at time τ. The fluctuating vorticity is computed by subtracting the time-averaged mean from each spatial location. The reader is referred to Sirovich (1987) or Smith et al. (2005) for the remainder of the method which is written therein for the decomposition of velocity.

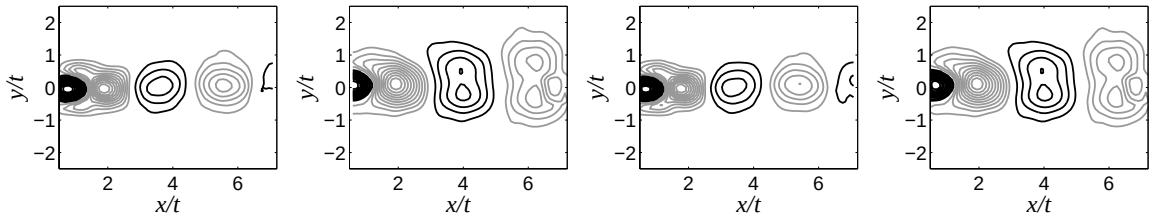

(a) (b) (c) (d)

Figure 4.2. Comparison of the vorticity (positive - black, negative - grey) of the first POD mode decomposed by velocity: (a) circular-, (b) triangular-edged body; and by vorticity: (c) circular-, (d) triangular-edged body.

As is written above, the POD formulation is written herein such that the algorithm will be performed upon the vorticity calculated from the PIV data. The single, out-of-plane, component of vorticity is computed using a second order, least-squares differentiation scheme, which has been shown to provide minimal error in the estimation of vorticity compared to other numerical differentiation schemes for PIV data (Liberzon et al., 2001).

A comparison between the decomposition of vorticity and a decomposition of the velocity fields is shown in Figure 4.2. The modes plotted therein are the first mode for both the circular- and triangular-edged bodies. The differences between the two (i.e., velocity and vorticity) are nearly imperceptible; however, differences were noted in higher modes. POD by vorticity captures these higher modes more accurately than POD by velocity since it is typically vortical structures that comprise the "coherent" structures that were originally sought by Lumley (1970).

Many numerical simulations now employ some form of POD computation and Galerkin projection to increase efficiency (Rapun and Vega, 2010). An analogous method is employed herein by reconstructing an instantaneous PIV realization using the POD modes (Smith et al., 2005). The following performs this reconstruction,

$$\hat{\omega}(\vec{x},\tau_n) = \sum_{i=1}^{M} \omega(\vec{x},\tau_i) + \sum_{j=1}^{K} a_j(\tau_n)\phi_j(\vec{x}) \tag{4.3}$$

where K is the number of modes included in the reconstruction ($K < M$). The coefficient, a, and eigenfunction, ϕ are computed from the POD. The vorticity of the individual PIV snapshot is computed and compared with the corresponding reconstruction using the first

K = 50 POD modes for the triangular-edged body (Figure 4.3). While distinctions are observed, it is evident that the main vortical features of the flow are described sufficiently well by the modes used.

4.1.4 *Energy of the POD modes*

The proper orthogonal decomposition gives a direct estimate of the relative energy of each spatial mode (eigenfunction) through the corresponding eigenvalues. The energy convergence of the modes is shown in Figure 4.4a. It is observed that the circular- and triangular-edged bodies converge faster than the square-edged body. The energy decay with increasing mode number is plotted in Figure 4.4b. For the circular- and triangular-edged bodies there are distinct steps down in energy over the first 8 modes. This pattern agrees with the decomposition shown by Ma and Karniadakis (2002) in their three-dimensional numerical simulations of flow past a circular cylinder at a Reynolds number of 185. The steps show that the energy content is approximately the same over two modes. It will be shown that these two modes represent the same flow feature and can, thus, be said to be paired. The square-edged body, meanwhile, is shown to have only one such pairing before the steady decay of energy begins. This result, along with previous work (e.g., Parker and Welsh, 1983; Chapter 2), suggests that the circular- and triangular-edged bodies' wakes are dominated by "strong" periodic vortex shedding and, while the square-edged body has some periodicity, it is not as strong or as regular as the other two bodies.

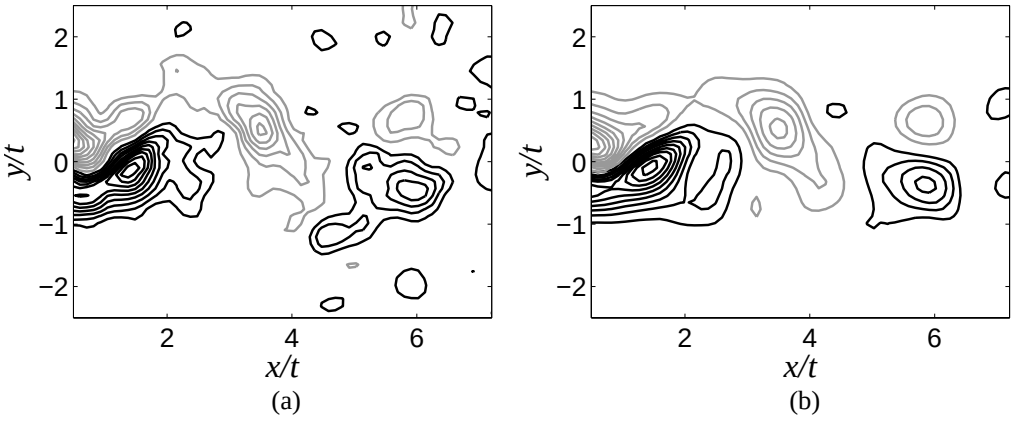

Figure 4.3. Reconstruction (b) of an instantaneous snapshot (a) using the first 50 POD modes. Black and grey contours represent positive and negative vorticity, respectively.

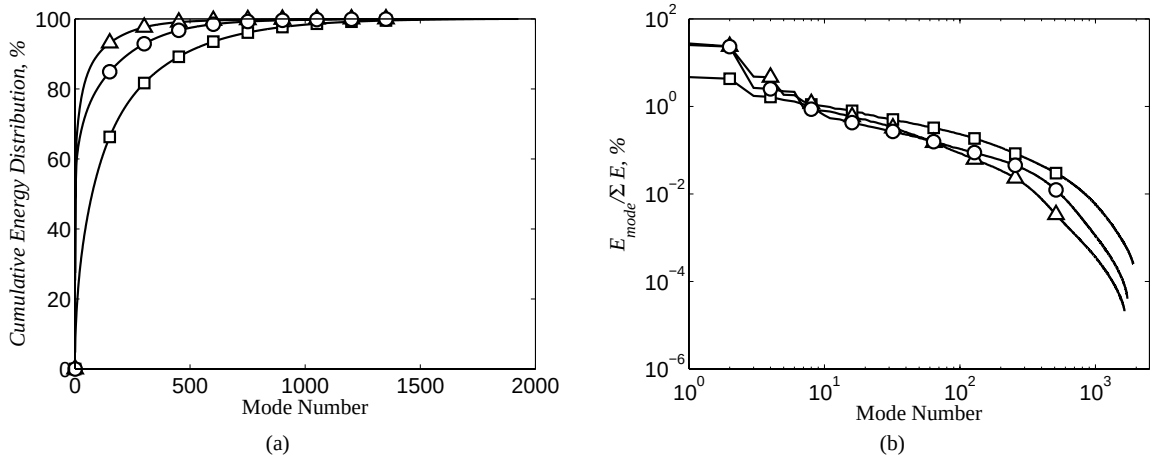

Figure 4.4. Plots of the energy variation in the POD modes: (a) cumulative distribution and (b) relative energy in each mode. Symbols are present to distinguish lines and do not mark each data point: ○- circular-, Δ - triangular- and □- square-edged bodies.

For the bodies with periodic vortex shedding, the first two modes are observed (from Figure 4.4a to contain approximately 50% of the total energy. In contrast, for the square-edged body, it requires nearly two orders-of-magnitude more, (approximately 100 modes) to contain half of the total energy. Figure 4.4b shows the variation of energy in each mode with these values listed for the first 8 modes in Table 4.2. Regarding the energy content in each mode, it should be reiterated that the POD is performed on the fluctuations of the vorticity field thus the estimate of the energy reflects the contribution of each mode (in %) to the total fluctuating enstrophy.

It is observed that the triangular-edged body contains more energy in the second mode pairing compared to the one with circular edges. The third mode of these two bodies is observed to contain similar amounts of energy with the mode pairing of the circular-edged body being slightly more energetic. However, the fourth mode pairing exhibits

Table 4.2. Percentage of the overall energy from the POD

Mode pair	Square-edge		Triangular-edge		Circular-edge	
	First	Second	First	Second	First	Second
1 & 2	4.68	4.23	27.4	23.5	25.3	23.2
3 & 4	1.74	1.64	4.79	4.63	2.65	2.51
5 & 6	1.41	1.30	1.84	1.81	2.22	2.15
7 & 8	1.11	1.11	1.29	1.16	0.93	0.87

more energy for the triangular-edged than the circular-edged body – an important point which is discussed in §4.2. Observations of the modes higher than the first 8 for the triangular- and circular-edged bodies, and the first 4 for the square-edged body indicate that the patterns are no longer ordered spatially. In other words, it is anticipated that these lower energy modes reflect either effects of turbulence or small experimental error. Thus, while some of the upper mode pairs contain a relatively small percentage of the total fluctuating enstrophy (Table 4.2) their spatial patterns suggest that they remain important in the description of the overall physics.

4.1.5 *POD modes: "Strong" vortex shedding bodies*

As was mentioned in the previous section, the circular- and triangular-edged bodies present energy curves that show similarities to other decompositions of vortex shedding bodies reported in the literature. In this section, the modes and phase information of the decomposition are examined to determine the characteristic features of these vortex shedding wakes.

Figure 4.2c-d show the first mode for the "strong" vortex shedding bodies. However, as has been shown in the energy curves of these bodies, the modes are paired up to mode 8. Thus, the second mode is paired with the first of each body and is shown in Figure 4.5. The PIV data have been sampled at a sporadic sampling frequency and information about the timing of each snapshot is not available. However, the spatial features reveal that modes 1 and 2 represent the same periodic feature with mode 2 shifted by approximately

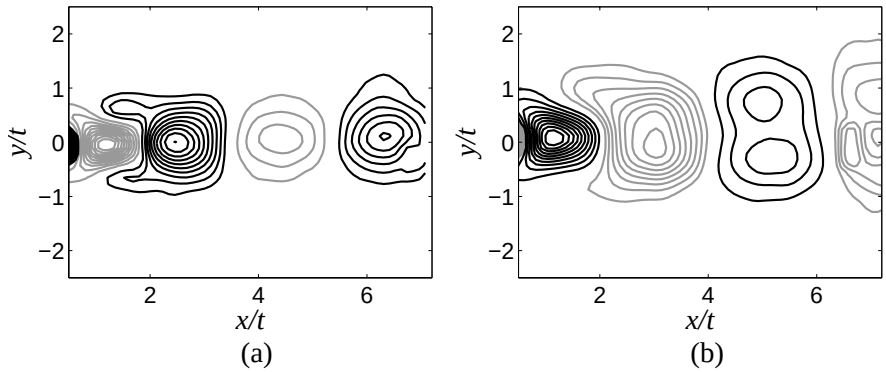

Figure 4.5. Mode 2 from POD of vorticity (positive - black, negative - grey): (a) circular-, (b) triangular-edged body.

0.25Λ from mode 1, where Λ is the wavelength.

Modes 3 through 6 are shown in Figure 4.6 for the bodies with circular and triangular edges. The wake of low Reynolds number circular cylinders has been decomposed by different researchers (e.g., Deane et al., 1991; Ma and Karniadakis, 2002; Noack et al., 2003) and serves as a reference for the bodies herein. Even though the Reynolds numbers are approximately two orders-of-magnitude apart, the strong periodicity observed in the wake of the circular- and triangular-edged bodies leads to similarities in the decomposed modes. A feature readily apparent from the decomposition is the existence of a dominant feature (the vortex shedding) and its harmonics. With the spatial data from the decomposition, wavelengths are estimated by averaging the distance between regions of maximum and minimum vorticity (i.e., positive and negative) using both modes of a mode pairing and subsequently doubling this half-wavelength. These wavelengths are reported in Table 4.3 where it is observed that modes 3 & 4 and modes 5 & 6 are, respectively, the second and third harmonics of the fundamental vortex shedding mode. It should be noted that because of the acceleration of vortices in the near wake (Balachandar et al., 1997; Chapter 2), these wavelengths are slowly changing with distance downstream; however, care was taken to estimate wavelengths at the same wake location to minimize possible errors. The ratios between the wavelengths of each body with the circular-edged body have also been computed (see Table 4.3). These ratios are

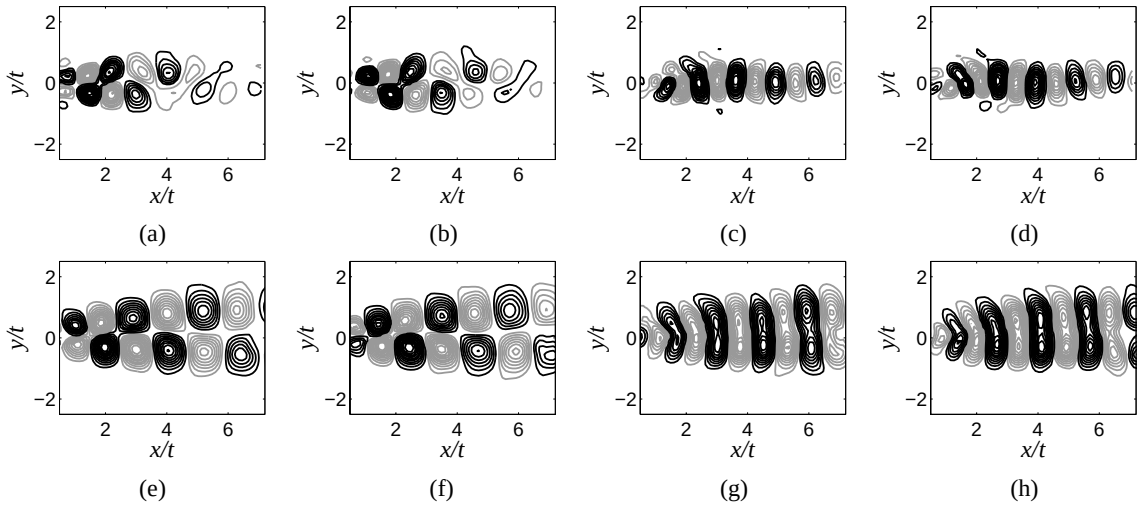

Figure 4.6. Modes 3-6 (left to right) from POD of vorticity (positive - black, negative - grey): circular- and triangular-edged bodies are top and bottom rows, respectively.

Table 4.3. Spatial features extracted from the POD

Edge shape	$\Lambda_{1\&2}/t$	$\Lambda_{3\&4}/t$	$\Lambda_{5\&6}/t$	St_{circ}/St	$\Lambda_{1\&2}/\Lambda_{1\&2,circ}$
Circular	3.30	1.65	1.10	1	1
Triangular	4.24	2.20	1.55	1.26	1.28
Square	5.24	-	-	1.60	1.64

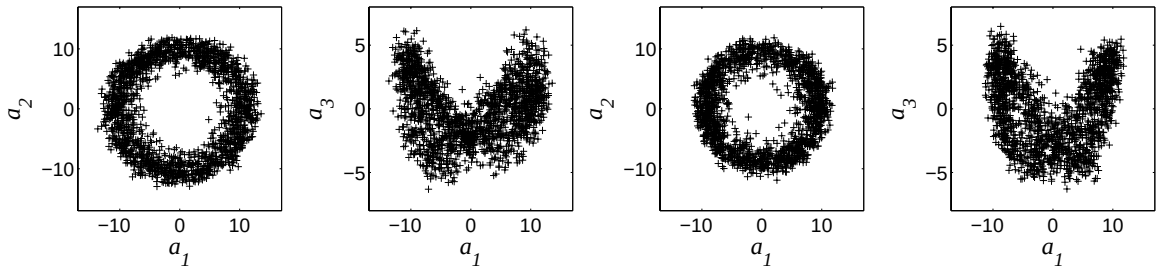

(a) (b) (c) (d)

Figure 4.7. Phase plots from the POD for the circular-edged (a) & (b) and triangular-edged (c) & (d) bodies.

compared with the ratios between the Strouhal numbers which provides further evidence that the first mode pairing represents the dominant frequency in the wake.

Aside from the measured wavelengths, other spatial features emerge from Figure 4.2, Figure 4.5 and Figure 4.6. The spatial features of the decomposed modes herein are also compared with the results of Noack et al. (2003) for a circular cylinder. The first mode pairing (modes 1 & 2) of the circular-edged body and the first mode pairing of the circular cylinder (Noack et al., 2003) seem to be qualitatively similar. The first mode pairing of the triangular-edged body, however, contains a structure which is observed to have two "lobes" or, in other words, two regions of peak vorticity contained within the structure (Figure 4.5b). The next mode pairing for the circular- and triangular-edged bodies (modes 3 & 4) are similar to each other; however, the centres of maximum vorticity are further from the wake centreline for the triangular-edged body. In modes 5 & 6, the existence of two lobes is once again observed for the triangular-edged body (Figure 4.6g-h) where it is not observed in the wake of the circular-edged body or for the low Reynolds number circular cylinder (Noack et al., 2003).

The phase plots for the first and second harmonics of the circular- and triangular-edged bodies are shown in Figure 4.7. Referring to the spatial wavelengths that were estimated

in Table 4.3, these phase plots offer further evidence that the most dominant feature of these two wakes is the trailing edge vortex shedding and its harmonics. The underlying attractor in both Figure 4.7a & c presents a circular orbit. This circular pattern agrees well with the findings of Deane et al. (1991) in their attempt to construct a lower dimensional formulation of the vortex shedding wake of circular cylinders. However, there is significantly more scatter at this higher Reynolds number. It is more difficult to discern the attractor in Figure 4.7b & d; yet, beneath the scatter it is possible to observe the "butterfly" orbit found by both Deane et al. (1991) and Ma and Karniadakis (2002) at lower Reynolds numbers.

4.1.6 *POD modes: Square-edged body*

As far as bluff bodies are concerned, rectangular cylinders are remarkable oddities. Parker and Welsh (1983) showed that these bodies do not regularly shed vortices for a wide range of elongation ratios. However, it was shown in Chapter 2 that there is a discernible vortex shedding peak in the frequency spectrum even though it is quite weak and broad-banded. In this section, the structure of the wake is explored through POD and will be compared with the other two bodies, both of which were observed to have strong vortex shedding wakes.

The results of the energy variation for the square-edged body in §4.1.4 suggest that the first two decomposed modes will be different from the first two modes of the bodies with

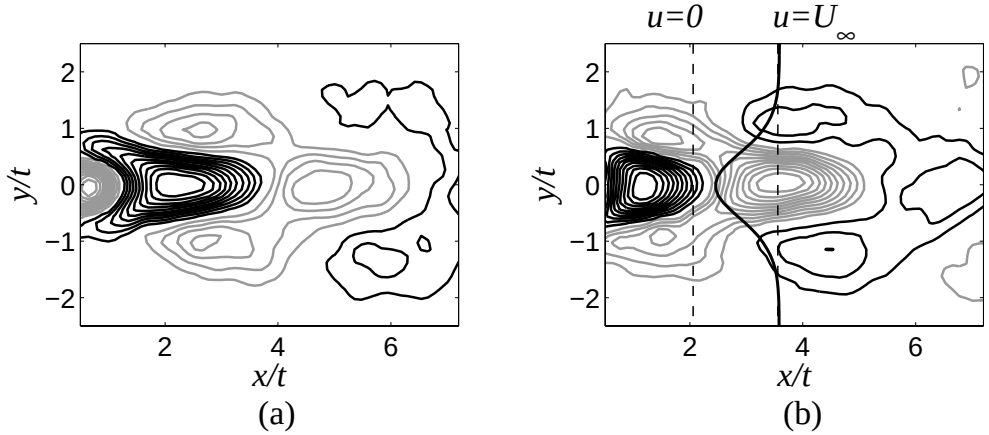

Figure 4.8. First mode pairing from the POD of vorticity (positive - black, negative - grey) on the wake of the square-edged body: (a) Mode 1, (b) Mode 2. Time-averaged velocity profile is shown, (b), for $x=2t$.

strong vortex shedding. These two modes are shown in Figure 4.8 and the estimation of the wavelength is given in Table 4.3. Note that additional wavelengths have not been added to Table 4.3 due to the lack of regular structures in the higher modes of the square-edged body. The wavelength that has been calculated for this mode pairing is for the structures on the wake centreline ($y = 0$). It is observed that these modes exhibit structures with three lobes. There is a region of high vorticity on the wake centreline which is similar to the other two bodies. However, the two lobes connected to the centreline lobe on either side of $y = 0$ distinguish this pattern compared with the first mode pairing of the other two bodies.

To further the contrast between the wake of the square-edged body and the wake of the two other bodies, similar phase plots have been computed for the square-edged body as were calculated for the other two bodies in Figure 4.7. These phase plots for the square-edged body are shown in Figure 4.10. It is observed from the a_1-a_2 phase plot that, while there may be a hint of a circular orbit, it is not indicative of the entire dataset. Rather a loosely bounded circle is observed with data scattered all the way throughout as opposed to a locus of points around the circumference.

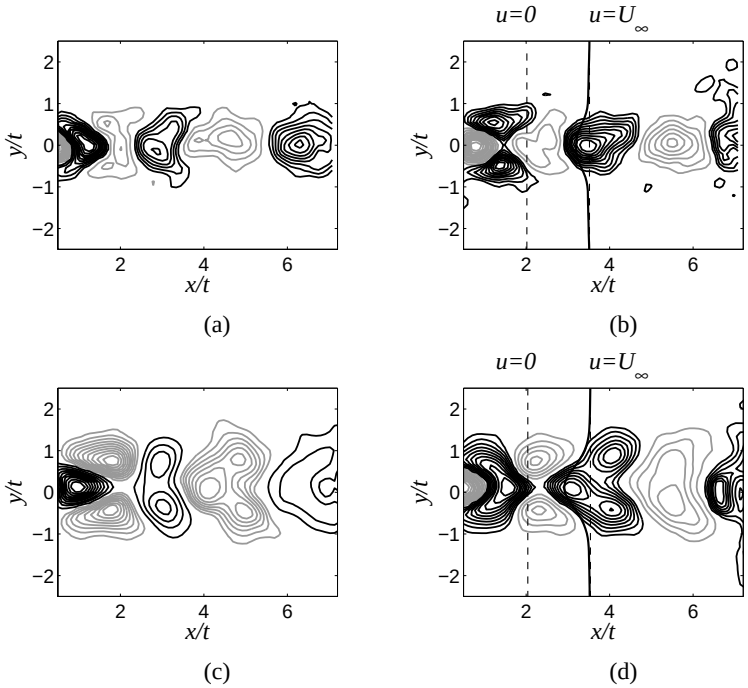

Figure 4.9. Modes 7 & 8 from POD of vorticity (positive - black, negative - grey) of: (a)-(b) circular- and (c)-(d) triangular-edged bodies. Time-averaged velocity profiles are shown for $x=2t$.

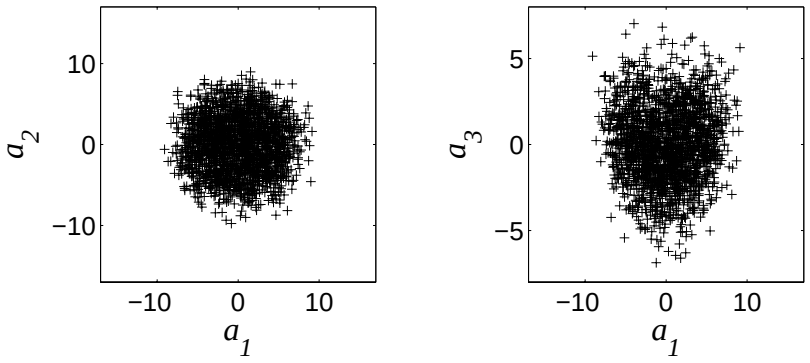

(a) (b)

Figure 4.10. Phase plots from the POD for the square-edged body.

A comparison is now made between the higher (lower-energy) modes of the circular- and triangular-edged bodies (shown in Figure 4.9) and the first two modes of the square-edged body. The similarity between the first mode pairing of the square-edged body and this mode pair for the triangular-edged body (7 & 8, shown in Figure 4.9c & d), is seen in the form of a three-lobed pattern. In this mode pairing for the circular-edged body, the near-wake contains structures with two lobes; however, past $x \sim 2t$ the spatial features return to primarily single-lobed structures. It is suggested that these trends reflect the differences of the state of the trailing edge separated shear layer and this point is discussed in detail in §4.2. It should be noted that these features are different than the regular vortex shedding appearing in modes 1 – 6 for these two bodies. This difference is confirmed by the wavelengths of the vortices aligned on the wake centreline, which demonstrate that this is not an upper harmonic of the fundamental vortex shedding mechanism that dominates the wake of these two bodies.

The mean wake profile at $x = 2t$ is added to the plot of mode 2 for the square-edged body (Figure 4.8b) and to mode 8 for the bodies with circular and triangular edges (Figure 4.9b & d, respectively). Comparing these modes and the mean wake profile shows the influence of the outer lobes. The peak vorticity in these outer lobes coincides approximately with the location of maximum shear ($\partial\langle u\rangle/\partial y$) in the wake profile. Thus, the location of these outer lobes and the wake width appear interrelated and estimates of each are given in Table 4.4. The wake width, $y_{2\delta}$, is defined as the distance over which the flow is less than $0.95U_\infty$ and is measured herein at $x = 2t$. The location that is used for

Table 4.4. Wake width and location of outer lobes.

Edge shape	$y_{2\delta}/t$	b/t
Circular	1.76	0.55
Triangular	2.55	0.75
Square	2.95	0.86

the outer lobes, b, is measured from the wake centreline to the peak vorticity in the outer lobe occurring closest to the body, in the streamwise direction, for each body. The scales reported here appear to be related to the wake formation and are further discussed in §4.2.

4.1.7 *Reconstructed phase averages*

Although modes 7 & 8 of the circular- and triangular-edged bodies and modes 1 & 2 of the square-edged body are not identical, there exist similarities, as has been mentioned above. These similarities suggest that there is a common spatial feature that is relatively important to these elongated bluff bodies other than the primary trailing edge vortex shedding. By reconstructing individual instantaneous vorticity fields (see §4.1.3), using different linear combinations of modes, it is possible to determine the role of these modes (Diamessis et al., 2010). In order to ensure that the reconstructions were not limited to a unique instantaneous vorticity field, some form of ensemble average was desired. To this end, a phase average was performed based on the phase space of the a_1-a_2 plots. Each instantaneous snapshot has a specific angle, α, in this phase space defined as the arctangent of the ratio a_2/a_1. The phase average was performed by dividing this phase

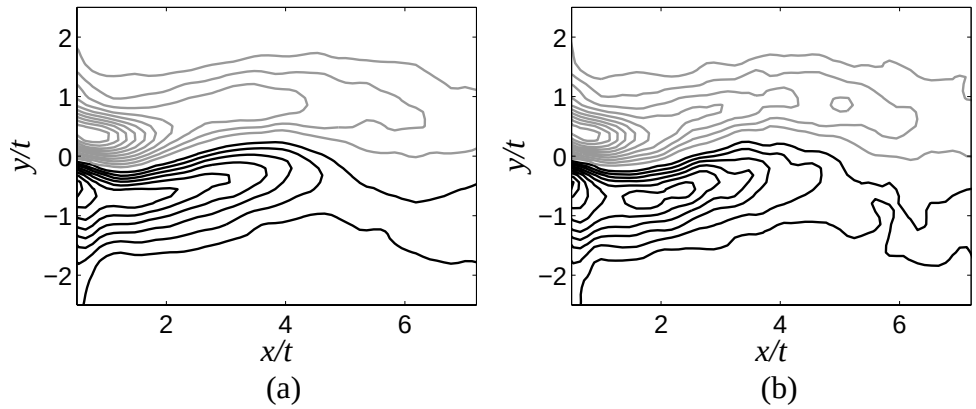

Figure 4.11. Phase $\alpha=5\pi/8$ of the wake of the square-edged body. (a) Ensemble average of reconstructed snapshots using modes 1 & 2, (b) Ensemble average of instantaneous vorticity from PIV. Contours: positive - black, negative - grey.

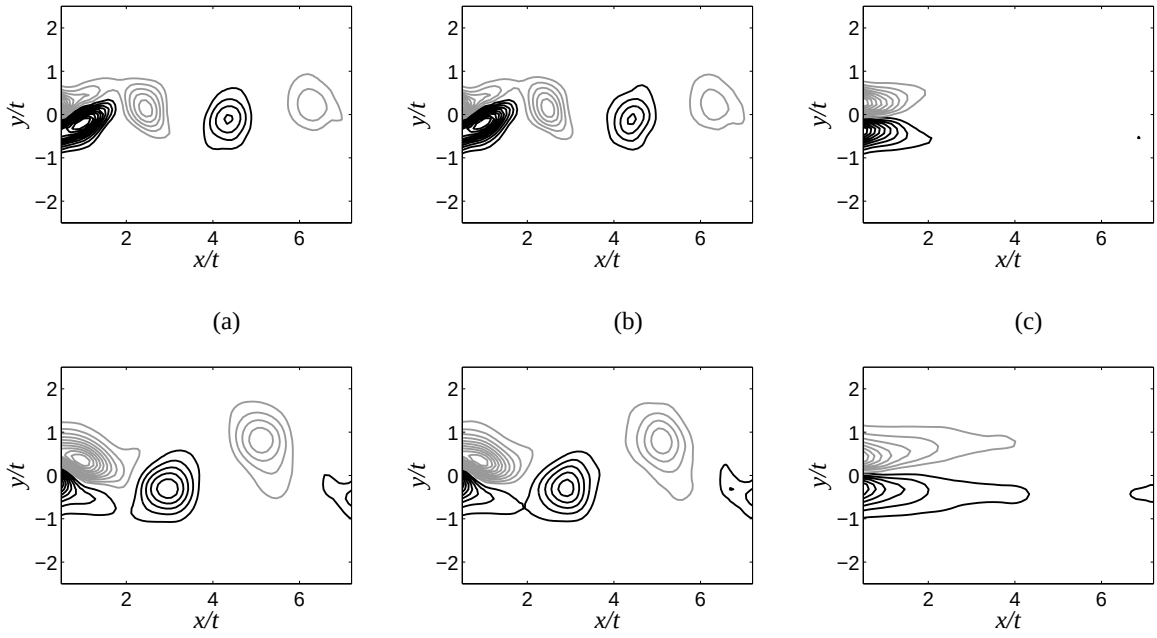

Figure 4.12. Phase $\alpha=5\pi/8$ of the wake of the circular- (top row) and triangular-edged (bottom row) bodies. (a) Ensemble average of reconstructed snapshots using modes 1-6, (b) Ensemble average of instantaneous vorticity from PIV, and (c) Ensemble average of reconstructed snapshots using modes 7 & 8. Contours: positive - black, negative - grey.

space into 16 bins from $0 < \alpha < 2\pi$. The instantaneous snapshots that fell into each bin were then reconstructed (using Eq. (4.3)) and an average taken of all of the reconstructions within the bin. Instantaneous vorticity fields computed directly from the PIV data were also ensemble averaged using the same bins; both of these ensemble averages are presented for the square-edged body in Figure 4.11. The reconstructed vorticity field shown in Figure 4.11a was based on modes 1 & 2 and it is shown that these two modes largely describe the ensemble averaged flow (Figure 4.11b).

The circular- and triangular-edged bodies are dominated by the vortex shedding modes (1 -6). A similar phase average to what was performed on the square-edged body is also performed on these bodies. However, instead of the two phase averages performed on the square-edged body, there are three different phase averages that have been computed. The first phase average is an ensemble of the reconstructed vorticity fields using modes 1-6 in the reconstruction. Therefore, it is analogous to the first phase average of the square-edged body in that it is performed by using the dominant flow features. The second phase average is similar to the one performed for the square-edged body and is

the ensemble of the instantaneous vorticity fields in each phase. The third phase average is an ensemble of the reconstructions using modes 7 & 8. The three phase averages are shown in Figure 4.12a-c and d-f for the circular- and triangular-edged bodies, respectively.

The results of Figure 4.12 suggest that the phase averaged flow is captured by the first 6 modes for both the circular- and triangular-edged bodies. However, the energy curves (see Figure 4.4b) show that modes 7 & 8 are also relevant. The reconstructed vorticity fields using this mode pair (Figure 4.12c & f) show similarities to the flow fields reconstructed using modes 1 & 2 for the square-edged body (Figure 4.11). Further discussion on this observation is given in the following section.

4.2 Discussion

4.2.1 *Existence of the separated shear layer mode*

The reconstructions using the dominant vortex shedding modes (1 - 6) for the circular- and triangular-edged bodies (Figure 4.12) show that it is these modes which dominate the wake structure. It is also evident that another important mode pair is present. As previously observed, mode pair 7 & 8 is not an upper harmonic of the fundamental shedding frequency but is a distinct mode pairing with a particular spatial arrangement. The alignment of the outer lobes with the maximum shear in the mean wake velocity profile suggests that this mode is related to the separated shear layers at the trailing edge. Reconstructing the vorticity field using this mode pairing for the circular- and triangular-edged bodies (Figure 4.12c & f, respectively) reveals that this mode pair represents a layer of high vorticity at the trailing edge of each body. The high shear ($\partial u/\partial y$) in separated shear layers leads to higher levels of vorticity which are observable through vorticity contours. Therefore, the vorticity contours in Figure 4.12c & f appear to indicate high shear. It is assumed that the high shear represents the separated shear layers of these bodies. The phase average of the reconstructed vorticity field for the square-edged body (Figure 4.11) using its similar mode pairing (1 & 2) demonstrates that this mode pair also describes the contribution of the separated shear layer, which is significantly larger. From this point onwards, these mode pairs: 7 & 8 for the triangular-

and circular-edged bodies, and 1 & 2 for the square-edged body, will be referred to as the "separated shear layer" modes. As well as basing this assertion on the reconstructed flow fields, Lardeau et al. (2010) have performed POD analysis on the flow fields resulting from mixing layers which show some similarities to these separated shear layer modes. The limitations in the comparison are due to the asymmetry of the mixing layer in contrast to the symmetry of the wakes measured herein; however, mirroring the results of Lardeau et al. (2010) across the streamwise axis reveals a similar spatial pattern to the separated shear layer mode. The decomposed modes of the mixing layer feature spatial structures with offset lobes which, when mirrored, are analogous to the three-lobed pattern observed in the separated shear layer modes herein (e.g., Figure 4.8).

Much of the work on bluff body wakes with regards to proper orthogonal decomposition has been focused on the circular cylinder (Deane et al., 1991; Ma and Karniadakis, 2002; Noack et al., 2003). From their examination of the circular cylinder, Noack et al. (2003) found that, as in the present case, the dominant modes arrive in pairs and that "...the *n*th pair approximately resolves the *n*th harmonics". From this work, and other published data (e.g., Ma and Karniadakis, 2002), it would appear that a separated shear layer mode is either not present or contains too little energy to play a significant role in describing the wake structure of a circular cylinder. However, it is well known that it is the interaction of the separated shear layers in the wake of circular cylinders which is responsible for the wake formation (Gerrard, 1966). It is not clear from the available literature why the decompositions do not contain such a mode. The work of Lardeau et al. (2010), on mixing layers, involves two different initial conditions which offer a plausible explanation. The first case is when there is a thick trailing edge that separates the two boundary layers that form the mixing layer, and the second case is when the trailing edge is thin. When comparing the decompositions of the two initial conditions, it is evident that when the trailing edge is thin, spatial features with significant energy appear further downstream than when the trailing edge is thicker. This scenario is analogous to the contrast between the wakes of the circular cylinder and the bodies tested herein. The separated shear layers from circular cylinders have been conceptualized as thin layers, or even as vortex sheets (Roshko, 1954a). The relatively thin size of shear layers separating from shorter bluff bodies may be a reason why they are spatially less energetic. It is

apparent that the shear layers, and their relative importance, are markedly different between elongated bluff bodies and the circular cylinder.

The persistence of a separated shear layer mode pairing with significant energy, especially when contrasted with the absence of such a mode pairing in the wake of a circular cylinder, leads to the suggestion of this mode being a general feature of elongated bluff body wakes. It appears from the data presented herein that each body is influenced to a differing degree by the separated shear layer. The dominance of this mode pairing for the square-edged body is reflected in it being the most energetic mode. Both the dominance of this type of mode and the significantly different fluctuating flow at the edge of the recirculation region (Figure 4.1) seem to be the result of the significant size of the trailing edge boundary layer. Castro and Epik (1998) performed experiments on an infinite plate with a blunt leading edge and found that it took 6.5 times the reattachment length for some of the Reynolds stresses to recover to values expected of a boundary layer with an equivalent thickness; furthermore, higher order statistics took an even longer distance to recover. Highlighting this observation, Parker and Welsh (1983) did not observe narrow banded peaks in the velocity spectra over the elongation ratios of $7.6 < c/t < 16$ for rectangular cylinders at similar Reynolds numbers. Since the criteria used herein for the definition of an elongated bluff body requires leading edge separation and subsequent reattachment, it is apparent that the boundary layers separating at the trailing edge will experience the effect of the leading edge separation over a wide range of geometries and elongation ratios. This likelihood has implications regarding the separated shear layer mode observed herein. Even a body with a relatively small leading edge reattachment length, in relation to its elongation ratio, such as the circular-edged body (Chapter 2), has a relatively energetic separated shear layer mode. This mode presents larger spatial features and increasing energetic importance as the leading edge separation angle grows. Thus, although a persistent presence, the separated shear layer mode varies in significance and the importance of its contribution to the overall wake structure is discussed in the following section. The POD performed in this chapter lends quantitative support to the notion of competition presented in Chapter 3. It was shown in Chapter 3 that as the leading edge separation angle grew, the trailing edge shedding became weaker and the overall flow became dominated by the energy content of the leading edge. The

energetic importance of the separated shear layer modes found for the three bodies herein agree with this mechanism suggested in Chapter 3.

4.2.2 *Importance of the separated shear layer mode*

The importance of the shear layers in describing the wake structure of elongated bluff bodies is addressed in its relation to the hypothesis of the so-called "diffusion length" by Gerrard (1966). Gerrard (1966) examined the effect of free stream turbulence on the wake formation of circular cylinders, which led to the suggestion of this second length scale. The first length scale was that of the recirculation region, which had been suggested earlier by Roshko (1954a). These two length scales were combined by Gerrard (1966) in an attempt to universalize the Strouhal number. The universalization of the Strouhal number remains elusive; however, the observed cause of this second scale by Gerrard (1966) is of interest in light of the present results. Gerrard (1966) observed that when free stream turbulence was introduced to the flow around a circular cylinder, the separated shear layers grew thicker. These thicker shear layers were then hypothesized to delay the interaction between the opposing shear layers in the recirculation region which, according to Gerrard (1966), was the cause of the lower Strouhal number measured in this case. The spatial scale of the separated shear layer mode described herein, in addition to its relative energy contribution, is assumed to be closely linked to the diffusion length described by Gerrard (1966). The present results show that the larger the spatial size of the separated shear layer mode (Table 4.4), the lower the shedding frequency.

The distinctions in shedding frequency were also discussed in Chapter 2 in terms of the overall momentum balance of the recirculation region and in Chapter 3 in terms of the competition between the magnitude of the pressure fluctuations at the leading and trailing edges, respectively. In Chapter 2, it was found that Reynolds shear stresses grew in importance for the momentum balance as the leading edge separation angle increased. The increase in the separation angle was also observed to increase both the boundary layer thickness and the level of Reynolds shear stresses contained in the trailing edge boundary layer. The distribution of fluctuating flow angles (see Figure 4.1) are taken along the separating streamline which, in the time-averaged sense, represents the division between the recirculation region and the separated trailing edge boundary layer. Thus,

this distribution can be thought to partially characterize the separated shear layer. The separated shear layer is the result of the interaction between the so-called "inner" flow and the "outer" flow, which distinguish the flow within the recirculation region and outside of it, respectively. The outer flow has the initial condition, upon trailing edge separation, of the trailing edge boundary layer. The inner flow is typified by trailing edge vortices growing alternatively. Thus, the separated shear layer modes observed herein and their relative significance represent this interaction. The square-edged body has the most significant separated shear layer modes and, according to Figure 4.1, have a significant probability of fluctuating flow aligned across the boundary of the recirculation region. The relatively high likelihood of these fluctuating flow angles shows the dominance of the outer flow. The circular-edged body, however, has fluctuating flow aligned with the separated streamline. This body also has the energetically least significant separated shear layer mode. Thus, it is suggested that as the outer flow becomes more dominant, the separated shear layer modes become more dominant in the description of the wake structure.

The interplay between the trailing edge boundary layer and the growth of trailing edge vortices has practical application as well. One of the implications of the diffusion length, suggested by Gerrard (1966), relates to the circulation present in the shed trailing edge vortices. He reasoned that because it takes longer for the separated shear layers to interact when the diffusion length is increased, that less vorticity is cancelled by the opposing shear layer and as a result, the circulation in the shed vortices is increased. It was reported in Chapter 4 that the circulation of the vortices in the wake of the triangular-edged body was higher than for the circular-edged body even though the shedding frequency was higher for the latter. Presently, it is observed that the magnitudes of the lift fluctuations, which correlate strongly with circulation, are also higher for the triangular-edged body than for that of the circular-edged body. The more energetic and defined presence of the separated shear layer mode for the triangular-edged body is assumed to indicate stronger influence of the trailing edge boundary layer on the formation of the wake structure. This influence is shown to affect the loading on the body through the lift fluctuations. These results agree well with the mechanism of competition presented in Chapter 3 as well. It was shown therein that the flow became increasingly dominated by the leading edge as

the trailing edge vortex shedding strength was diminished by the magnitude of the pressure fluctuations at the leading edge.

At present, the relationship between the relative importance of the separated shear layer mode and the drag on the body is unclear. However, it is known that vortex shedding increases the overall drag of bluff bodies. Pastoor et al. (2008) achieved drag reductions by disrupting vortex formation through active manipulation of the separated shear layers. Thus, the presence of the separated shear layer mode will affect the overall drag force through passive manipulation of the separated shear layers; however, the extent of this effect remains the topic of future investigation.

4.3 Conclusions

The three symmetric bluff bodies studied herein represent a broad sampling of elongated bluff bodies. The square-edged body is governed by the leading edge vortex shedding whereas the circular-edged body is dominated by trailing edge vortex shedding. The triangular-edged body lies between these two extremes. The variety of the leading edge shapes allow for differing effects of the leading edge flow and the variety of trailing edges ensures that any generalities were not a manifestation of a particular geometry at this location.

A general feature of the three bodies tested was found and termed the separated shear layer mode. This mode was found by applying POD to the vorticity computed from PIV measurements. It was found to be the most energetic for the square-edged body followed by the triangular- and circular-edged bodies. This trend is matched with the separation angle and was suggested to reflect the dominance of the leading edge flow. The first six modes, or first three mode pairings, for the circular- and triangular-edged bodies were shown to be qualitatively similar to previously published decompositions of circular cylinders at low Reynolds numbers. The orbits found in the phase spaces of these bodies also agree with previous data; however, the square-edged body was shown to be markedly different.

The presence of the separated shear layer mode is suggested to be due to the interaction

of the trailing edge boundary layer (the "outer" flow) and the growing, trailing edge vortices in the recirculation region (the "inner" flow). The data shown herein support this notion and confirm the results presented in Chapter 3. The interaction between these two flows was shown to be manifest in the distribution of the fluctuating flow at the edge of the recirculation region. The square-edged body, which is dominated by the separated shear layer mode, had a significant probability of fluctuating flow aligned vertically across the recirculation region. The triangular-edged body had the second most energetic separated shear layer mode and appears to be between the square- and circular-edged bodies in terms of the fluctuating flow angle.

In relation to the shedding frequencies observed, it was hypothesized that the separated shear layer mode is linked with the diffusion length idea of Gerrard (1996). It was shown that when the scale of the separated shear layer increased, the same effects were observed as when the so-called diffusion length was increased – nominally higher lift fluctuations and lower shedding frequencies. The square-edged body, being dominated by the separated shear layer mode, did not follow these trends as its shedding does not appear to be regularly periodic (Chapter 2).

The general feature of elongated bluff bodies identified herein is assumed to be related to the competition between energetic magnitudes suggested by Chapter 3. For the square-edged body there was no regular Kármán shedding and thus no modes representing this feature. In Chapter 3 it was shown that the square-edged body was dominated by the leading edge separating-reattaching flow. However, the notion of a continuous exchange shown in Chapter 3 suggests that there could be a flow scenario where the Kármán shedding modes and the separated shear layer mode are of relatively equal energetic importance in the POD. This idea remains the topic of future investigations.

Conclusion to Part I

Throughout Part I, several data have been presented and several observations drawn – each chapter containing its own set of conclusions. However, in this section, these individual conclusions are synthesized to form a deeper understanding of the phenomena of elongated bluff body flows than any individual conclusion reached on its own. In Chapter 2, a thorough examination was performed on the recirculation region. For circular cylinders this is where all of the essential dynamics of wake formation occur (Gerrard, 1966). Roshko (1954b) suggested the importance of the pressure field created by the growing vortices to "close" the mean recirculation region. This importance was later reinforced by Balachandar et al. (1997) by using the quantitative method of a force balance on the recirculation region. Herein, it was found that while the pressure field was still important for closing the mean recirculation region of a trailing edge vortex shedding dominated body, that for bodies with significant leading edge flow separation the shear stresses at the boundary of the recirculation region become increasingly important. The shown importance of the turbulent stresses reveals the importance of the leading edge flow to the overall process. Due to the heightened stresses in the trailing edge boundary layers there are enhanced momentum transfers at the edge of the recirculation region. For a circular cylinder, the "outer" flow is typically the free stream flow which even close to the cylinder is relatively quiescent. Thus, the introduction of the significant disturbance of separating-reattaching flow at the leading edge (Castro and Epik, 1998) is shown to significantly alter the dynamics of the recirculation region.

Within the recirculation region, the vortices were also characterized in Chapter 2. The circular-edged body had vortex paths and convection speeds much like that of shorter bluff bodies since the influence of the leading edge flow was comparatively low. However, for the triangular- and square-edged bodies, the growth of trailing edge vortices was observed to be disrupted. It was shown that vortices were smaller, traveled slower and did not penetrate as far into the recirculation region as those of the circular-edged body and for the circular cylinder data of Balachandar et al. (1997). These results were hypothesized to occur by Gerrard (1966) in the case of circular cylinders when the vortex shedding was hampered by increasing disturbances in the separated shear layers. Based

on the dynamics observed in the recirculation region in Chapter 2 it is expected that these vortex data reflect the interference of the flow from the leading edge.

To better address the balance between elongated bodies which are leading edge dominated and those which are trailing edge dominated models with varying leading edge separation angles were studied in Chapter 3. Contrary to what is expected for similar geometries at low Reynolds numbers, it was observed that synchronization between the leading edge separation and the trailing edge vortex shedding was not important. Rather, it was suggested that as the leading edge separation became larger, that it began to dominate the trailing edge vortex shedding. The strength and periodicity of the trailing edge vortex shedding was shown to continually decrease as the leading edge separation angle grew. Along with this observation, the shedding frequency was shown to continually decrease with increasing separation angle. Although not enough of the parameter space was sampled (e.g., more elongation ratios), it is suggested that there is some connection between these two observations. Gerrard (1966) studied the effects of free stream turbulence on the shedding frequency of circular cylinders. He suggested that as the interaction within the recirculation region becomes more difficult the shedding frequency must decrease. In the present work, as the separation angle grows there are increasingly large vortices shed from the leading edge. It was also observed that there is a marked drop in the spanwise correlation as the leading edge separation angle increases. The combination of both of these observations suggest that the interaction in the recirculation region will be disturbed thus, following Gerrard (1966), possibly lowering the shedding frequency. The lack of importance of the synchronization meant that there was a relatively continuous change in the behaviour of the shedding as the leading edge separation angle grew. The ratio between the fluctuating pressure close to leading edge reattachment and that in the recirculation region was shown to be a reasonable indicator of bodies which were trailing edge or leading edge dominated. These data approximate the fluctuating energy at each location – a notion which was explored further using the proper orthogonal decomposition technique in Chapter 4.

The analysis of the wake data using POD shows the features of the flow which are energetically most important. It was suggested in Chapter 4 that there exists a mode

called the separated shear layer mode. As the name implies, this mode represents the contribution of the separated shear layer to the wake. The observations regarding the energetic content of these modes agree well with the leading edge and trailing edge domination categorization of Chapter 3. The square-edged body was shown to be dominated by this mode. For the circular-edged body, with small leading edge separation, the separated shear layer mode was not very energetic and the triangular-edged body was between these other two bodies. It was suggested that this mode increases in importance as the leading edge separation begins to dominate wake formation.

The overall mechanism of vortex shedding of elongated bluff bodies is shown herein to be strongly related to the leading edge geometry. The state of the trailing edge boundary layer, which is significantly influenced by the leading edge geometry, was observed to be the most significant factor in the determination of the dynamics in the recirculation region in Chapter 2. In Chapter 3, the leading edge geometry was shown to be strongly linked with the three-dimensionality of the trailing edge flow. It was also shown that as the leading edge separation angle increased that the trailing edge vortex shedding became noticeably weaker. The discovery of the separated shear layer mode in Chapter 4 revealed the energetic balance between the leading edge flow and the trailing edge vortex shedding. Therein, it was shown that the trailing edge vortex shedding modes are eventually suppressed at high leading edge separation angles. In all cases, as the trailing edge vortex shedding was weakened, the shedding frequency was also observed to decrease.

The results herein offer a framework going forward for the study of vortex-induced vibrations of long span suspension bridges. The variation of the shedding frequency was shown to vary approximately with the size of the leading edge separation. It was observed that for a larger region of leading edge separation that there was a lower shedding frequency. The lower shedding frequency is suggested to be the result of disruptions to the trailing edge vortex shedding process. Thus, in the design of these bridges, one can begin to understand how a change to the cross-sectional geometry affects the shedding frequency as well as the regularity of the trailing edge vortex

shedding. A note of caution, however, need also be applied to the observed results. All of the data obtained herein are for static models which provide a good starting point for a more thorough examination of dynamically mounted bodies. However, the literature (e.g., Parker and Welsh, 1983; Mills et al., 2002) show how susceptible the leading edge vortices are to external forcing. Thus, once these bodies are mounted dynamically, it is possible that the motion of the body can excite the ILEV instability which is suppressed for static bodies at higher Reynolds numbers (Nakamura and Nakashima, 1986). The work herein provides a mechanistic framework incorporating dynamics of the leading edge separation, trailing edge boundary layers, recirculation region and the wake around which future studies of dynamically mounted sections can be contextualized.

Part II Development of long-duration PIV and the study of flutter

Introduction to Part II

It is well known that bluff body flutter caused the collapse of the Tacoma Narrows Bridge (Billah and Scanlan, 1991). Since that time, bridges are routinely tested for their susceptibility to flutter based primarily on section model wind tunnel tests using various approaches (e.g., Scanlan and Tomko, 1971; King, 2003). For example, the wind tunnel methods proposed by Scanlan (Scanlan and Sabsevari, 1969) are based on the potential flow model of Theodorsen (1935). Theodorsen found that the onset of coupled flutter for airfoils could be predicted using a potential flow model. Obviously, bridge sections represent a significant departure from smooth airfoils; however, Scanlan was able to show that parallels exist between the two flows. Primarily he found that the derivatives of the aerodynamic coefficients from the potential flow model can be replaced with what are commonly called the "flutter derivatives" derived from section model tests. This method is still one basis for wind tunnel testing with recent research focused on more accurately determining the flutter derivatives from freely vibrating section models (e.g., Bartoli et al., 2009).

Even though the flutter instability can now be prevented based on wind tunnel testing, there remains relatively little known about the flow dynamics. In both Chapter 6 and Chapter 7, investigations into the wake during this instability reveal new features of the flow. One of the common interpretations of the flutter instability relies on the vortex drift hypothesis given by Larsen (2000). In order to study the vortex kinematics in the wake, a novel PIV system was developed. In Chapter 6, the development of the PIV system used for this study is given in detail. The time-resolved system used herein represents the current state-of-the-art due to its unique recording length. The introduction of a long recording length allows for the capture of the low frequency oscillations of flutter as well as the high frequency turbulence content in the wake.

In the current work, a rectangular cylinder with an elongation ratio of 7 is examined using a conventional section model rig. There has been some work done on flutter of rectangular cylinders and the results are comparable with those of the classic 'H' shaped cross-section of the Tacoma Narrows Bridge. Matsumoto et al. (1997) showed that the

torsional flutter derivative, A_2^*, for rectangular cylinders around this elongation ratio varies in a similar manner to an H-section (as shown by Scanlan and Tomko, 1971). The similarity is that the value of the flutter derivative is positive over a wide range of velocities. This positive value indicates that the aerodynamic damping is negative and will create a negatively damped overall system once the structural damping is exceeded.

Chapter 5

Details of experiments

5.1 Wind tunnel tests

The flutter tests were carried out in an open-return aerodynamic wind tunnel with a 7.4:1 contraction ratio at the Boundary Layer Wind Tunnel Laboratory (BLWTL) of the University of Western Ontario. The air is pulled through a honeycomb and several fine screens to straighten the flow before it enters the 0.46 m x 0.46 m cross-section test section which has a length of 1.5 m. The wind tunnel has been described in some detail by Bailey (2001).

The co-ordinate system used in these studies is located at the centre of the static trailing edge. This is defined as a laboratory co-ordinate system in the sense that it does not change with body motion. All geometry is scaled by the thickness, t, of the model. This choice agrees with conventions used previously in related works in scaling the Reynolds number (e.g., Parker and Welsh, 1983). Since only a single chord-to-thickness ratio is studied in the current work, no implications pertaining to flow similarity are intended by this choice.

5.1.1 *Build-up of flutter*

The first examination of the flutter instability was performed by slowly increasing the free stream speed. The speed was set below the onset of flutter and increased slowly until the oscillations were too great for the mechanical section model system. The free stream speed, U_∞, was increased by hand to limit the rapid growth of the body motion. Although done by hand, the wind tunnel speed was observed to increase monotonically (refer to Figure 6.3) between 14.5 and 17 m/s and the Reynolds number based on the free stream speed and the model thickness (19 mm) ranged from 1.76-2.2x10^4. The results presented herein focus on the build-up process of the flutter phenomena of the elongated body. The flutter phenomenon was characterized through the temporally and spatially resolved velocity measurements taken in the wake throughout the build-up process.

5.1.2 *Flutter at steady free stream speeds*

To observe vortex patterns in the wake of a body experiencing the flutter instability, it was necessary to obtain statistically stationary data by setting the free stream of the wind tunnel. The speed of the wind tunnel was set, the model allowed to achieve stable oscillations and the data were subsequently sampled. For the displacement measurements and fixed point hot-wire data, the experiment was performed at reduced wind speeds ranging from 35 to 50 with 11 observations. The non-dimensional reduced wind speed is given by $U_r = U_\infty/f_t t$, U_∞, is the free stream velocity, t is the thickness of the cylinder and f_t is the natural frequency (in still air) in torsion. The reduced wind speed was increased by approximately 1.4 between each observation.

There were two PIV measurements performed in the wake at $U_r = 42$ and 50 and another set of data taken under the body at $U_r = 50$. The size of the frame in the wake extended nearly one chord length into the wake and included the entire thickness of the wake (for even the most violent vibrations) which meant the frame size in the wake was approximately 6.7t x 6.7t centred vertically close to $y/t = 0$. The PIV setup is depicted in Figure 5.1.

5.2 Dynamic testing set-up

A model rectangular cylinder with an elongation ratio (c/t) of 7:1 was constructed of

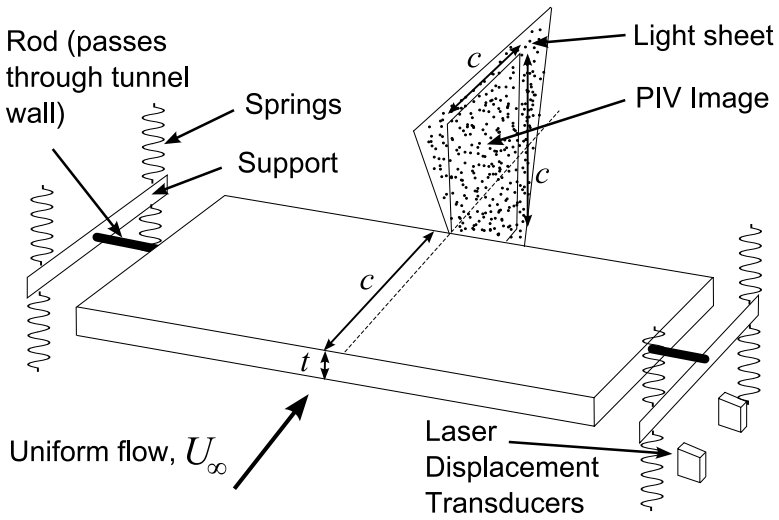

Figure 5.1. Schematic of the experimental set-up.

aluminum and balsa wood. The model had a span-to-thickness ratio of 24. An aluminum frame was used to provide strength in bending so that the model would act as a rigid body. Foam was then used to shape the model which was clad in balsa wood. The model was suspended on either side by springs mounted to a support beam of sufficient stiffness. A schematic of the experimental set-up is shown in Figure 5.1 while the dynamic and static properties of the model combined with its supporting structure are given in Table 5.1. In still air, the spring-model assembly had natural frequencies of 11.1 Hz and 16.1 Hz in the vertical and torsional modes respectively. The blockage ratio for all experiments was approximately 5% and no measures were taken to account for this blockage.

5.3 Displacements and point velocity measurements

Displacements were measured using two laser displacement transducers on either side of the central axis of the model. In addition, a pair was used on the other side of the testing rig to ensure that there was minimal difference between the displacements on either side. Matsushita Electric Works LM10-130 Class 2 transducers were used. These sensors offer a range of ±50 mm with a resolution of 20 μm.

Point velocity measurements were made in the wake using a Dantec 55P011 single-wire connected to a Dantec 90N10 constant temperature anemometer. These velocity measurements were made in conjunction with the displacement measurements. However, the hot-wire measurements could not be made while performing PIV since the oil used to seed the flow would have damaged the probe.

Table 5.1. Mechanical Properties of Experimental Set-up

Parameter	Value	Unit
Chord	133	mm
Thickness	19	mm
Span	458	mm
Mass per unit length	0.638	g/mm
Mass moment of inertia per unit length	1380	g-mm²/mm
Vertical frequency	11.1	Hz
Torsional frequency	16.1	Hz
Mechanical damping ratio (in still air)	1.4	% critical

5.4 Particle Image Velocimetry

The PIV data were obtained using a long duration, time-resolved system (Chapter 6). The images were acquired using CMOS cameras with a resolution of 1024 pixels x1024 pixels. These images were acquired at 1 kHz, yielding PIV image pairs at a sampling frequency of 500 Hz. Seeding for the PIV system was provided via a Laskin nozzle. Olive oil was used as the liquid to be atomized which provides a mean particle diameter of 1 μm when used with a Laskin nozzle (Echols and Young, 1963). The particles were illuminated from below by a Quantronix Darwin-Duo laser operating at 500 Hz and synchronized with the image captures. The energy of the laser was 22 mJ/pulse in each frame.

Cross-correlation of the images was performed using 32 pixels x 32 pixels interrogation windows with a 50% overlap. Filtering and smoothing of the data were performed in order to eliminate erroneous vectors. The number of vectors which were removed, and then interpolated, was approximately 5% in each frame.

The time, Δt, between the images in a straddle pair was determined in order to yield pixel displacements of approximately 8 in the free stream for each of the experiments performed (ranging between 65 – 80 μs).

Chapter 6

Long duration, time-resolved PIV to study unsteady aerodynamics*

There are many examples in engineering practice and nature where fluid flows are both turbulent and unsteady in the time-averaged sense. Two natural examples of these cases are oceanic flows, where turbulence is modulated by waves and tides, and avian aerodynamics where turbulent flow exists simultaneously with the unsteady vortices generated by flapping wings. Among engineering applications, one of the most famous engineering disasters – the Tacoma Narrows Bridge collapse – is an example of these types of flow conditions as it failed due to bluff body flutter. The current state-of-the-art techniques are not suitable for measuring these phenomena due to the lack of either temporal/spatial resolution or the lack of long time recording capabilities.

Bluff body flutter has been a persistent problem for bridge engineers. As previously noted, the most well known case of bluff body flutter is the collapse of the Tacoma Narrows Bridge. Although often interpreted as resonance between alternating vortices in the wake, it has been shown definitively that it was flutter that caused the bridge to collapse (Billah and Scanlan, 1991). This distinction is important because the vortices being shed from the body, as well as the turbulence created by the unsteady flow around the body, have time scales much shorter than that of the oscillating bridge. Since the engineering community witnessed this catastrophic failure, steps have been taken to understand and prevent this instability. Currently, an experimental method similar to that developed by Scanlan is required to gauge a given bridge's stability (Scanlan and Tomko, 1971). This section model technique has been used in wind engineering for every long-span bridge in the last 40 years and is still used today at the Boundary Layer Wind Tunnel Laboratory (BLWTL) of the University of Western Ontario and other leading

---

* A version of this chapter has been published in the IEEE Transactions on Instrumentation and Measurement. The full reference is cited herein as Taylor et al., 2010a. Copyright release information can be found in Appendix A.

facilities. However, due to the lack of experimental tools, the understanding of this instability is still quite limited. Over the years many researchers have looked at this instability by surface pressure measurements and structural responses (e.g., Matsumoto et al., 1997). However, with the large amplitude of body motions it becomes difficult to extract information about the flow from surface pressure measurements as the motion induced pressure field dominates and structural responses give no information about features of the flow.

With the advent of Particle Image Velocimetry (PIV) it became possible to learn more about flow fields such as these. PIV has been an established technique in the fluid mechanics community for some time (e.g., Keane and Adrian, 1990), but has seen little use in wind engineering. Work has been done on the near wake during this instability using classical (no time resolution) PIV techniques (Taylor et al., 2007). Even with time-resolved PIV, however, it would be impossible to measure the build-up of flutter from incipient motion to motions of large amplitude. Thus, a new PIV system has been developed at the University of Western Ontario which allows for resolution in time, paired with the capability of long recording periods. This novel system will be used to measure various problems in unsteady aerodynamics and hydrodynamics.

Typical in unsteady aerodynamics and hydrodynamics is some low frequency component significant to the flow (such as the flapping of wings or a bluff body oscillating) as well as the higher frequencies associated with turbulent fluid motion. This streaming, time-resolved PIV (STR-PIV) system has the unique ability to capture many cycles of the low frequency features as well as the necessary time resolution to quantify the high frequency turbulent activity.

An effort has also been put into developing open source software built on C++ using the Qt platform for the interface. The software was developed with the specifications of this new STR-PIV system in mind and has proven to provide high speed cross-correlations necessary for the enormous task of processing the data yield of this system. The software is based on the open source URAPIV code (Gurka et al., 1999). Although cross-correlation algorithms for PIV analysis widely exist and are well established (see PIV

challenge (Stanislas et al., 2005) and such open source codes as GPIV, MATPIV), there is a need for a fast, simple, accurate and reliable algorithm to resolve the velocity fields for massive data capacities. As computer memory, the speed and quality of cameras, and laser power continue to increase, so too does the sampling frequency and record length of PIV data.

The advantage for PIV over other experimental methods in fluid mechanics is the spatial resolution offered by the technique. Hot-Wire Anemometry and Laser Doppler Velocimetry provide only single point velocity measurements but offer much better temporal resolution than PIV. Modifications to the PIV method are most frequently developed to increase accuracy and/or resolution in time and/or space (e.g., Ponte et al., 2004). However, the method has also been used for experiments with unique imaging methods (Li et al., 2008). Early attempts at time resolved PIV (TR-PIV) were performed with film (Williams et al., 2003) because of the inability of digital cameras to capture and stream these data let alone a computer with the required acquisition capability. Thus, time resolved data were not easily obtainable using PIV until relatively recently. There have been many TR-PIV systems used recently (e.g. Troolin et al., 2006; Wernet, 2007; Hubel et al., 2009); however, these have always been for relatively short recording periods.

In most forms of TR-PIV, the images are stored to random access memory on the camera (e.g. Troolin et al., 2006). Although providing some storage capacity, the amount of RAM possible is still limited, being on the order of 8 GB. Thus, for images that are 1 megapixel in size, supposing the entire memory can be used, the user is limited to 8000 images (or 4000 image pairs). Capturing images at a rate of 1000 Hz means that only 8 seconds of data can be collected. Working in a cross-correlation mode will result with 4000 vector maps, which for the present case, is not statistically sufficient. Moreover, if the experiment has low frequency components or phase averaging has to be performed – as is the case with experiments on flow across flapping wings, oceanic flows, internal combustion, etc. – then these sampling times are too short.

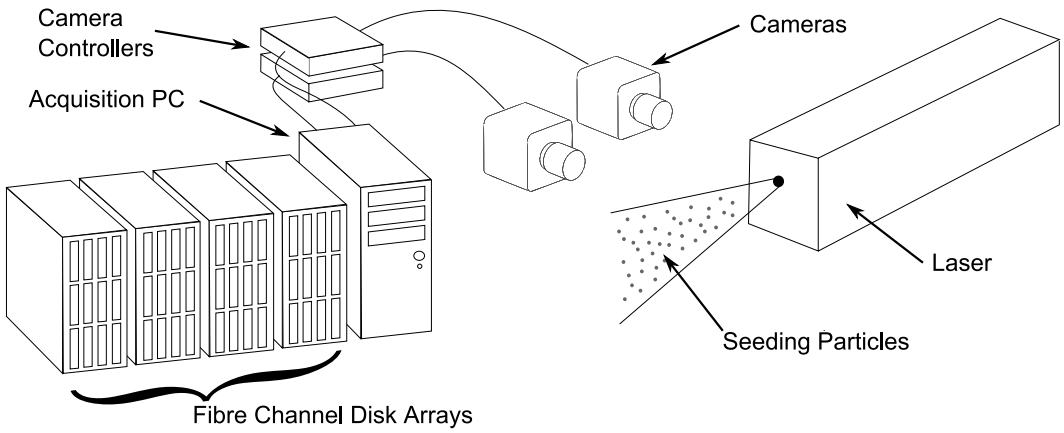

Figure 6.1. Schematic of the streaming, time-resolved PIV system and its components.

6.1 System details

The system described herein is different from the so-called TR-PIV (as reviewed in the Introduction) due to the capability of continuous streaming PIV images at a comparably high frame rate for long time durations (see Figure 6.1). In this manuscript, the results are based on PIV experiments using a single camera (1024x1024 pixels² at 1000 fps) with a record length of 50 seconds which is well short of capacity.

6.1.1 *Imaging and acquisition*

The imaging is performed using a Photron FASTCAM-1024PCI CMOS camera. This camera is capable of streaming the images continuously to a PC at a rate of 1000 Hz with a spatial resolution of 1024 x 1024 pixels and a 10 bit dynamic range. The technological challenge that emerges from the high-speed capability of the cameras is streaming and storing this amount of data for long durations. The solution is provided by using two unique video cards (IO Industries Inc.); each of these cards stream the images at a data rate of 650 MB/sec into two sets of fiber-channel hard drive arrays (Figure 6.1). Since the storage space is not RAM based, it is limited only by the capacity of the fiber-channel disc array. Although only one camera is used herein, the disk arrays of the system are of sufficient size to allow for acquisition of 1 megapixel images for 23 minutes from each of two CMOS cameras at 1000 Hz (i.e., in the presented set-up it can acquire 1,380,000 images continuously from each camera). The recording system is also capable of two-camera stereoscopic PIV and upcoming results will be the subject of future publication.

The spatial resolution of the system is similar to other CMOS based PIV systems. The minimum and maximum resolutions are dependent on the seeding and fluid medium being measured; however, in the current experimental setup the spatial resolution is 130 μm/pixel.

6.1.2 *Illumination*

Illumination is provided by a double head, diode pumped, Q-switched, Nd:YLF laser. The specific model of the laser is the Darwin-Duo by Quantronix. The lasers yield pulsed laser beams with a wavelength of 527 nm, providing power of 80 W at 3000 Hz. For PIV measurements, however, it is desirable to separate the timing of the emissions of the two laser heads. This separation means that instead of having a beam energy of 45 mJ/pulse (as it operates normally), in PIV mode there is only 22.5 mJ/pulse of energy available to illuminate the particles.

The particles used in this study are created by atomizing olive oil. These particles have a physical size of approximately 1 μm in diameter (Echols and Young, 1963). However, for PIV it is the image size, in pixels, of the particles that determines the accuracy of the technique (Raffel et al., 1998). This image size is a combination of several parameters including light sheet intensity, physical particle size, sensitivity of the pixel array, etc. In this study it is found that the particle images have pixel diameters of approximately 1-2 pixels. Results from Monte Carlo simulations in (Raffel et al., 1998) show an optimal particle image diameter of 2 pixels. However, as particle image diameters shrink below this value there is risk of increased peak locking effects. With conventional cross-correlation schemes there is always some effect of peak locking but from histograms of the present data (not shown) it appears that the peak locking effect is minimal. Although not employed herein, more advanced methods of correlation have been shown to nearly remove this effect (Chen and Katz, 2005).

6.1.3 *Synchronization*

In order to perform classical frame-straddled PIV to obtain images for cross-correlation, the camera and the laser have to be synchronized. The high frame rate, combined with a short time delay between PIV images enables the measurements of the time evolution in

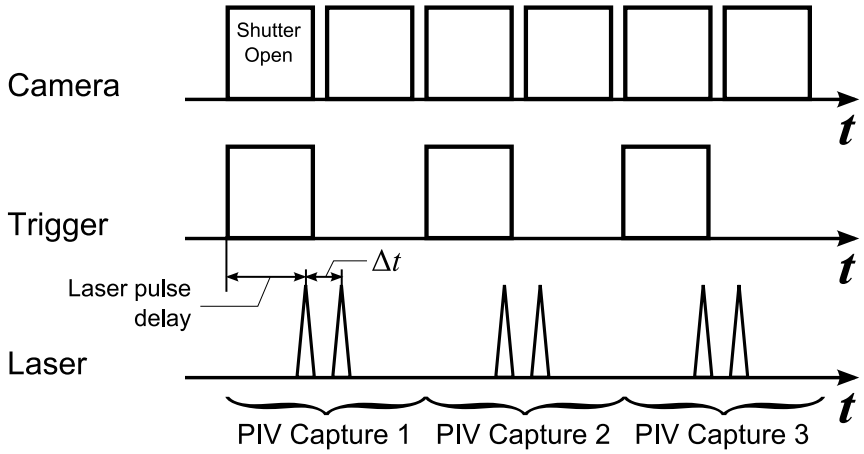

Figure 6.2. Illustrative synchronization scheme of the STR-PIV system.

high-speed flows. An illustrative synchronization scheme is presented in Figure 6.2.

The slowest component (camera or laser) determines the minimum sampling interval. In this manuscript, the sampling interval is equal to 0.002 sec (500 Hz) between PIV image pairs. Since the cameras cannot operate at full resolution faster than 1000 Hz these are the limiting features of the system. By maintaining the maximum data transfer rate of 1.3 GB/sec, these cameras can operate at faster speeds if resolution is reduced. For example if a resolution of 512 x 512 is used then the speed can be increased to 4 kHz. The time between the laser pulses, Δt, is chosen based on the free stream velocity in the investigated flow to optimize particle image displacements for the computation of the cross-correlation. This timing parameter is limited by the shortest time interval between two consecutive frames of the camera which has been measured to be approximately 5 μs. For the current experiments the value for Δt was chosen to be 50 μs. With a range of velocities required during the single build-up experiment, this value was a compromise between the ideal values at low- and high-speed flows.

The laser pulse delay is determined in order to ensure that a single laser pulse ends up in each frame of the image pairs. If not determined correctly a single image will contain two laser pulses. To make this parameter easier to set, the shutter stays open the maximum amount of time. The experiments then are performed in relative darkness and the only light absorbed by the CMOS sensor is a function of the laser pulse duration and

its energy (in this case 22.5 mJ/pulse with a pulse duration of 200 ns).

The synchronization is made possible through the use of a TSI LASERPULSE synchronizer (model 6100035) and its capacity for external triggering. The synchronizer has 1 ns resolution and its design for PIV systems makes it ideal for the current system as well as the ease of use of the provided software. However, it is expected that an externally triggered signal generator could be substituted since the entire system is triggered off of the camera signal. As part of the solutions provided by IO Industries, the user is able to mask any number of the 3.3 V triggering signals from each camera. Thus, for PIV operation every second signal is masked so that the synchronizer receives a trigger only at the start of a "PIV cycle" (Figure 6.2). When operating in stereo or dual-camera mode the process is triggered off of a single camera while the two cameras are synchronized with each other.

6.1.4 *Software solution*

In order to deduce the velocity fields from the acquired images, a cross-correlation algorithm is applied (see Adrian, 1991 for more detail). The function of this procedure is to extract the average displacement of several particles statistically in a given interrogation window, followed by the division of the displacement with the known time interval, Δt, between two consecutive images. This division yields an average velocity value in two dimensions with two components at the centre of the chosen interrogation window.

For experiments performed on flow phenomena that have more than one time scale, such as the one described in this manuscript or other cases like oceanic flows or animal aerodynamics/hydrodynamics, it is essential to acquire long time data sets. These data sets require high temporal and spatial resolution to resolve the various scales of the flow. In addition, the statistical analysis – which is essential to describe turbulent aspects within the flow – requires a large sampling period to ensure convergence of the data. There are also examples, such as the flow cycles in oceanic flows, when wave cycles have to be sampled long enough to characterize the wave contribution and contamination in the investigated flow. Most of the available software packages today do not address

Table 6.1. Comparison of URAPIV-C++ and TSI's Insight 3G per Image Pair

Processor	Software	Operating System	Process type	Time (s)
Intel Core 2 Duo T7500, 2.2 GHz	URAPIV-C++	Linux	Correlation	2.49
	URAPIV-C++	Windows	Correlation	2.93
	Insight 3G	Windows	Correlation	4.45
	URAPIV-C++	Linux	Corr. + Filter	2.82
	URAPIV-C++	Windows	Corr. + Filter	3.01
	Insight 3G	Windows	Corr. + Filter	7.36

the problem of extremely large data sets and usually the input would be limited to a few thousand image pairs. In addition, once analysis is being performed, there are significant concerns of computational resources as typical data sets can take several weeks to compute on a single processor. The solution described in this manuscript uses URAPIV (Gurka et al., 1999), which is a well known PIV algorithm, redesigned and written in C++ using the Qt4 graphical user interface platform. The URAPIV algorithm was written originally in Matlab and later a Python version was added. It is widely used and it is completely open source and the group of programs is now known as OpenPIV (Liberzon et al., 2009). The idea behind it was to allow a simple and accurate cross correlation analysis which will provide a velocity vector deduced from a chosen interrogation window using FFT functions and statistical tools to validate the vectors (such as mean, standard deviation, median, etc.). The software has been tested and validated by comparison with known databases (e.g., Stanislas et al., 2005 and Okamoto et al., 2000). The accuracy has been shown to match that of commercial software (TSI's Insight) which uses similar algorithms in Gurka et al. (1999) and Liberzon et al. (2001). The use of standard cross-correlation techniques yields errors on the order of 0.1 pixels in carefully set-up PIV (Huang et al., 1997). The need to perform these tasks in substantially shorter times with large data sets requires the use of a non-scripted based programming platform such as C++. The C++ version utilizes the Matlab/Python algorithms in a more efficient manner and enables faster computation although some user friendliness is lost from the scripted languages.

The new URAPIV-C++ code takes advantage of the cross-platform capabilities of both the Qt libraries (Nokia Corporation , 2009) and the FFTW library (Frigo and Johnson,

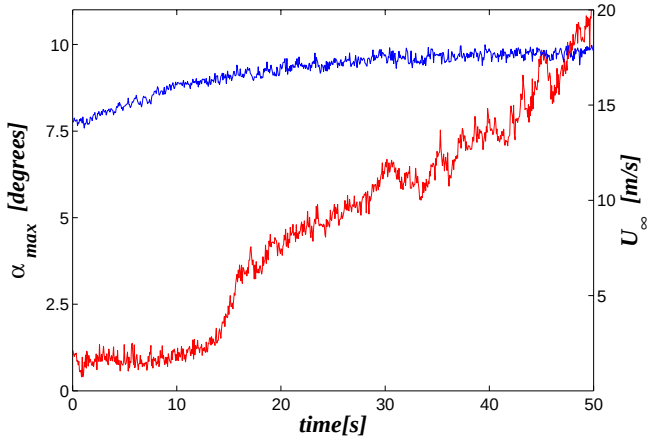

Figure 6.3. Maxima of periodic angular displacement, $\alpha_{max,}$ (axis on left, red line) and free stream speed, U_{∞}, (axis on right, blue line) with increasing time (in seconds).

2009). Unlike some other open source PIV codes, URAPIV-C++ uses only these two libraries which make it easier for users to both use and develop the software. As noted, a substantial increase in speed is observed between this version and the scripted versions (Matlab/Python) of the same routines; however, slight increases have also been observed over some of the commercially available software packages on a single processing core (see Table 6.1). Although currently written for a single processor, the goal for future versions of the code is to allow for distributed computing in order to take advantage of one's available computational resources.

6.2 Results and discussion

6.2.1 *Body motion*

The PIV system sampled the wake for 50 seconds continuously, yielding 25 000 vector maps. Figure 6.4 presents the time spectra of the flow, taken at the edge of the wake at a distance of one chord length away from the body. The time spectrum has been calculated from the whole data set and a comparison is made with spectra obtained through measurement by a hot-wire anemometer. Good agreement is shown in terms of the general trend as well as the dominant frequency and its harmonics up to 250 Hz which is the cutoff of the PIV spectrum based on the Nyquist criterion. The dominant frequency appears at 15.6 Hz, which is close to the torsional natural frequency of the dynamical

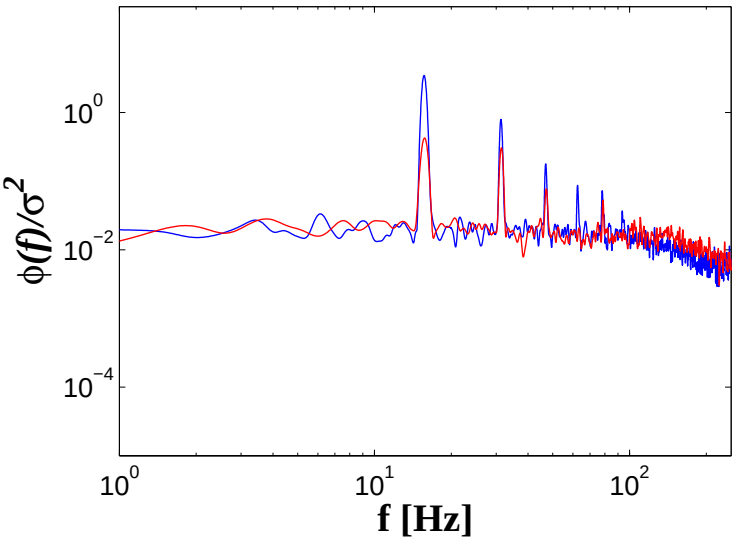

Figure 6.4. Power spectra densities in the frequency domain from PIV data (red) and hot-wire data (blue).

system. It should be noted that the motion of the model is not purely torsional about the centre-of-geometry (CG) since both vertical and torsional motions are observed at, and about, the CG.

There are several classifications of flutter with the classic case being that of coupled flutter. In the case of coupled flutter, both vertical and torsional modes are excited through the action of the flowing fluid. This case has been explored analytically for thin shapes (Theodorsen, 1935). In traditional airfoil flutter the motion is torsional about a point located one quarter of the chord length from the leading edge (Tinar and Cetiner, 2006). A similar observation is made in the current study where the body does not oscillate torsionally about its CG. The CG also oscillates in the vertical direction; however, a point close to one quarter of the chord length from the leading edge remains stationary during the entire build up. Thus, in Figure 6.3 the angular motion of the model about this point is shown with the angle being measured between the model and the streamwise direction. This motion has been estimated by image processing of the portion of the model which appears in the image. Based on the significant motion of the model and the resolution of the images, the estimation of the angle is accurate to 2%. The results of the image processing were then compared with measurements taken by laser displacement transducers to ensure accuracy. Thus, while yielding the velocity fields, the

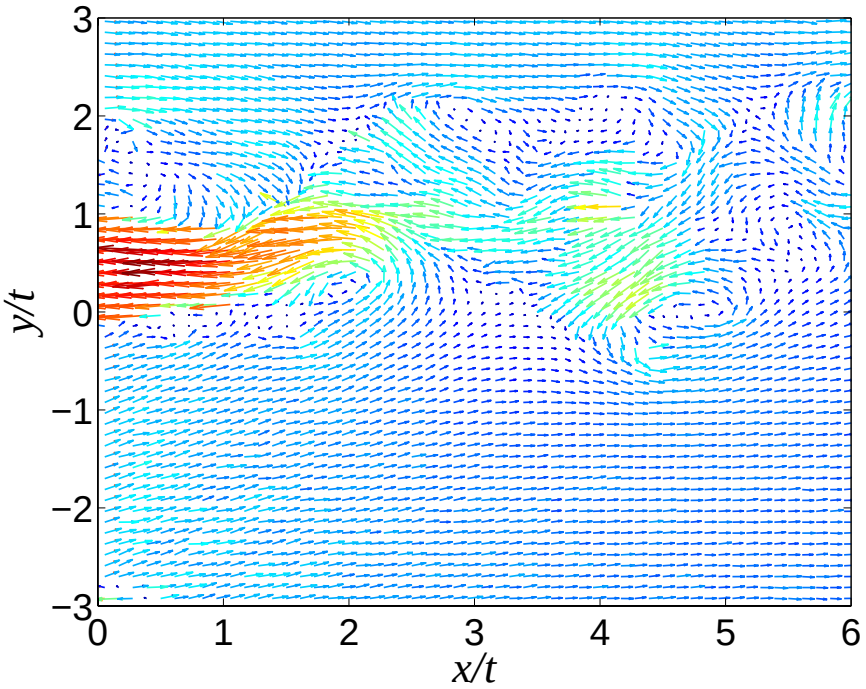

Figure 6.5. Instantaneous fluctuating velocity field in the wake with the mean flow field subtracted from each vector. Colours represent the magnitude of the fluctuating velocity normalized by the free stream speed.

PIV system with the current time-resolution also yields a high-speed video of body motion. In unsteady aerodynamics and hydrodynamics where displacement measurements are more difficult to make – such as avian aerodynamics – the image record could be used to phase-average the results.

6.2.2 *Wake flow field*

A snapshot of the wake velocity field is given in Figure 6.5 where the flow is from left to right. The vectors represent the fluctuating velocities (u' and v') as the mean values, averaged spatially over this snapshot, are subtracted from each vector and the magnitudes are normalized by the mean u component. The model, of thickness t, has its trailing edge centred at (x, y) = (0, 0.5t) at this instant in time thus creating an angle between the model and the direction of flow. One can also observe that the wake centreline is at an angle to the primary flow direction due to the influence of the oscillating body. Critical points have long represented important features in turbulent flows (Perry and Chong, 1987) and examples of some of these can be found in this instantaneous image. Vortices, represented by swirling vectors, are observed at the edges of the wake and there is a clear

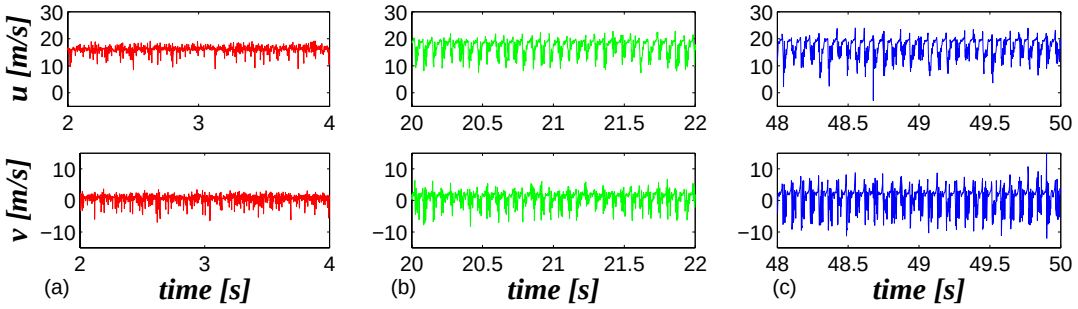

Figure 6.6. Time evolution of streamwise, *u*, and normal, *v*, velocities for three time sets: I: 2-4 sec., II: 20-22 sec. and III: 48-50 sec. from left to right respectively.

saddle point (in this frame of reference) at (x, y) = (3.75t, -0.5t) emphasizing the complexity of the large scale motion of the turbulent flow.

In order to emphasize the different phases of the build-up process, analysis of three data sets is presented in Figure 6.6, each consisting of two seconds: namely, set I: 2-4 sec., II: 20-22 sec. and III: 48-50 seconds. These velocity data are taken at a point offset from the centre of the wake ($x/t = 5$, $y/t = 1$) for the three time intervals. During set I, the body motion is basically zero while set III is taken during the largest amplitude of motion recorded during these experiments (Figure 6.3). Figure 6.3 shows that only a very small increase in free stream speed is required to yield a large increase in model displacement highlighting the divergent nature of the flutter phenomenon.

Figure 6.6a presents the time evolution at the beginning of the build-up where the model has small amplitude motion and the velocity fluctuations detected are primarily from the turbulence created by the presence of the body. As flutter builds up (Figure 6.6b), the velocity amplitude increases and additional frequencies appear as the dynamics of the body affect the wake. Figure 6.6c demonstrates that the amplitude of the oscillation in the flow field is significantly altered due to flutter.

6.2.3 *Turbulence in the wake*

The dynamic behaviour of the body impacts both mean and turbulent flow fields. The Reynolds stresses give an estimate of momentum transfer in the wake and are strong indicators of turbulent activity. Values of the Reynolds shear stress are plotted in Figure 6.7 along vertical profiles in the wake at two locations: $x/t = 3$ and $x/t = 5$. It is shown

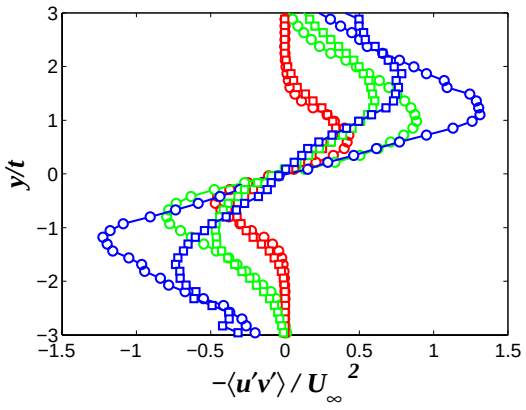

Figure 6.7. Reynolds shear stress profile at the wake. Circle: $x/t = 3$, Square: $x/t = 5$. Time series (as defined in text) I: Red, II: Green, III: Blue.

that for the first time interval (set I) there are small differences in the values of shear stress along the streamwise direction. However, for sets II and III, the Reynolds shear stresses are observed to be reduced by approximately 30% from upstream to downstream locations. These decreases imply that there is stronger turbulent activity nearer the body and that turbulence is enhanced for greater amplitudes of motion.

One of the key features of both turbulent flows in general, and the flutter phenomenon in particular, is that of energy transfer. Closely related to energy transfers in fluid flows are transfers of momentum which are highlighted by the Reynolds shear stresses above. However, another approach to assessing the momentum in the wake is to compute the wake momentum thickness,

$$\theta = \int_{-\infty}^{\infty} \frac{u}{U_\infty}\left(1 - \frac{u}{U_\infty}\right) dy. \tag{6.1}$$

The wake momentum thickness is an estimate of the amount of streamwise momentum lost from the uniform free stream due to the presence of the body. This integration has been performed in the vertical direction in each PIV realization in time at $x/t = 5$ in the wake. The results have then been window averaged (1 second windows) and are shown in Figure 6.8. Also, in Figure 6.8 the standard deviation in each averaging window is marked above and below the mean giving a sense of the fluctuations of the momentum thickness with increasing time. It is observed that the mean momentum thickness increases slowly with time. It should be noted that the momentum thicknesses computed are relative to the instantaneous free stream speed, as shown in Eq. (6.1). Any changes

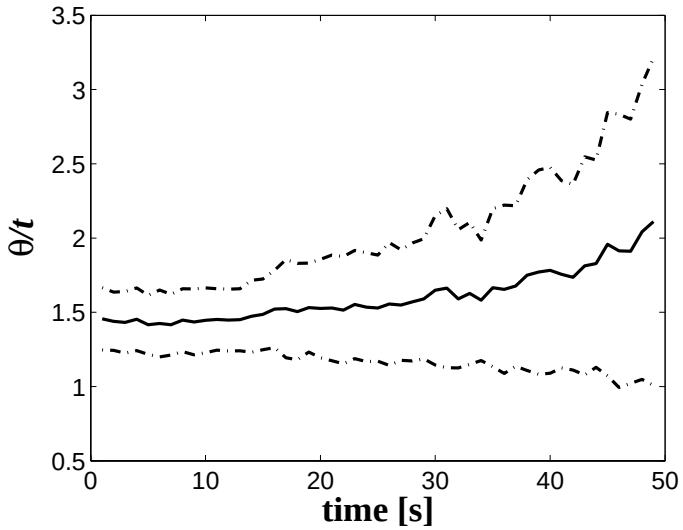

Figure 6.8. Evolution of wake momentum thickness with time at x/t = 5. Time-windowed mean (solid) is bounded either side by one time-windowed standard deviation (dashed).

observed are, thus, due to changes in the ratio u/U_∞ and are not related to the slowly increasing free stream speed, U_∞, in these experiments. Thus, the observed increase in mean momentum thickness implies that the velocity deficit in the wake is increasing with time. The momentum in the wake is also observed to fluctuate significantly at higher amplitudes implying that the rate of change of momentum through a cycle of motion is growing with amplitude. The fluctuating momentum thickness reveals that, while the mean has increased, the instantaneous momentum thickness at higher amplitudes has a smaller value than at lower amplitudes. This result is now explored in light of the connection to energy in the flow.

The velocity deficit is related to the kinetic energy contained in the fluid. A greater velocity deficit indicates lower kinetic energy. Thus, the mean kinetic energy in the fluid appears to decrease slightly with growing amplitude as would be expected. Flutter is known to be the result of overall (structural and aerodynamic) negative damping. Thus, as the free stream speed is increased, the body takes more energy from the flow than it can dissipate which causes the divergent motion. However, less intuitively, the fluctuating momentum thickness implies that at higher amplitudes the wake contains more energy than at lower amplitudes for certain parts of the cycle. This observation implies that as amplitudes increase, energy transferring mechanisms have changed such

that in certain parts of the cycle the body is more efficient at removing energy from the flow than at lower amplitudes.

6.3 Conclusions

The system developed herein is a highly effective tool for the study of unsteady aerodynamics and hydrodynamics. The build-up of bluff body flutter has been studied previously through structural responses and single point measurements. However, the resolution obtained in both time and space, coupled with the record length measured herein, is unprecedented. These measurements reveal the complex nature of momentum transfers in the wake as the body motion grows. The most striking revelation of these measurements results from the evolution of the momentum thickness with time. While the mean momentum thickness increases with time as expected, the fluctuations show an interesting result. The spatio-temporal data obtained with this unique system show that there is more momentum in the wake – for certain parts of the cycle – at higher amplitudes than at lower amplitudes due to the large fluctuations of momentum as the body motion grows. These results suggest varying efficiencies of energy extraction from the flow with the efficiency increasing as the motion is amplified. These results would not have been possible but for the unique combination of high spatial and temporal resolution of time-resolved PIV coupled with the long record length capabilities of this system.

It is expected that this system will yield not only new forms of analysis in the field of fluid mechanics but also new information on the physics of the vast field of unsteady aerodynamics/hydrodynamics. As with other time-resolved PIV systems, data can be obtained for the high frequency components of the flow; however, the long record length of this system ensures that low frequency components are captured as well. This ability can be exploited to perform well-resolved phase averaging of low frequency phenomena. The capabilities of future systems will only improve, and the OpenPIV software solution presented herein, as well as other PIV specific software packages, will require continued development as both the speed and recording length of the various PIV components increase.

Chapter 7

Flow measurements regarding the timing of vortices during flutter*

Although it is now well known how to predict the occurrence of the flutter instability, there is still much about this phenomenon that is poorly understood. Regarding the flow mechanisms involved, Kubo et al. (1992) and Larsen (2000) suggest that it is the arrival of leading edge vortices, timed with the movement of the body, that create the diverging oscillation amplitude. Others have attempted to treat the problem mathematically using nonlinear oscillators (e.g., McKenna, 1999; Green and Unrah, 2006). The hypotheses regarding vortex convection and timing are the only ones that attempt to explain the phenomenon from the point of view of the flow physics. Kubo et al. (1992) used flow visualizations to justify their explanation of the role of vortices in the instability. They hypothesized that it was the number and phasing of vortices across the bridge deck that determined whether the heaving or twisting instabilities are excited. Larsen (2000) took these results and, along with his discrete vortex simulations, built a simple conceptual model based on the motion of the leading edge vortices. One of his assumptions is that vortices convect along the model at a constant convection speed. From these simulations he estimated that the non-dimensional drift time of a vortex to reach half of the chord of the bridge is $T_d = 2$. The non-dimensional time units are defined as $T_d = \tau U_\infty / c$ where τ is dimensional time, U_∞ is the free stream velocity and c is the model chord. With the aforementioned assumptions it is necessary that a vortex convects along the bridge deck at a non-dimensional speed of $U_c/U_\infty = 0.25$. From first principles, it is well known that a vortex has a core of low pressure, thus, a vortex travelling over the bridge deck acts to pull on the deck. Larsen (2000) speculates that it is the timing of these leading edge vortices which act to destabilize the bridge. It is necessary to realize that the position of vortices relative to the phase of the bridge motion based on this will not change with

---

* A version of this chapter has been published in the Journal of Wind Engineering and Industrial Aerodynamics. The full reference is cited herein as Taylor et al., 2010b. Copyright release information can be found in Appendix A.

increasing wind speed. Since the publication of this vortex drift hypothesis, many have assumed it is the controlling instability (e.g., Green and Unrah, 2006). However, there remains very little flow data to support the notion, outside of the numerical discrete vortex simulations.

In their paper on the role of flutter in the collapse of the Tacoma Narrows Bridge, Billah and Scanlan (1991) discuss the existence of two frequencies in the wake at the onset of flutter. They infer that these two frequencies are the vortex shedding frequency of the body and the distinct frequency of the body motion. The two distinct frequencies suggest that neither is being controlled by the other. This result may have been anticipated since Theodorsen (1935) showed that coupled flutter of an airfoil is possible without any leading edge vortices or vortex shedding in his potential flow model. Vortex shedding past elongated bluff bodies is not as well understood as that past shorter bodies such as a circular cylinder. However, there has been meaningful work done to understand the wakes of rectangular cylinders.

The aerodynamics of stationary rectangular cylinders was first addressed by Parker and Welsh (1983) where they assessed the shedding frequency over a wide range of elongation ratios. They found an elongation ratio regime, at a Reynolds number of 3.1×10^4, where regular vortex shedding could not be detected. This elongation ratio range was between $7.6 < c/t < 16$, where c is the chord of the body and t the thickness. At lower Reynolds numbers ($Re < 2000$), Nakamura et al. (1991) found shedding at all elongation ratios. As these bodies become more elongated, a shedding instability is developed which is referred to as the Impinging Leading Edge Vortex (ILEV) instability (Naudascher and Wang, 1993). This instability was proposed originally by Nakamura and Nakashima (1986) as an impinging shear layer instability like that of cavity flows (Rockwell and Naudascher, 1979). At lower Reynolds numbers it is clear that there is a strong feedback from these vortices as they reach the trailing edge (Hourigan et al., 2001). Thus, the leading edge vortices that form the basis of the vortex drift hypothesis play a significant role in determining the vortex shedding past elongated bluff bodies. However, for higher Reynolds numbers, there is no measurable feedback from leading edge vortices formed from a blunt leading edge. Parker and Welsh (1983) show that,

without the organizing effect of the feedback, the wake is only weakly organized, although external forcing does allow the mechanism to occur at much higher Reynolds number. In Part I, it was shown that even though the wake is poorly organized (when no forcing is present) the leading edge vortices play a significant role in determining the wake structure. The experimental setup used for the following results is given in Chapter 5.

7.1 Results

7.1.1 *Displacement results*

The reader is referred to §5.3 for details of the displacement experiments. In these experiments, it was observed for the lower range of wind speeds that the motion was not periodic, but random, due to buffeting of the wind. Once the critical velocity was reached, the structure began to oscillate in a periodic manner increasing in amplitude quite rapidly with increasing velocity (Figure 7.1). In Figure 7.1, it should be noted that the vertical motion of the centre-of-gravity and the rotational motion are occurring simultaneously so that both the vertical and torsional modes are excited. Thus, the motion is clearly a case of coupled bluff body flutter. The ¼-chord point is an important point in classical coupled flutter of an airfoil since this is the location on the body which remains stationary (Tinar and Cetiner, 2006). In other words, the body rotates about this point. It is observed from the free-vibration experiments herein that a point close to the ¼-chord point also remains stationary for this rectangular cylinder. The dominant torsional frequency in the body motion matches the wake frequency (which is shown in Figure 7.1). Both of these frequencies slowly decreased from a value of 16.1 Hz (the torsional natural frequency) to 15.6 Hz with increasing wind speed once flutter began.

From the displacement measurements it is possible to approximate the critical velocity for the body. Divergent response defines the critical condition and from Figure 7.1 it is observed that this response begins at approximately $U_r = 40$. Comparing this value with those of Takai and Sakamoto (2006) shows that the value measured in the current experiments is higher, most likely because of the higher level of damping in the current experiments.

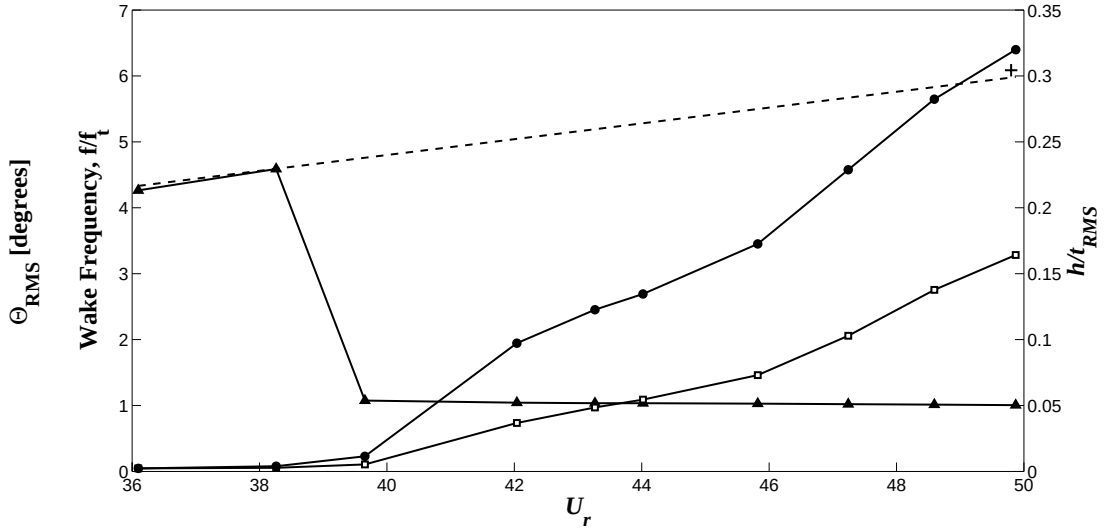

Figure 7.1. Displacement and wake frequency changes with increasing reduced wind speed $U_r=U_\infty/ft$. Left axis denotes values of *rms* angular displacements and wake frequency (normalized by the natural frequency) and the right axis denotes values of the *rms* vertical displacement, *h/t*, of the centre-of-gravity. ▲ – f/f_t, ● – α_{rms}, □ – *h/t*, --- Line of constant Strouhal number, + - Vortex shedding frequency extracted from PIV. (Arrows indicate corresponding vertical axes)

7.1.2 *Wake frequency*

The frequency in the wake was measured using PIV (which was validated against hot-wire measurements). The power spectral density of the vertical velocity component at a point near the edge of the wake is presented in Figure 7.2. The data in Figure 7.2 are taken from the run where $U_r = 50$ and it is observed that the frequency of the model oscillation (and its harmonics) contain the most significant energy in narrow-banded peaks. This energy content should be expected due to the large amplitude oscillation at this velocity (refer to Figure 7.1). However, there is a noticeable, broad-banded, peak in the spectrum around the Strouhal number obtained from static measurements. Also plotted on Figure 7.2 is the spectrum of the sectional lift coefficient, C_L, from surface pressure measurements of the static body. The subtle peak measured in the sectional lift coefficients matches the subtle peak at a similar elongation ratio and Reynolds number measured by Parker and Welsh (1983) in the wake. When both spectra are normalized according to the Strouhal number (St = ft/U_∞) it is observed that the peak in the spectrum when the body is moving coincides with the peak from the spectrum of the sectional lift

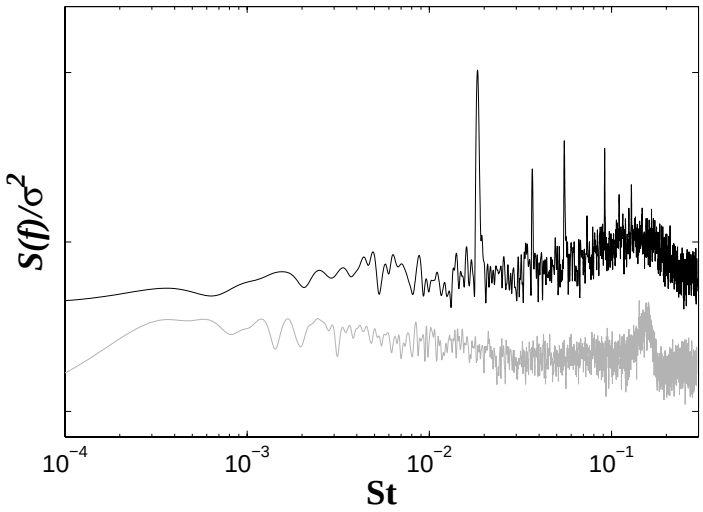

Figure 7.2. Power spectral densities of vertical velocity, v, (black line) for $U_r = 50$ and sectional lift coefficient, C_L, (gray line) for the static model against the Strouhal number. Data are shifted apart from each other to better observe the alignment of the peaks.

in the static model. These data have been shifted vertically apart from one another on the plot so that the alignment of the vortex shedding peaks is clear. The spectrum from the high speed PIV data agrees with the observation made by Billah and Scanlan (1991) that at the onset of flutter there are still two distinct frequencies in the wake: one from the body motion (as well as harmonics) and one from the vortex shedding. This shedding frequency identified from the high-speed PIV has been added to Figure 7.1, with the '+' in the plot near $U_r = 50$. Even though organized vortex shedding is weak for this shape and elongation ratio, it is shown to change little between the static and dynamic cases during flutter.

7.1.3 *Ensemble averages*

Due to the oscillatory nature of the flow it is useful to phase average the data to distinguish features of the flow linked to the oscillations. High Reynolds number (turbulent) flows have a wide range of frequencies which can be separated from the periodic features of the flow (e.g., a moving body or a vortex street wake) with this method. Flow features associated with the periodic or oscillating component are said to be "coherent", in contrast to the incoherence of typical turbulence (e.g., Kiya and Matsumura, 1988). The typical deconstruction of the data follows that of Reynolds and

Hussain (1972) where,

$$f = \bar{f} + \widetilde{f} + f' \tag{7.1}$$

In Eq. 1, above, f is the instantaneous value of the measured variable, $\bar{f}$, is the global, or time-averaged mean of all recorded data, $\tilde{f}$, is the periodic component and f' is the incoherent, fluctuating portion. The periodic component is defined as follows,

$$\widetilde{f} = \langle f \rangle - \bar{f} \tag{7.2}$$

where the phase average, $\langle f \rangle$, is the average of all measured data points (numbering N_i) at a given phase of the cyclical process and is defined as,

$$\langle f \rangle_i = \frac{1}{N_i} \sum_{k=1}^{N_i} f_k \quad i = 1,2,...phases \tag{7.3}$$

A feature of the phase average, as it is defined here, is that the average of the phase averages, over all phases, returns the global, or time-averaged, mean.

Most periodic phenomena of interest have to do with vortices and, since these are usually coherent over substantial lateral regions in shear flows, they do not travel at the local mean velocity; nor are they simply fluctuations about the mean velocity (e.g., Reynolds and Hussain, 1972; Perry et al., 1982). Perry et al. (1982) emphasize the importance of the speed of the observer when analyzing critical points such as vortices in turbulent flow fields, and there has been considerable discussion of vortex identification and vortex convection speed algorithms in the fluid mechanics literature (e.g., Chakraborty et al., 2005). However, it is clear from Perry et al's (1982) work on critical points that the convection speed must be the velocity at the vortex centre so that viewing it at this speed is the clearest representation. Nevertheless, there are practical challenges in defining this when there is strong mean shear present (Vernet et al., 1999).

As discussed previously, there are two frequencies in the flow: one related to vortex shedding and the other to the motion of the model. Phase averages based on both were performed. It should be emphasized that if the flow field at one of the frequencies is unrelated to the other, then the flow features would be smeared out in the averaging process. However, if they are linked, the features should appear in both phase averages.

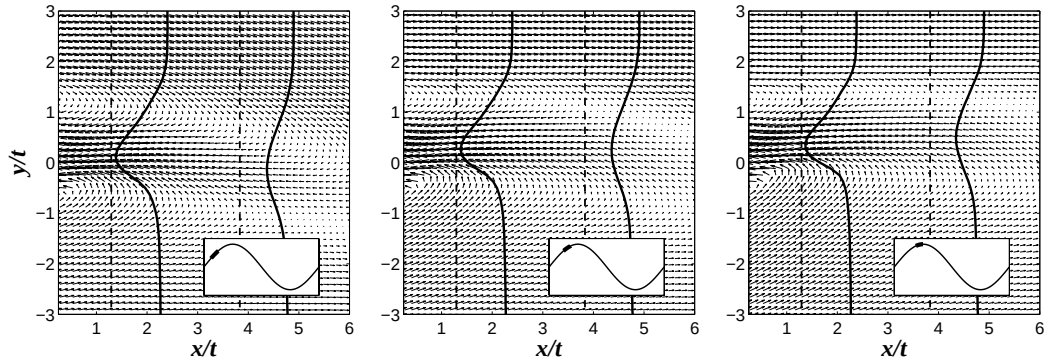

Figure 7.3. Three different phases of the body motion are shown as indicated by bolded portion of the inset. Vector plot of velocity has been phase averaged based on body motion and $0.75U_\infty$ is subtracted from the horizontal speed. Two velocity profiles are shown (taken at dashed lines) and the magnitude of u/U_∞ is scaled to the geometric scale.

In other words, if the data were phase averaged based on the motion of the model, the vortex shedding phenomenon would be smeared and undetectable if it is unrelated to the model motion. This is the key issue of the vortex drift hypothesis so that if shedding of vortices from the leading edge is driving the instability, then such vortices should be clearly associated with the different phases of the model motion during flutter.

Figure 7.3 depicts three of the phases obtained by using a phase average triggered on the motion of the model divided into16 equal bins. The three phases, which are indicated in the insets of the figures, are through to the peak of the body motion when the model is slowing down and about to change direction. In Figure 7.3, a convection speed of $0.75U_\infty$ has been subtracted from the velocity vectors in an attempt to observe vortices; however, the flow looks like a conventionally averaged wake that has shifted due to body motion, a point which is also highlighted by the shown velocity profiles included in the vector fields. In all of the phase averaged fields there are no discernable signs of vortices as they have all been smeared indicating that in the wake there are no vortices aligned by the phase of the motion.

In the second phase-average the trigger is actual identified vortices at fixed locations. In this case, a subset of the data is analyzed that includes only the PIV data for which a vortex is present in a window defined by: $4.5 < x/t < 5.5$ and $-2.5 < y/t < -1.5$ for $U_r = 50$ and $4.5 < x/t < 5.5$, $-1 < y/t < 0$ for the static model. In order to perform this computation, it is necessary to utilize a vortex identification algorithm.

There exists much debate on the strict definition of a vortex (Chakraborty et al., 2005); however, an effective means of identifying a vortex is by the value of the second eigenvalue of the velocity gradient tensor, $u_{i,j} = \partial u_i/dx_j$. This definition for a vortex was originally proposed by Chong et al. (1990) and is valid in three dimensions. Since the vortices of interest are aligned primarily perpendicular to the measurement plane and, considering the lack of information in the third dimension from the PIV data, the analysis is limited to two-dimensions. Adrian et al. (2000) apply the same method to identify vortices in a turbulent boundary layer from PIV data. In two-dimensions, the problem reduces to determining whether the eigenvalues of the two-dimensional velocity gradient tensor are real or complex. If complex, it suggests that the flow is swirling about the point; or, that a vortex is present. It is this estimate of swirl that differentiates this method from identification based on vorticity contours since regions of high shear can have high values of vorticity without the presence of the swirling fluid typical of a vortex. In the presence of a vortex, the complex portion (Eq. (7.4)) of the complex pair can be thought of as the level of swirl around the vortex or the "swirling strength" (Adrian et al., 2000).

$$\lambda_{ci} = \sqrt{\frac{\partial u}{\partial y}\frac{\partial v}{\partial x} - \frac{\partial u}{\partial x}\frac{\partial v}{\partial y}} \tag{7.4}$$

Once the subset of the data is selected based on vortex position, one last part of the algorithm is performed to reduce smearing effects. This last step entails shifting the vortices within this small window such that the centres coincide on the average vortex centre position and then all of the velocity maps within this subset are averaged. The results of this phase average for the static model are shown in Figure 7.4a as a vector plot, while those for $U_r = 50$ are shown in Figure 7.4b. The contours in Figure 7.4 are the values of λ_{ci} computed directly from the phase averaged velocity field. Although a Kármán vortex street is not clearly observed in Figure 7.4b, this result was expected since a similar pattern is observed for a static body at a similar Reynolds number, as shown in Figure 7.4a. The weak periodicity of the two figures is consistent with the spectra given in Figure 7.2.

7.1.4 *Vortex motion*

The motion of the vortices considered in this section has to do with their location relative to the deck motion and also an approximation of their convection speed. Though the phase averages suggest there is no correlation between body motion and vortex motion, with the data collected it is possible to assess this correlation. A body defined co-ordinate system (*x',y'*) is used in this case and its origin is located at the middle of the trailing edge surface with the *x'*-axis extending perpendicular to this surface. Analysis has been performed identifying which frames (from a total of 15 000) have a vortex located at *x'*=2*t*. A window of 1*t* x 1*t* was centred at this location and only vortices with sufficient circulation and the same direction of rotation were included. If a vortex was present in this window, the angular position of the model was recorded. The distribution of these corresponding angular positions of the model is indicated in Figure 7.5 as well as the distribution of the entire time series of model position. The observation that the two distributions are nearly identical shows that the position of the vortices is independent of the deck position. If the timing of the vortices was in some way synchronized with the angular position of the body then the distribution would be markedly different. In that case, the distribution would show that it is highly probable for the model to be at a certain angular position for a prescribed vortex location. However, Figure 7.5 shows that for a

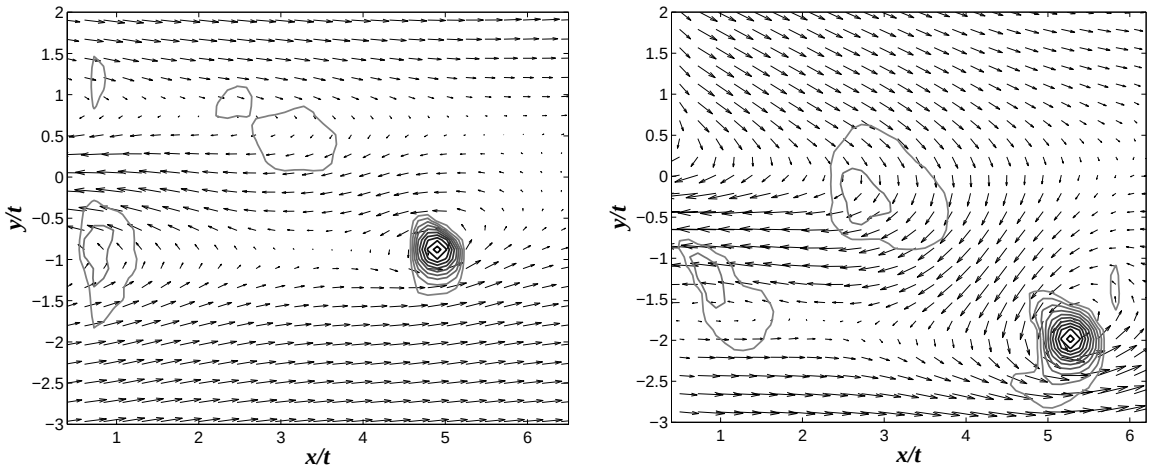

Figure 7.4. Ensemble averaged PIV frames based on vortex position of $x = 5t$. The contours show the swirling strength in each ensemble averaged frame. Frame on the left is taken from static measurements, while frame on the right is taken in the wake of the fluttering body at U_r = 50. Horizontal speed of $0.75U_\infty$ is subtracted from each frame.

given vortex location (in this case $x' = 2t$) the model can be at any angular position throughout its travel.

Measurements were also performed around the surface of the oscillating body to approximate the convection speed of the vortices. The vortex drift hypothesis is based on the notion that vortices travel at $0.25U_\infty$. Tan et al. (2004), as well as Liu and Kopp (2011), have shown the speed of vortices across different rectangular cylinders through numerical simulations. While these vortices are shed at a relatively low convection speed they travel at close to $0.75U_\infty$ as they approach the trailing edge of a body with $c/t = 7$. A limited PIV dataset was captured around the surface of the body. An instantaneous velocity map from this dataset is shown in Figure 7.6. In this figure, $0.75U_\infty$ has been subtracted from the horizontal velocity. It is clear from this figure that the vortex near the trailing edge is traveling near this expected convection speed as it is well observed in this frame of reference.

7.2 Discussion

In this section, the presented data are discussed with regards to the vortex drift hypothesis. If one is to assume that it is the precise location of the vortices that cause the instability then one must assume that either the body oscillates at different frequencies

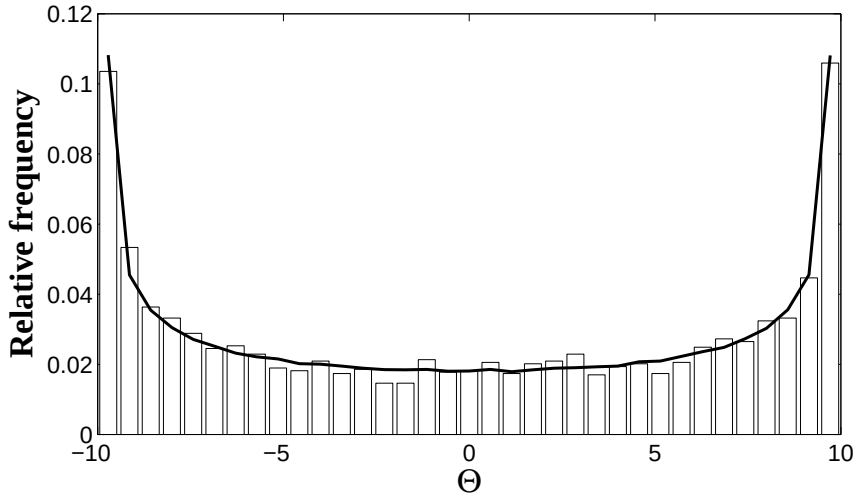

Figure 7.5. Distribution of the relative frequency (number of occurrences in each bin/total occurrences) of the angular position of the model, Θ, in degrees. Bars represent the distribution of the model's angular position when a vortex is at $x'=2t$ and the solid line is the distribution of the measured angular displacement of the model.

with increasing wind speed or, if the body remains at a constant frequency, that the shedding frequency of vortices does not change with increasing wind speed so that the Strouhal number drops continuously. Figure 7.1 showed that the frequency of the model changed only slightly as wind speed was increased. This result agrees well with that of Takai and Sakamoto (2006) who also found that the frequency of the body oscillations remained relatively unchanged with increasing wind speed. Thus, for the vortex drift hypothesis to function as described, the vortex shedding frequency must readjust with increasing wind speed such that the vortex is at the same position relative to the phase of body motion. It is well known that vortex shedding frequency generally increases linearly with increasing wind speed. Exceptions to this trend happen when there is an external forcing agent such as organized sound or mechanical forcing. Surely, flutter offers the latter type of forcing. However, the forcing frequency must be close to the natural shedding frequency to lock it to a different frequency. From Figure 7.1 it is clear that the shedding frequency is far from the model frequency when motion begins. Furthermore, Figure 7.2 and the comments of Billah and Scanlan (1991) show that indeed there are two significant frequencies in the wake at the onset of flutter.

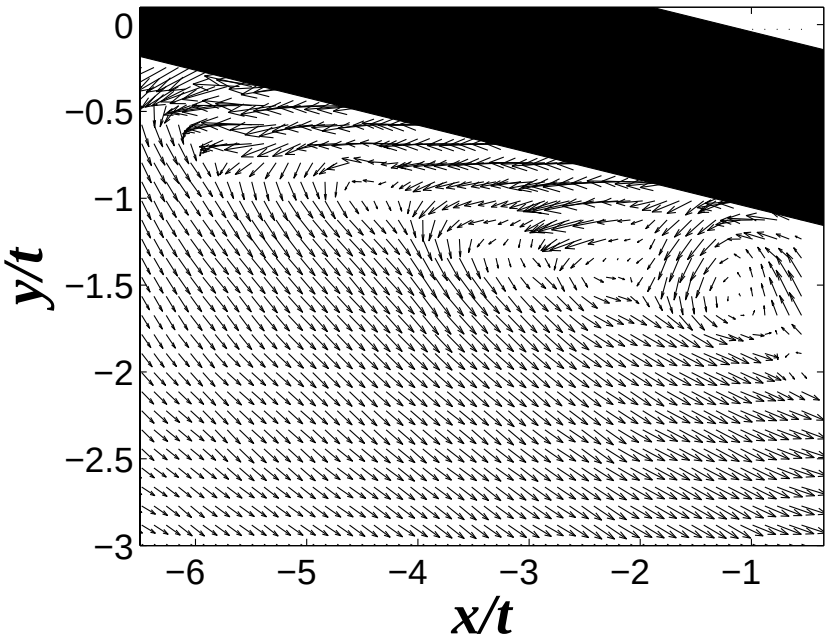

Figure 7.6. Instantaneous vector map taken underneath the oscillating body. Horizontal velocity component has $0.75U_\infty$ subtracted.

The existence of two unrelated frequencies in the wake suggests that the motion of vortices is not controlling the instability. When the phase average was performed on the data based solely on body position (Figure 7.3), no vortices were found in the average velocity field further suggesting that the two periodic phenomena in the flow are not linked. It was only when an ensemble average based on vortex position was performed that vortex patterns emerged. From Figure 7.4 it was observed that the vortex wake pattern was largely unchanged from the static case, rather it was shifted by the motion of the body. In watching video from the high speed PIV results at $U_r = 50$, it is clear that the frequency of vortex shedding is so much faster (approximately 6 times, from Figure 7.1) that the relatively slow moving body only has the effect of 'swinging' the wake, as is shown in Figure 7.3. There is another result in Figure 7.4 which helps to confirm the observation of dual frequencies. From the pattern in Figure 7.4 it is possible to estimate the half wavelength of vortex shedding and, from assuming a relatively constant convection speed of the vortices, a shedding frequency. An estimate at this wind speed puts the ratio of shedding frequency to model frequency at approximately 6 which agrees well with the measured shedding frequency from the PIV plotted in Figure 7.1. The distribution of deck position in Figure 7.5 shows conclusively that vortex position and the angular position of the deck are uncorrelated since vortices appear at the same relative location in the wake regardless of the position of the deck.

Since the flow patterns match well between the static and dynamic wakes, it is expected that the flow along the body during oscillations is similar to that from static experiments. The PIV results under the body show that vortices are traveling along the body similar to when the body is static (Tan et al., 2004). From previous studies it is known that although near the separation point vortices may move as slowly as $0.25U_\infty$ most of the time that they travel along the body they are going faster than $0.6U_\infty$ (Tan et al., 2004; Liu and Kopp, 2010). From the static results taken herein and those previously published (e.g., Mills et al., 2002), it is clear that leading edge vortex shedding is the controlling mechanism for the vortex shedding wakes of elongated rectangular cylinders. Thus, it should be noted that the shedding frequency measured in the wake is a direct result of vortices being shed from the leading edge. These results prevent the notion that the vortices are timed over the surface in such a way as to match the model's motion only to

rearrange themselves to a completely different frequency in the wake. In fact, from the analysis of static measurements in Chapter 2 it is likely that the vortices in the wake are primarily those shed from the leading edge for this rectangular body and the fluttering body is not creating new vortices, at least for the range of amplitudes observed in this study. It should also be recalled that the phenomenon of flutter can be predicted based on potential flow for a thin plate (Theodorsen, 1935) which does not have vortices being shed from the leading edge. The mechanisms contained in the coupled system of equations determine the instability of the system and not necessarily the drift of the leading edge vortices. The timing between the two phenomena is too poor for their influence to be as great as once thought.

7.3 Conclusions

The flutter phenomenon is complex and there has recently been a notion that leading edge vortices are responsible for the instability. However, the data taken herein have shown that the vortex shedding activity remains relatively unchanged from the static case even when significantly large amplitude oscillations are measured. This result was shown by the fact that there are two significant and distinct frequencies in the wake. The lower frequency is narrow-banded and matches the frequency of the model's motion. The higher frequency is broad-banded and matches the shedding frequency. The existence of two distinct frequencies suggests that vortex drift is not responsible for the instability. Furthermore, it was shown by ensemble averaging by vortex position, that the vortex pattern remains largely unchanged from static measurements, and that the deck position is independent of the vortex position in the wake. The static case is dominated by the leading edge vortices, thus, the similarity in wake vortex patterns indicates that the leading edge vortex activity is not significantly changed even though the amplitude of body motion is large.

The fact that Theodorsen (1935) predicted the onset of flutter using a potential flow model, mixed with the results taken herein, indicates that there is something fundamentally unstable in the coupled set of equations. Between thin plates and bluff bodies there are significant differences in the flow fields. The major differences are the presence of leading edge vortices and vortex shedding. However, while the phenomena

of bluff body flutter is not the same as that predicted by Theodorsen (1935) there are enough similarities to infer that while the leading edge vortices and subsequent vortex shedding play some role, they are not the main destabilizing feature of the phenomenon.

References

Adrian, R.; Christensen, K. and Liu, Z. (2000), Analysis and interpretation of instantaneous turbulent velocity fields, *Experiments in Fluids* **29**, 275-290.

Adrian, R. J. (1991), Particle-imaging techniques for experimental fluid mechanics, *Annual Review of Fluid Mechanics* **23**, 261-304.

Andreopoulus, J. and Agui, J. (1996), Wall-vorticity flux dynamics in a two-dimensional turbulent boundary layer, *Journal of Fluid Mechanics* **309**, 45-84.

Bailey S. (2001), The effect of wall proximity on vortex shedding from a square cylinder, M.E.Sc thesis. *The University of Western Ontario*.

Balachandar, S.; Mittal, R. and Najjar, F. (1997), Properties of the mean recirculation region in the wakes of two-dimensional bluff bodies, *Journal of Fluid Mechanics* **351**, 167-199.

Bartoli, G.; Contri, S.; Mannini, C. and Righi, M. (2009), Toward an improvement in the identification of bridge deck flutter derivatives, *Journal of Engineering Mechanics, ASCE* **135**, 771-785.

Battista, R. C. and Pfeil, M. S. (2000), Reduction of vortex-induced oscillations of Rio-Niteroi bridge by dynamic control devices, *Journal of Wind Engineering and Industrial Aerodynamics* **84**, 273-288.

Bearman, P. (2009), Understanding and predicting vortex-induced vibrations, *Journal of Fluid Mechanics* **634**, 1-4.

Bearman, P. (1967), On vortex street wakes, *Journal of Fluid Mechanics* **28**, 625-641.

Benesty, J.; Chen, J. and Huang, Y. (2005), A generalized MVDR spectrum, *IEEE Signal Processing Letters* **12**, 827-830.

Bernal, L. and Roshko, A. (1986), Streamwise vortex structure in plane mixing layers, *Journal of Fluid Mechanics* **170**, 499-525.

Billah, K. Y. and Scanlan, R. H. (1991), Resonance, Tacoma Narrows bridge failure, and undergraduate physics textbooks, *American Journal of Physics* **59**, 118-124.

Cantwell, B. and Coles, D. (1983), An experimental study of entrainment and transport in the turbulent near wake of a circular cylinder, *Journal of Fluid Mechanics* **136**, 321-374.

Castro, I. P. and Epik, E. (1998), Boundary layer development after a separated region, *Journal of Fluid Mechanics* **374**, 91-116.

Castro, I. P. and Haque, A. (1987), The structure of a turbulent shear layer bounding a separation region, *Journal of Fluid Mechanics* **179**, 439-468.

Chakraborty, P.; Balachandar, S. and Adrian, R. J. (2005), On the relationships between local vortex identification schemes, *Journal of Fluid Mechanics* **535**, 189-214.

Chen, J. and Katz, J. (2005), Elimination of peak-locking error in PIV analysis using the correlation mapping method, *Measurement Science and Technology* **16**, 1605-1618.

Cherry, N.; Hillier, R. and Latour, M. (1984), Unsteady measurements in a separated and reattaching flow, *Journal of Fluid Mechanics* **144**, 13-46.

Choi, H.; Jeon, W. and Kim, J. (2008), Control of flow over a bluff body, *Annual Review of Fluid Mechanics* **40**, 113-139.

Chong, M.; Perry, A. and Cantwell, B. (1990), A general classification of three-dimensional flow fields, *Physics of Fluids, A* **2**, 765-777.

Deane, A.; Kevrekidis, I.; Karniadakis, G. and Orszag, S. (1991), Low-dimensional models for complex geometry flows: Application to grooved channels and circular cylinders, *Physics of Fluids, A* **3**, 2337-2354.

Diamessis, P. J.; Gurka, R. and Liberzon, A. (2010), Spatial characterization of vortical structures and internal waves in a stratified turbulent wake using proper orthogonal decomposition, *Physics of Fluids* **22**, 08801.

Diana, G.; Rocchi, D.; Argentini, T. and Muggiasca, S. (2010), Aerodynamic instability of a bridge deck section model: Linear and nonlinear approach to force modeling, *Journal of Wind Engineering and Industrial Aerdoynamics* **98**, 363-374.

Dipankar, A.; Sengupta, T. and Talla, S. (2007), Suppression of vortex shedding behind a circular cylinder by another control cylinder at low Reynolds numbers, *Journal of Fluid Mechanics* **573**, 171-190.

Djilali, N. and Gartshore, I. (1991), Effect of leading-edge geometry on a turbulent separation bubble, *American Institute of Astronautics and Aeronautics* **30**, 559-5610.

Echols, W. and Young, J. (1963), Studies of portable air-operated aerosol generators, Technical Report 5929, Naval Research Laboratory.

Fage, A. and Johansen, F. (1928), The structure of vortex sheets, *Philosophical Magazine* **5**, 417-441.

Ferré J. and Giralt, F. (1989), Some topological features of the entrainment process in a heated turbulent wake, *Journal of Fluid Mechanics* **198**, 68-78.

Frigo M. and Johnson, S.G. (2009), FFTW Home Page. http://www.fftw.org.

Fujino, Y. and Yoshida, Y. (2002), Wind-induced vibration and control of Trans-Tokyo Bay Crossing Bridge, *Journal of Structural Engineering* **128**, 1012-1025.

Gerrard, J. H. (1966), The mechanics of the formation region of vortices behind bluff bodies, *Journal of Fluid Mechanics* **25**, 401-413.

Green, D. and Unrah, W. G. (2006), The failure of the Tacoma Bridge: A physical model, *American Journal of Physics* **74**, 706-716.

Green, R. and Gerrard, J. (1993), Vorticity measurements in the near wake of a circular cylinder at low Reynolds numbers, *Journal of Fluid Mechanics* **246**, 675-691.

Gurka, R.; Liberzon, A.; Hefetz, D.; Rubinstein, D. and Shavit, U. (1999), Computation of pressure distribution using PIV velocity data, In: *3rd International Workshop on PIV*.

Gurka, R.; Liberzon, A. and Hetsroni, G. (2006), POD of vorticity fields: A method for spatial characterization of coherent structures, *International Journal of Heat and Fluid Flow* **27**, 416-423.

Gurka, R.; Liberzon, A. and Hetsroni, G. (2004), Detecting coherent patterns in a flume by using PIV and IR imaging techniques, *Experiments in Fluids* **37**, 230-236.

Hazarika, B. and Hirsch, C. (1994), Behavior of separation bubble and reattached boundary layer around a circular leading edge, In: *International Gas Turbine and Aeroengine Congress and Exposition*, The Hague, Netherlands.

Ho, T.C.E.; Lythe, G.R. and Isyumov., N. (1999), Structural loads and responses from the integration of simultaneous pressures, In: *Proceedings of the 10th International Conference on Wind Engineering*, Copenhagen, Denmark, 1505-1510.

Hourigan, K.; Thompson, M. C. and Tan, B. T. (2001), Self-sustained oscillations in flows around long blunt plates, *Journal of Fluids and Structures* **15**, 387-398.

Huang, H.; Dabiri, D. and Gharib, M. (1997), On errors of digital particle image velocimetry, *Measurement Science and Technology* **8**, 1427-1440.

Hubel, T. Y.; Hristov, N. I.; Swartz, S. M. and Breuer, K. S. (2009), Time-resolved wake structure and kinematics of bat flight, *Experiments in Fluids* **46**, 933-943.

Keane, R. D. and Adrian, R. J. (1990), Optimization of particle image velocimeters. Part I: Double pulsed systems, *Measurement Science and Technology* **1**, 1202-1215.

King, J.P.C. (2003), The aerodynamics of long-span bridges. Ph.D. thesis, *University of Western Ontario*.

Kiya, M. and Matsumura, M. (1988), Incoherent turbulence structure in the near wake of a normal plate, *Journal of Fluid Mechanics* **190**, 343-356.

Kiya, M. and Sasaki, K. (1983), Structure of a turbulent separation bubble, *Journal of Fluid Mechanics* **137**, 83-113.

Kopp, G.; Kawall, J. and Keffer, J. (1995), The evolution of coherent structures in a uniformly distorted turbulent wake, *Journal of Fluid Mechanics* **291**, 299-322.

Kopp, G.A. and Keffer, J.F. (1996a), Coherent structures in two uniformly distorted plane turbulent wakes, *Physics of Fluids* **8**, 2706-2711.

Kopp, G.A. and Keffer, J.F. (1996b), The near wake region of a high solidity mesh-strip, *Physics of Fluids* **8**, 2712-2715.

Kubo, Y.; Hirata, K. and Mikawa, K. (1992), Mechanism of aerodynamic vibrations of shallow bridge girder sections, *Journal of Wind Engineering and Industrial Aerodynamics* **41-44**, 1297-1308.

Lardeau, S.; Tessicini, F. and Leschziner, M. A. (2010), Analysis of cyclic events in turbulent flows using recurrence plots, *Journal of Turbulence* **11**, 1-27.

Larsen, A. (2000), Aerodynamics of the Tacoma Narrows Bridge - 60 years later, *Structural Engineering International* **4**, 243-248.

Larsen, A.; Esdahl, S.; Anderson, J. E. and Vejrum, T. (2000), Storebælt suspension bridge - vortex shedding excitation and mitigation by guide vanes, *Journal of Wind Engineering and Industrial Aerodynamics* **88**, 283-296.

Li, M.; Du, H.; Zhang, Q. and Wang, J. (2008), Improved particle image velocimetry through cell segmentation and competitive survival, *IEEE Transactions on Instrumentation and Measurement* **57**, 1221-1229.

Liberzon, A.; Gurka, R. and Hetsroni, G. (2001), Vorticity characterization in a turbulent boundary layer using PIV and POD analysis, In: *4th International Symopsium on Particle Image Velocimetry*.

Liberzon, A.; Gurka, R. and Taylor Z. (2009), OpenPIV Home Page, http://www.openpiv.net.

Lighthill, M.J. (1963), *Boundary layer theory. In: Laminar Boundary Layers* (ed. L. Rosenhead), Oxford University Press.

Liu, Z. (2009), Effects of geometry on vortex shedding from elongated bluff bodies. Ph.D. thesis, *University of Western Ontario*.

Liu, Z. and Kopp, G. A. (2011), High-resolution vortex particle simulations of flows around rectangular cylinders, *Computers & Fluids* **40**, 2-11.

Lumley, J. (1970), *Stochastic tools in turbulence*, Dover Publications.

Ma, X. and Karniadakis, G. (2002), A low-dimensional model for simulating three-dimensional cylinder flow, *Journal of Fluid Mechanics* **458**, 181-190.

Matsumoto, M.; Daito, Y.; Yoshizumi, F.; Ichikawa, Y. and Yabutani, T. (1997), Torsional flutter of bluff bodies, *Journal of Wind Engineering and Industrial Aerodynamics* **69-71**, 871-882.

McKenna, P. (1999), Large torsional oscillations in suspension bridges revisited: fixing an old approximation, *The American Mathematical Monthly* **106**, 1-18.

Mills, R.; Sheridan, J. and Hourigan, K. (2003), Particle image velocimetry and visualization of natural and forced flow around rectangular cylinders, *Journal of Fluid Mechanics* **478**, 299-323.

Mills, R.; Sheridan, J. and Hourigan, K. (2002), Response of base suction and vortex shedding from rectangular prisms to transverse forcing, *Journal of Fluid Mechanics* **461**, 25-49.

Morse, T. and Williamson, C. (2009), Prediction of vortex-induced vibration response by employing controlled motion, *Journal of Fluid Mechanics* **634**, 5-39.

Nakamura, Y. and Nakashima, M. (1986), Vortex excitation of prisms with elongated rectangular, H and T cross-sections, *Journal of Fluid Mechanics* **163**, 149-169.

Nakamura, Y.; Ohya, Y. and Tsuruta, H. (1991), Experiments on vortex shedding from flat plates with square leading and trailing edges, *Journal of Fluid Mechanics* **222**, 437-447.

Naudascher, E. and Wang, Y. (1993), Flow-induced vibrations of prismatic bodies and grids of prisms, *Journal of Fluids and Structures* **7**, 341-373.

Nguyen, T. D. and Naudascher, E. (1991), Vibration of beams and trashracks in parallel and inclined flows, *Journal of Hydraulic Engineering* **117**, 1056-1076.

Noack, B. R.; Afanasiev, K.; Morzynski, M.; Tadmor, G. and Thiele, F. (2003), A hierarchy of low-dimensional models for the transient and post-transient cylinder wake, *Journal of Fluid Mechanics* **497**, 335-363.

Nokia Corporation (2009), Qt – A cross-platform application and UI framework, http://qt.nokia.com.

Okajima, A. (1982), Strouhal numbers of rectangular cylinders, *Journal of Fluid Mechanics* **123**, 379-398.

Okamoto, K.; Nishio, S.; Saga, T. and Kobayashi, T. (2000), Standard images for particle-image velocimetry, *Measurement Science and Technology* **11**, 685-691.

van Oudheusden, B.; Scarano, F.; van Hinsberg, N. and Watt, D. (2005), Phase-resolved characterization of vortex shedding in the near wake of a square-section cylinder at incidence, *Experiments in Fluids* **39**, 86-98.

Parker, R. and Welsh, M. (1983), Effects of sound on flow separation from blunt plates, *International Journal of Heat and Fluid Flow* **4**, 113-127.

Pastoor, M.; Henning, L.; Noack, B. R.; King, R. and Tadmor, G. (2008), Feedback shear layer control for bluff body drag reduction, *Journal of Fluid Mechanics* **608**, 161-196.

Perry, A. E. and Chong, M. S. (1987), A description of eddying motions and flow patterns using critical-point concepts, *Annual Review of Fluid Mechanics* **19**, 125-155.

Perry, A. E.; Chong, M. S. and Lim, T. T. (1982), The vortex-shedding process behind two-dimensional bluff bodies, *Journal of Fluid Mechanics* **116**, 77-90.

Ponte, S. D.; Malavasi, S.; Galzerano, G. and Svelto, C. (2004), Novel particle image velocimetry system based on three-color pulsed lamps and image processing, *IEEE Transactions on Instrumentation and Measurement* **53**, 175-180.

Raffel, M.; Willert, C. and Kompenhans, J. (1998), *Particle image velocimetry: a practical guide*, 1st ed., Berlin: Springer.

Ram, H. G. and Arakeri, V. (1990), Studies on unsteady pressure fields in the region of separating and reattaching flows, *Journal of Fluids Engineering* **112**, 402-408.

Rapun, M. and Vega, J. M. (2010), Reduced order models based on local POD plus Galerkin projection, *Journal of Computational Physics* **229**, 3046-3063.

Reynolds, W. and Carr, L. (1985), Review of unsteady, driven, separated flow, AIAA Shear Flow Control Conference, Ref. No. 85-0527.

Reynolds, W. and Hussain, A. (1972), The mechanics of an organized wake in turbulent shear flow. Part 3. Theoretical models and comparisons with experiments, *Journal of Fluid Mechanics* **54**, 263-288.

Rockwell, D. and Naudascher, E. (1979), Self-sustained oscillations of impinging free shear layers, *Annual Review of Fluid Mechanics* **11**, 67-94.

Roshko, A. (1993), Perspectives on bluff body aerodynamics, *Journal of Wind Engineering and Industrial Aerodynamics* **49**, 79-100.

Roshko, A. (1961), Experiments on the flow past a circular cylinder at very high Reynolds number, *Journal of Fluid Mechanics* **10**, 345-356.

Roshko, A. (1954a), On the drag and shedding frequency of two-dimensional bluff bodies, NACA Technical Note 3169.

Roshko, A. (1954b), A new hodograph for free-streamline theory, NACA Technical Note 3168.

Roshko, A. and Lau, J. (1965), Some observations on transition and reattachment of a free shear layer in incompressible flow, In: *Proceedings of the Heat Transfer and Fluid Mechanics Institute* **18**, 157-167.

Saffman, P. and Schatzman, J. (1982), Stability of a vortex street of finite vortices. *Journal of Fluid Mechanics* **117**, 171-185.

Scanlan, R. and Sabzevari, A. (1969), Experimental aerodynamic coefficients in the analytical study of suspension bridge flutter, *Journal of Mechanical Engineering Science* **11**, 234-242.

Scanlan, R. H. and Tomko, J. J. (1971), Airfoil and bridge deck flutter derivatives, *Journal of the Engineering Mechanics Division ASCE* **97**, 1717-1737.

Simpson, R. L. (1989), Turbulent boundary-layer separation, *Annual Review of Fluid Mechanics* **21**, 205-234.

Sirovich, L. (1987), Turbulence and the dynamics of coherent structures, Part I: Coherent structures, *Quarterly of Applied Mechanics* **45**, 561-571.

Smith, T. R.; Moehlis, J. and Holmes, P. (2005), Low-dimensional modeling of turbulence using the proper orthogonal decomposition: A tutorial, *Nonlinear Dynamics* **41**, 275-307.

Song, S. and Eaton, J.K. (2002), The effects of wall roughness on the separated flow over a smoothly contoured ramp, *Experiments in Fluids* **33**, 38-46.

Stanislas, M.; Okamoto, K.; Kaehler, C. and Westerweel, J. (2005), Main results of the Second International PIV Challenge, *Experiments in Fluids* **39**, 170-191.

Stokes, A. and Welsh, M. (1986), Flow-resonant sound interaction in a duct containing a plate, II: Square leading edge, *Journal of Sound and Vibration* **104**, 55-73.

Strykowski, P. and Sreenivasan, K. (1990), On the formation and suppression of vortex 'shedding' at low Reynolds numbers, *Journal of Fluid Mechanics* **218**, 71-107.

Szepessy, S. and Bearman, P. (1992), Aspect ratio and end plates on vortex shedding from a circular cylinder, *Journal of Fluid Mechanics* **234**, 191-217.

Takai, K. and Sakamoto, H. (2006), Response characteristics and suppresion of torsional vibration of rectangular prisms with various width-to-depth ratios, *Wind and Structures* **9**, 1-22.

Tan, B. T.; Thompson, M. C. and Hourigan, K. (2004), Flow past rectangular cylinders: receptivity to transverse forcing, *Journal of Fluid Mechanics* **515**, 33-62.

Taylor, Z.; Gurka, R. and Kopp, G. (2007), Wake measurements for a rectangular cylinder during torsional oscillation, In: *Proceedings 7th International Symposium on PIV*.

Taylor, Z. J.; Gurka, R.; Kopp, G. A. and Liberzon, A. (2010a), Long-duration time-resolved PIV to study unsteady aerodynamics, *IEEE Transactions on Instrumentation and Measurement* **59**, 3262 - 3269.

Taylor, Z. J.; Kopp, G. A. and Gurka, R. (2010b), Flow measurements regarding the timing of vortices during flutter, *Journal of Wind Engineering and Industrial Aerodynamics* **98**, 864-871.

Taylor, Z. J.; Palombi, E.; Gurka, R. and Kopp, G. A. (2011), Features of the turbulent flow around symmetric elongated bluff bodies, *Journal of Fluids and Structures* **27**, 250-265.

Theodorsen, T. (1935), General theory of aerodynamic instability and the mechanism of flutter, NACA Technical Report 496.

Tinar, E. and Cetiner, O. (2006), Acceleration data correlated with PIV images for self-induced vibrations of an airfoil, *Experiments in Fluids* **41**, 201-212.

Tombazis, N. and Bearman, P. (1997), A study of three-dimensional aspects of vortex shedding from a bluff body with a mild geometric disturbance, *Journal of Fluid Mechanics* **330**, 85-112.

Tritton, D.J. (1988), *Physical Fluid Dynamics*, 2nd Ed., Oxford University Press.

Troolin, D.; Longmire, E. and Lai, W. (2006), Time resolved PIV analysis of flow over a NACA 0015 airfoil with Gurney flap, *Experiments in Fluids* **41**, 241-254.

Vernet, A.; Kopp, G. A.; Ferré, J. A. and Giralt, F. (1999), Three-dimensional structure and momentum transfer in a turbulent cylinder wake, *Journal of Fluid Mechanics* **394**, 303-337.

Welsh, M.; Stokes, A. and Parker, R. (1984), Flow-resonant sound interaction in a duct containing a plate, part 1: Semi-circular leading edge, *Journal of Sound and Vibration* **95**, 305-323.

Wernet, M. P. (2007), Temporally resolved PIV for space-time correlations in both cold and hot jet flows, *Measurement Science and Technology* **18**, 1387-1403.

Williams, T. C.; Hargrave, G. K. and Halliwell, N. A. (2003), The development of high-speed particle image velocimetry (20 kHz) for large eddy simulation code refinement in bluff body flows, *Experiments in Fluids* **35**, 85-91.

Williamson, C. (1996), Vortex dynamics in the cylinder wake, *Annual Review of Fluid Mechanics* **28**, 477-539.

Wu, S.; Miau, J.; Hu, C. and Chou, J. (2005), On low-frequency modulations and three-dimensionality in vortex shedding behind a normal plate, *Journal of Fluid Mechanics* **526**, 117-146.

Wygnanski, I.; Champagne, F. and Marasli, B. (1986), On the large-scale structures in two-dimensional, small-deficit, turbulent wakes, *Journal of Fluid Mechanics* **168**, 31-71.

Yeung, W. and Parkinson, G. (2004), Analysis and modeling of pressure recovery for separated reattaching flows, *Journal of Fluids Engineering* **126**, 355-361.

Zdravkovich, M. (1997), *Flow Around Circular Cylinders: Volume 1: Fundamentals*, Oxford University Press.

Zhou, Y. and Antonia, R. (1994), Effect of initial conditions on vortices in a turbulent near wake, *American Institute of Aeronautics and Astronautics* **32**, 1207-1213.

Appendix A

Permissions for reuse of copyrighted materials

There are three articles in this integrated-article thesis which have previously been published. They are listed here for context:

- Taylor, Z. J.; Gurka, R.; Kopp, G. A. and Liberzon, A. (2010a), Long-duration time-resolved PIV to study unsteady aerodynamics, *IEEE Transactions on Instrumentation and Measurement* **59**, 3262 - 3269.

- Taylor, Z. J.; Kopp, G. A. and Gurka, R. (2010b), Flow measurements regarding the timing of vortices during flutter, *Journal of Wind Engineering and Industrial Aerodynamics* **98**, 864-871.

- Taylor, Z. J.; Palombi, E.; Gurka, R. and Kopp, G. A. (2011), Features of the turbulent flow around symmetric elongated bluff bodies, *Journal of Fluids and Structures* **27**, 250-265.

The copyrights of these articles belong to the respective publishing companies of each journal (IEEE for the first and Elsevier for the latter two). Permissions for reuse in the current context of a thesis have been obtained for each of these articles and are included in this appendix.

ELSEVIER LICENSE
TERMS AND CONDITIONS

Sep 19, 2011

This is a License Agreement between Zachary J Taylor ("You") and Elsevier ("Elsevier") provided by Copyright Clearance Center ("CCC"). The license consists of your order details, the terms and conditions provided by Elsevier, and the payment terms and conditions.

All payments must be made in full to CCC. For payment instructions, please see information listed at the bottom of this form.

Supplier	Elsevier Limited The Boulevard,Langford Lane Kidlington,Oxford,OX5 1GB,UK
Registered Company Number	1982084
Customer name	Zachary J Taylor
Customer address	University of Western Ontario London, ON N6G 3T4
License number	2752771043246
License date	Sep 19, 2011
Licensed content publisher	Elsevier
Licensed content publication	Journal of Wind Engineering and Industrial Aerodynamics
Licensed content title	Flow measurements regarding the timing of vortices during flutter
Licensed content author	Zachary J. Taylor,Gregory A. Kopp,Roi Gurka
Licensed content date	December 2010
Licensed content volume number	98
Licensed content issue number	12
Number of pages	8
Start Page	864
End Page	871
Type of Use	reuse in a thesis/dissertation
Portion	full article
Format	both print and electronic
Are you the author of this Elsevier article?	Yes
Will you be translating?	No
Order reference number	
Title of your thesis/dissertation	Vortex shedding of elongated bluff bodies

Expected completion date	Sep 2011
Estimated size (number of pages)	170
Elsevier VAT number	GB 494 6272 12
Permissions price	0.00 USD
VAT/Local Sales Tax	0.0 USD / 0.0 GBP
Total	0.00 USD
Terms and Conditions	

INTRODUCTION

1. The publisher for this copyrighted material is Elsevier. By clicking "accept" in connection with completing this licensing transaction, you agree that the following terms and conditions apply to this transaction (along with the Billing and Payment terms and conditions established by Copyright Clearance Center, Inc. ("CCC"), at the time that you opened your Rightslink account and that are available at any time at http://myaccount.copyright.com).

GENERAL TERMS

2. Elsevier hereby grants you permission to reproduce the aforementioned material subject to the terms and conditions indicated.

3. Acknowledgement: If any part of the material to be used (for example, figures) has appeared in our publication with credit or acknowledgement to another source, permission must also be sought from that source. If such permission is not obtained then that material may not be included in your publication/copies. Suitable acknowledgement to the source must be made, either as a footnote or in a reference list at the end of your publication, as follows:

"Reprinted from Publication title, Vol /edition number, Author(s), Title of article / title of chapter, Pages No., Copyright (Year), with permission from Elsevier [OR APPLICABLE SOCIETY COPYRIGHT OWNER]." Also Lancet special credit - "Reprinted from The Lancet, Vol. number, Author(s), Title of article, Pages No., Copyright (Year), with permission from Elsevier."

4. Reproduction of this material is confined to the purpose and/or media for which permission is hereby given.

5. Altering/Modifying Material: Not Permitted. However figures and illustrations may be altered/adapted minimally to serve your work. Any other abbreviations, additions, deletions and/or any other alterations shall be made only with prior written authorization of Elsevier Ltd. (Please contact Elsevier at permissions@elsevier.com)

6. If the permission fee for the requested use of our material is waived in this instance, please be advised that your future requests for Elsevier materials may attract a fee.

7. Reservation of Rights: Publisher reserves all rights not specifically granted in the combination of (i) the license details provided by you and accepted in the course of this licensing transaction, (ii) these terms and conditions and (iii) CCC's Billing and Payment terms and conditions.

8. License Contingent Upon Payment: While you may exercise the rights licensed immediately upon issuance of the license at the end of the licensing process for the transaction, provided that you have disclosed complete and accurate details of your proposed use, no license is finally effective unless and until full payment is received from you (either by publisher or by CCC) as provided in CCC's Billing and Payment terms and conditions. If full payment is not received on a timely basis, then any license preliminarily granted shall be deemed automatically revoked and shall be void as if never granted. Further, in the event that you breach any of these terms and conditions or any of CCC's Billing and Payment terms and conditions, the license is automatically revoked and shall be void as if never granted. Use of materials as described in a revoked license, as well as any use of the materials beyond the scope of an unrevoked license, may constitute copyright infringement and publisher reserves the right to take any and all action to protect its copyright in the materials.

9. Warranties: Publisher makes no representations or warranties with respect to the licensed material.

10. Indemnity: You hereby indemnify and agree to hold harmless publisher and CCC, and their respective officers, directors, employees and agents, from and against any and all claims arising out of your use of the licensed material other than as specifically authorized pursuant to this license.

11. No Transfer of License: This license is personal to you and may not be sublicensed, assigned, or transferred by you to any other person without publisher's written permission.

12. No Amendment Except in Writing: This license may not be amended except in a writing signed by both parties (or, in the case of publisher, by CCC on publisher's behalf).

13. Objection to Contrary Terms: Publisher hereby objects to any terms contained in any purchase order, acknowledgment, check endorsement or other writing prepared by you, which terms are inconsistent with these terms and conditions or CCC's Billing and Payment terms and conditions. These terms and conditions, together with CCC's Billing and Payment terms and conditions (which are incorporated herein), comprise the entire agreement between you and publisher (and CCC) concerning this licensing transaction. In the event of any conflict between your obligations established by these terms and conditions and those established by CCC's Billing and Payment terms and conditions, these terms and conditions shall control.

14. Revocation: Elsevier or Copyright Clearance Center may deny the permissions described in this License at their sole discretion, for any reason or no reason, with a full refund payable to you. Notice of such denial will be made using the contact information provided by you. Failure to receive such notice will not alter or invalidate the denial. In no event will Elsevier or Copyright Clearance Center be responsible or liable for any costs, expenses or damage incurred by you as a result of a denial of your permission request, other than a refund of the amount(s) paid by you to Elsevier and/or Copyright Clearance Center for denied permissions.

LIMITED LICENSE

The following terms and conditions apply only to specific license types:

15. **Translation**: This permission is granted for non-exclusive world **English** rights only unless

your license was granted for translation rights. If you licensed translation rights you may only translate this content into the languages you requested. A professional translator must perform all translations and reproduce the content word for word preserving the integrity of the article. If this license is to re-use 1 or 2 figures then permission is granted for non-exclusive world rights in all languages.

16. **Website**: The following terms and conditions apply to electronic reserve and author websites:
Electronic reserve: If licensed material is to be posted to website, the web site is to be password-protected and made available only to bona fide students registered on a relevant course if:
This license was made in connection with a course,
This permission is granted for 1 year only. You may obtain a license for future website posting,
All content posted to the web site must maintain the copyright information line on the bottom of each image,
A hyper-text must be included to the Homepage of the journal from which you are licensing at http://www.sciencedirect.com/science/journal/xxxxx or the Elsevier homepage for books at http://www.elsevier.com , and
Central Storage: This license does not include permission for a scanned version of the material to be stored in a central repository such as that provided by Heron/XanEdu.

17. **Author website** for journals with the following additional clauses:

All content posted to the web site must maintain the copyright information line on the bottom of each image, and
he permission granted is limited to the personal version of your paper. You are not allowed to download and post the published electronic version of your article (whether PDF or HTML, proof or final version), nor may you scan the printed edition to create an electronic version,
A hyper-text must be included to the Homepage of the journal from which you are licensing at http://www.sciencedirect.com/science/journal/xxxxx , As part of our normal production process, you will receive an e-mail notice when your article appears on Elsevier's online service ScienceDirect (www.sciencedirect.com). That e-mail will include the article's Digital Object Identifier (DOI). This number provides the electronic link to the published article and should be included in the posting of your personal version. We ask that you wait until you receive this e-mail and have the DOI to do any posting.
Central Storage: This license does not include permission for a scanned version of the material to be stored in a central repository such as that provided by Heron/XanEdu.

18. **Author website** for books with the following additional clauses:
Authors are permitted to place a brief summary of their work online only.
A hyper-text must be included to the Elsevier homepage at http://www.elsevier.com

All content posted to the web site must maintain the copyright information line on the bottom of each image
You are not allowed to download and post the published electronic version of your chapter, nor may you scan the printed edition to create an electronic version.
Central Storage: This license does not include permission for a scanned version of the material to

be stored in a central repository such as that provided by Heron/XanEdu.

19. **Website** (regular and for author): A hyper-text must be included to the Homepage of the journal from which you are licensing at http://www.sciencedirect.com/science/journal/xxxxx. or for books to the Elsevier homepage at http://www.elsevier.com

20. **Thesis/Dissertation**: If your license is for use in a thesis/dissertation your thesis may be submitted to your institution in either print or electronic form. Should your thesis be published commercially, please reapply for permission. These requirements include permission for the Library and Archives of Canada to supply single copies, on demand, of the complete thesis and include permission for UMI to supply single copies, on demand, of the complete thesis. Should your thesis be published commercially, please reapply for permission.

21. **Other Conditions**:

v1.6

If you would like to pay for this license now, please remit this license along with your payment made payable to "COPYRIGHT CLEARANCE CENTER" otherwise you will be invoiced within 48 hours of the license date. Payment should be in the form of a check or money order referencing your account number and this invoice number RLNK<%=invoiceNo%>.
Once you receive your invoice for this order, you may pay your invoice by credit card. Please follow instructions provided at that time.

Make Payment To:
Copyright Clearance Center
Dept 001
P.O. Box 843006
Boston, MA 02284-3006

For suggestions or comments regarding this order, contact RightsLink Customer Support: customercare@copyright.com or +1-877-622-5543 (toll free in the US) or +1-978-646-2777.

Gratis licenses (referencing $0 in the Total field) are free. Please retain this printable license for your reference. No payment is required.

ELSEVIER LICENSE
TERMS AND CONDITIONS

Sep 19, 2011

This is a License Agreement between Zachary J Taylor ("You") and Elsevier ("Elsevier") provided by Copyright Clearance Center ("CCC"). The license consists of your order details, the terms and conditions provided by Elsevier, and the payment terms and conditions.

All payments must be made in full to CCC. For payment instructions, please see information listed at the bottom of this form.

Supplier	Elsevier Limited The Boulevard,Langford Lane Kidlington,Oxford,OX5 1GB,UK
Registered Company Number	1982084
Customer name	Zachary J Taylor
Customer address	University of Western Ontario London, ON N6G 3T4
License number	2752780261887
License date	Sep 19, 2011
Licensed content publisher	Elsevier
Licensed content publication	Journal of Fluids and Structures
Licensed content title	Features of the turbulent flow around symmetric elongated bluff bodies
Licensed content author	Z.J. Taylor,E. Palombi,R. Gurka,G.A. Kopp
Licensed content date	February 2011
Licensed content volume number	27
Licensed content issue number	2
Number of pages	16
Start Page	250
End Page	265
Type of Use	reuse in a thesis/dissertation
Intended publisher of new work	other
Portion	full article
Format	both print and electronic
Are you the author of this Elsevier article?	Yes
Will you be translating?	No
Order reference number	

Order reference number	
Title of your thesis/dissertation	Vortex shedding of elongated bluff bodies
Expected completion date	Sep 2011
Estimated size (number of pages)	170
Elsevier VAT number	GB 494 6272 12
Permissions price	0.00 USD
VAT/Local Sales Tax	0.0 USD / 0.0 GBP
Total	0.00 USD
Terms and Conditions	

INTRODUCTION

1. The publisher for this copyrighted material is Elsevier. By clicking "accept" in connection with completing this licensing transaction, you agree that the following terms and conditions apply to this transaction (along with the Billing and Payment terms and conditions established by Copyright Clearance Center, Inc. ("CCC"), at the time that you opened your Rightslink account and that are available at any time at http://myaccount.copyright.com).

GENERAL TERMS

2. Elsevier hereby grants you permission to reproduce the aforementioned material subject to the terms and conditions indicated.

3. Acknowledgement: If any part of the material to be used (for example, figures) has appeared in our publication with credit or acknowledgement to another source, permission must also be sought from that source. If such permission is not obtained then that material may not be included in your publication/copies. Suitable acknowledgement to the source must be made, either as a footnote or in a reference list at the end of your publication, as follows:

"Reprinted from Publication title, Vol /edition number, Author(s), Title of article / title of chapter, Pages No., Copyright (Year), with permission from Elsevier [OR APPLICABLE SOCIETY COPYRIGHT OWNER]." Also Lancet special credit - "Reprinted from The Lancet, Vol. number, Author(s), Title of article, Pages No., Copyright (Year), with permission from Elsevier."

4. Reproduction of this material is confined to the purpose and/or media for which permission is hereby given.

5. Altering/Modifying Material: Not Permitted. However figures and illustrations may be altered/adapted minimally to serve your work. Any other abbreviations, additions, deletions and/or any other alterations shall be made only with prior written authorization of Elsevier Ltd. (Please contact Elsevier at permissions@elsevier.com)

6. If the permission fee for the requested use of our material is waived in this instance, please be advised that your future requests for Elsevier materials may attract a fee.

7. Reservation of Rights: Publisher reserves all rights not specifically granted in the combination of

(i) the license details provided by you and accepted in the course of this licensing transaction, (ii) these terms and conditions and (iii) CCC's Billing and Payment terms and conditions.

8. License Contingent Upon Payment: While you may exercise the rights licensed immediately upon issuance of the license at the end of the licensing process for the transaction, provided that you have disclosed complete and accurate details of your proposed use, no license is finally effective unless and until full payment is received from you (either by publisher or by CCC) as provided in CCC's Billing and Payment terms and conditions. If full payment is not received on a timely basis, then any license preliminarily granted shall be deemed automatically revoked and shall be void as if never granted. Further, in the event that you breach any of these terms and conditions or any of CCC's Billing and Payment terms and conditions, the license is automatically revoked and shall be void as if never granted. Use of materials as described in a revoked license, as well as any use of the materials beyond the scope of an unrevoked license, may constitute copyright infringement and publisher reserves the right to take any and all action to protect its copyright in the materials.

9. Warranties: Publisher makes no representations or warranties with respect to the licensed material.

10. Indemnity: You hereby indemnify and agree to hold harmless publisher and CCC, and their respective officers, directors, employees and agents, from and against any and all claims arising out of your use of the licensed material other than as specifically authorized pursuant to this license.

11. No Transfer of License: This license is personal to you and may not be sublicensed, assigned, or transferred by you to any other person without publisher's written permission.

12. No Amendment Except in Writing: This license may not be amended except in a writing signed by both parties (or, in the case of publisher, by CCC on publisher's behalf).

13. Objection to Contrary Terms: Publisher hereby objects to any terms contained in any purchase order, acknowledgment, check endorsement or other writing prepared by you, which terms are inconsistent with these terms and conditions or CCC's Billing and Payment terms and conditions. These terms and conditions, together with CCC's Billing and Payment terms and conditions (which are incorporated herein), comprise the entire agreement between you and publisher (and CCC) concerning this licensing transaction. In the event of any conflict between your obligations established by these terms and conditions and those established by CCC's Billing and Payment terms and conditions, these terms and conditions shall control.

14. Revocation: Elsevier or Copyright Clearance Center may deny the permissions described in this License at their sole discretion, for any reason or no reason, with a full refund payable to you. Notice of such denial will be made using the contact information provided by you. Failure to receive such notice will not alter or invalidate the denial. In no event will Elsevier or Copyright Clearance Center be responsible or liable for any costs, expenses or damage incurred by you as a result of a denial of your permission request, other than a refund of the amount(s) paid by you to Elsevier and/or Copyright Clearance Center for denied permissions.

LIMITED LICENSE

The following terms and conditions apply only to specific license types:

15. **Translation**: This permission is granted for non-exclusive world **English** rights only unless your license was granted for translation rights. If you licensed translation rights you may only translate this content into the languages you requested. A professional translator must perform all translations and reproduce the content word for word preserving the integrity of the article. If this license is to re-use 1 or 2 figures then permission is granted for non-exclusive world rights in all languages.

16. **Website**: The following terms and conditions apply to electronic reserve and author websites:
Electronic reserve: If licensed material is to be posted to website, the web site is to be password-protected and made available only to bona fide students registered on a relevant course if:
This license was made in connection with a course,
This permission is granted for 1 year only. You may obtain a license for future website posting,
All content posted to the web site must maintain the copyright information line on the bottom of each image,
A hyper-text must be included to the Homepage of the journal from which you are licensing at http://www.sciencedirect.com/science/journal/xxxxx or the Elsevier homepage for books at http://www.elsevier.com , and
Central Storage: This license does not include permission for a scanned version of the material to be stored in a central repository such as that provided by Heron/XanEdu.

17. **Author website** for journals with the following additional clauses:

All content posted to the web site must maintain the copyright information line on the bottom of each image, and
he permission granted is limited to the personal version of your paper. You are not allowed to download and post the published electronic version of your article (whether PDF or HTML, proof or final version), nor may you scan the printed edition to create an electronic version,
A hyper-text must be included to the Homepage of the journal from which you are licensing at http://www.sciencedirect.com/science/journal/xxxxx , As part of our normal production process, you will receive an e-mail notice when your article appears on Elsevier's online service ScienceDirect (www.sciencedirect.com). That e-mail will include the article's Digital Object Identifier (DOI). This number provides the electronic link to the published article and should be included in the posting of your personal version. We ask that you wait until you receive this e-mail and have the DOI to do any posting.
Central Storage: This license does not include permission for a scanned version of the material to be stored in a central repository such as that provided by Heron/XanEdu.

18. **Author website** for books with the following additional clauses:
Authors are permitted to place a brief summary of their work online only.
A hyper-text must be included to the Elsevier homepage at http://www.elsevier.com

All content posted to the web site must maintain the copyright information line on the bottom of each image
You are not allowed to download and post the published electronic version of your chapter, nor

may you scan the printed edition to create an electronic version.
Central Storage: This license does not include permission for a scanned version of the material to be stored in a central repository such as that provided by Heron/XanEdu.

19. **Website** (regular and for author): A hyper-text must be included to the Homepage of the journal from which you are licensing at http://www.sciencedirect.com/science/journal/xxxxx. or for books to the Elsevier homepage at http://www.elsevier.com

20. **Thesis/Dissertation**: If your license is for use in a thesis/dissertation your thesis may be submitted to your institution in either print or electronic form. Should your thesis be published commercially, please reapply for permission. These requirements include permission for the Library and Archives of Canada to supply single copies, on demand, of the complete thesis and include permission for UMI to supply single copies, on demand, of the complete thesis. Should your thesis be published commercially, please reapply for permission.

21. **Other Conditions**:

v1.6

If you would like to pay for this license now, please remit this license along with your payment made payable to "COPYRIGHT CLEARANCE CENTER" otherwise you will be invoiced within 48 hours of the license date. Payment should be in the form of a check or money order referencing your account number and this invoice number RLNK<%=invoiceNo%>.
Once you receive your invoice for this order, you may pay your invoice by credit card. Please follow instructions provided at that time.

Make Payment To:
Copyright Clearance Center
Dept 001
P.O. Box 843006
Boston, MA 02284-3006

For suggestions or comments regarding this order, contact RightsLink Customer Support: customercare@copyright.com or +1-877-622-5543 (toll free in the US) or +1-978-646-2777.

Gratis licenses (referencing $0 in the Total field) are free. Please retain this printable license for your reference. No payment is required.

Appendix B

Guidelines for use of time-resolved PIV system at UWO

There are many guides out there on how to do PIV. One of the most thorough is the book by Raffel et al. (1998) (see References). Also, for the interested reader, Prof. Jerry Westerweel's thesis is available in pdf format and is a good source written by one of the pioneers of digital particle image velocimetry. The full reference is:

- Westerweel, J. (1993), Digital Particle Image Velocimetry – Theory and Application. Ph.D. thesis, University Press (Delft). URL: http://www.ahd.tudelft.nl/~jerry/publ/thesis.pdf

In this section some guidelines are given that are applicable to performing PIV at UWO; however, the majority of the guidelines refer to the equipment itself.

B.1 Equipment

The PIV equipment at UWO is made up of two major components: the Darwin Duo Laser and the image streaming cameras/computers developed by IO Industries. The key characteristics of each are given as follows (more information is available in the documentation of each):

- Darwin Duo Laser
  - Diodes: Nd:YLF
  - Power: 80 W @ 3 kHz
  - Energy: 45 mJ/pulse total (2 diodes)
  - Wavelength: 527 nm
- Imaging
  - Full resolution: 1 megapixel
  - Bit depth: 10 bit
  - Streaming rate: 1000 Hz @ full resolution per camera
  - Streaming length: 23 min per camera (approx.)
- Seeding
  - Olive oil has shown best results, refer to Echols and Young (1963)

B.2 Experimental setup

Before the operation of either camera or laser, the experiment needs to be conceived and setup. Among all of the other parameters to consider, the important PIV ones are the position of the light sheet and the camera. Many different parameters go into these decisions; however, based on experience with this system it is recommended that users do not try and measure image windows of greater than approximately 20 cm. Past this size, the particle image diameters become too small and correlation becomes poorer. Also, regardless of the experiment, the level of seeding is important. The laser is certainly quite powerful; however, the individual pulse energy is still relatively low for PIV in air so high levels of seeding are desirable.

Once the plane of measurement is chosen, a cylindrical lens is used to expand the beam of the laser followed by a spherical lens to help focus the light sheet in the field-of-view (FOV). The beam should be expanded to only slightly bigger than the FOV with the cylindrical lens to minimize the loss of available light energy. A cylindrical lens with a smaller negative focal length leads to a wider beam expansion. The spherical lens should be chosen to be approximately the distance from the beam optics to the FOV. The reader is encouraged to try different spherical lenses to see the effect on the quality of the cross-correlation. As much as possible, the optics should be aligned close to the optimal location without turning on the laser. However, to fine tune the placement of the laser optics the laser will have to be run at low power. If, at high power, the light sheet optics need adjustment, this should be done by trial and error by LOWERING the power, making the adjustment, then raising the power to see if the desired change has occurred and so on. Making adjustments at high power is unnecessary and dangerous. Refer to §B.4 for instructions on changing the power of the laser.

With the light sheet in place, the cameras should be placed such that the desired field-of-view is captured. This can be determined using a calibration plate aligned with the light sheet. If it is necessary to put the cameras in the wind tunnel, they should be placed in such a way that they are least obtrusive.

B.3 Cameras and synchronization

In this section it is assumed that the lens aspects of the cameras (aperture, focal length, etc.) are known or can be found in other sources. The streaming system, which collects data from the cameras, is the most complex portion of the PIV system at UWO. This system was not purpose built for PIV and thus offers many settings for the wide possibility of applications for such a system. The successful use of this system for PIV measurements rely on certain settings. Ideally these settings do not get changed or reset; however, it is inevitable that this will not be the case. First, we start by opening the Streams software and the FASTCAM settings box as well as understanding how settings are applied.

- To begin, open Streams and select the previously used *.vl library
- Open the FASTCAM settings box by:
    - Right click one of the cameras on the left side of the screen in Streams
    - Configure device → Camera settings
- The upper right of the FASTCAM settings shows which camera is being manipulated.
- If the status bar on the lower left displays “Unknown” (or a variant), it means that the applied settings will not be registered with the camera and indicates that one of the frame grabber boards is not connected properly. There is no feedback to Streams from the Photron cameras so it does not guarantee that these settings are applied.

Data can be acquired with one camera or both cameras depending on the desired results. When operating with both cameras it is imperative to ensure that they are synchronized with each other or the clock drift of each camera will ruin the sensitive timing required for PIV. It is assumed that the reader can infer how to use the cameras in single camera mode from the following synchronized mode.

- Settings common to the two cameras in the FASTCAM settings box
    - Gain File: PixelGainData_Default_1024*.gdf (camera specific)
    - Calibrate shading: This should be done with an 18% Gray card
- Settings for Camera 18 (or Master camera)
    - *Settings in italics are irrelevant but included for completeness*

    - Mode box (upper left corner of FASTCAM settings box)
        - Frame rate: 1000
        - Sync Mode: Free Run
        - Output: 2x8x10 bit
    - Triggering box (lower right corner of FASTCAM settings box)
        - *Sync In: Disable*
        - Sync Out: Cam VSync Pos
        - *General Out: Exposure Pos*
        - *Trig Out: t_ttl_in*
- Settings for Camera 19 (or Slave camera)
    - Mode box
        - Frame rate: 1000
        - Sync Mode: External Sync Mode
        - Output: 2x8x10 bit
    - Triggering box
        - Sync In: Hirose Sync_In Pos
        - *Sync Out: Cam VSync Pos*
        - *General Out: Exposure Pos*
        - *Trig Out: t_ttl_in*
- Ensure that the hirose connectors (the ones with BNC connectors to the frame grabbers) are connected to the OUT for Camera 18 and the IN for Camera 19.
- Connect SYNC_OUT from Camera 18 to TRIG_IN on Camera 19
- It is often worth the time to ensure that the cameras are synchronized using an oscilloscope and the TRIG OUT serial connection on the back of the PC (this should have two BNC cables attached to pins 6 and 7).

The whole PIV system is synchronized to the timing of the cameras. However, the settings in Streams that allow for this synchronization seem to be reset each time the software is started. To set the correct values:

- Right click camera → Configure device → Click the Miscellaneous tab → Signal Manager button
- For each device (selected in the upper left corner):

- Ensure that the "Secondary FVAL" is enabled (checkbox in lower left corner)
- Set the FVAL Skip value to 1 (this performs the signal masking)

The synchronization between the cameras and the laser is accomplished through the use of TSI's Insight software and their synchronizer. There are 6 BNC ports on the back of the synchronizer labelled A through F. A and C are used for flashlamp lasers which are irrelevant for this PIV system. Ports E and F are ordinarily for cameras, but for this system are unnecessary. The following needs to be connected on the synchronizer:

- Port B and D are connected to the two BNC connections on the front of the laser power supply (does not matter which)
- RS-232 (Serial port) connection needs to be connected to the controlling PC
- External trigger is connected to the TRIG OUT serial connection on the back of the PC. This serial connection has two BNC cables connected to it. Depending on which camera is being used will depend on which cable to connect to. Pin 6 corresponds to Camera "18" and Pin 7 corresponds to Camera "19". The camera naming is based on the last two digits of their serial numbers.

The synchronization is performed using TSI's Insight 3G. The following needs to be performed to ensure that the system is synchronized:

- Open the "Timing Setup" box on the Capture tab
- The frequency should be set to somewhere between 500 – 1000 Hz. This value can be set by Tools → Component Setup → Laser Setup
- The camera trigger is high when on so it is a rising edge trigger; however, the synchronizer, by default, is triggered by a falling trigger. To change this behaviour go to Tools → Component Setup → Synchronizer setup and ensure that the toggle is set to "External Trigger Edge Rising" in the lower right
- Once again open the "Timing Setup" box on the Capture tab
- The mode should be on single
- The delta T should be set using the following,

$$\Delta t = \frac{pixel\ displacement}{U_\infty \times magnification}$$

where calibration is the physical size represented by one pixel. Pixel

displacements for interrogation windows of 32 x 32 pixels² are ideally 8; however, sometimes this is not possible. One should strive to get as close to 8 as possible to reduce the effect of peak locking errors.

- The external trigger box should be clicked
- The laser pulse delay should be in the range of 920-980 μs. This is the parameter which controls when the first laser pulse of a PIV cycle is fired. It is set to ensure that the first pulse appears in the first image of an image pair.

B.4 Laser

The laser is a Class IV laser which can cause permanent eye damage among other dangers thus the reader is urged to take all necessary precautions. These precautions include the proper use of laser safety goggles. Any alignment of laser optics should be done at the lowest possible power.

The following is a rough outline of how the laser operates and how to run the laser:

- The cooling system in the laser is one which requires water circulation in two loops. The laser head is the unit housing the diodes and from which the beam exits. The diodes in the head are cooled by a closed loop of steam distilled water between the head and the chiller. The chiller (at the base of the power supply) is then cooled by an open loop of running water between a source (typically a tap or a sink) and the drain.
- Prior to operation of the laser ensure that there are hoses connecting the chiller to a source (i.e., tap) and a drain. Also ensure that the reservoir of steam distilled water is full by unscrewing the blue cap on top of the spout on the front of the chiller. CHECK TO MAKE SURE THE SOURCE (TAP) IS ON BEFORE TURNING ON THE LASER TO AVOID OVERHEATING.
- The next step is to ensure that the laser is plugged into an adequate power source (AC 220V @ 60Hz, single phase)
- ENSURE THAT THE SHUTTER IS CLOSED (top right hand corner of the power supply)
- Once all of the preceding steps are ensured, the laser can be turned on with the

key, similar to starting a car and pressing the SELECT button

- The laser will then run through an initialization process of setting the temperature and current to the diodes
- Because the system is cooled by tap water whose temperature is relatively uncontrolled, it will take some time for the system to stabilize. The desired temperature is indicated on the screen (at the time of this writing it is 18°C)
- To change the power of the laser:
    - This can be done with the shutter closed or open. If open take necessary precaution including laser safety goggles.
    - Press the MENU button to the right of the screen on the power supply
    - Scroll down with the arrow buttons to SET CURRENT
    - For low power and all alignment purposes set the current to approximately 11 A
    - For high power during the experiments, set the current to 28 A
- To change from internal to external triggering:
    - Close the shutter
    - Press the MENU button to the right of the screen on the power supply
    - Scroll down with the arrow buttons to SET MODE
    - Make sure to LEAVE the laser set on PRF. DO NOT USE CW UNDER ANY CIRCUMSTANCE.
    - Select EXT
    - Ensure that the serial type connector is connected at the back of the power supply. It has a BNC connector coming off of it, but does not need to be connected. The serial connector has a jumper necessary for the operation of external triggering.
    - Ensure that the triggering mode switch is on DOUBLE
    - Connect the BNC cables from the synchronizer to the two on the front of the laser power supply
- To turn off the laser, close the shutter and turn the key counter-clockwise

B.5 Running an experiment

Experiments can be performed once the laser is setup and aligned, the cameras are in the correct position and the whole system is synchronized. The first step in running the experiment is to ensure that the cameras are focused. One can get a reasonable focus by focusing on the calibration plate that is aligned with the light sheet prior to running the experiment. However, it is almost always necessary to fine tune the focus. The following outlines a procedure to focus the cameras:

- Turn on the cameras using the LIVE capture mode (the button with an eye on it)
- Turn on the laser using internal triggering. Note: in this mode the laser will be firing both diodes at the same time which means that the images will be about twice as bright as one can expect during the real experiment.
- While checking the display screen, continually adjust the focus of the cameras (and possibly the aperture) until the particles are clearly in focus.

Once the system is focused, PIV captures can be taken. To capture PIV data:

- Reset the laser to external trigger mode
- In Insight 3G make sure that the 3 drop-down menus in the upper left are set to:
    - PIV
    - Synchronized
    - Continuous
- Click “Capture” in Insight 3G
- Now the system is waiting until the record button is pushed using the Streams software.
- Click “Record”
- The laser should fire and the cameras should capture data. Stop after desired time has transpired.
- If more space on the drives is needed, go to Movie → Movie Manager and delete data that is no longer required to free up space
- Export some of the data by clicking File → Export to... in Streams
- Give the file an appropriate name and export using the “Insight 3G tiff” filter (upper left)

- Cross-correlate the image pairs in Insight 3G to see the quality of the data
- It is advisable to perform these checks several times before sampling an entire dataset
- You're done!
- It is important to export and backup the recently acquired data. One can anticipate transfer times of roughly 1.5 hours/minute/camera of images.

Curriculum Vitae

Name:	Zachary Taylor
Post-secondary Education and Degrees:	The University of Western Ontario London, Ontario, Canada 2002-2006 B.E.Sc., Mechanical Engineering The University of Western Ontario London, Ontario, Canada 2006-2011 Ph.D., Civil and Environmental Engineering
Selected Honours and Awards:	Declined: Province of Ontario Graduate Scholarship 2009-2010 National Science and Engineering Research Council (NSERC) Doctoral Fellowship 2009-2011
Related Work Experience:	Teaching Assistant The University of Western Ontario 2006-2011

Selected Publications:

Articles published or accepted in refereed journals

Taylor, Z.J.; Palombi, E.; Gurka, R. & Kopp, G.A. (2011) Features of the turbulent flow around symmetric elongated bluff bodies, *J. Fluids Struct.*, **27**, 250-265.

Taylor, Z.J.; Kopp, G.A. & Gurka, R. (2010) Flow measurements regarding the timing of vortices during flutter, *J. Wind Eng. Ind. Aerodyn.*, **98**, 864-871.

Taylor, Z.J.; Gurka, R.; Kopp, G.A. & Liberzon, A. (2010) Long-duration time-resolved PIV to study unsteady aerodynamics, *IEEE Trans. Instrum. Meas.*, **58**, 3262-3269.

Selected refereed conferences

Taylor, Z.J.; Kopp, G.A. & Gurka, R. (2011) Effects of leading edge geometry on the flow around elongated bluff bodies, 7^{th} *Int. Symp. Turbul. Shear Flow Phenom.*, Ottawa, Canada, July 28-31.

Taylor, Z.J.; Kopp, G.A. & Gurka, R. (2009) Wake dynamics of a fluttering elongated bluff body, 6^{th} *Int. Symp. Turbul. Shear Flow Phenom.*, Seoul, Korea, June 22-24.

Taylor, Z.J.; Gurka, R. & Kopp, G.A. (2007) Wake measurements for a rectangular cylinder during torsional oscillation, 7^{th} *Int. Symp. Particle Image Velocimetry*, Rome, Italy, September 11-14.